Aalto-yliopisto
Aalto-universitetet
Aalto University

Master's Programme: European Mining, Minerals and Environmental Programme (EMMEP)

A Compositional Trace Element Study Between Ore-Gangue Mineral Pairs in Iron Oxide Apatite Ores of the Kiirunavaara and Per Geijer Ore Bodies

Desiree Beher

Master's Thesis
2021

Aalto-yliopisto
Aalto-universitetet
Aalto University

Author Desiree Beher

Title of thesis A Compositional Trace Element Study Between Ore-Gangue Mineral Pairs in Iron Oxide Apatite Ores of the Kiirunavaara and Per Geijer Ore Bodies

Programme European Mining, Minerals and Environmental Programme (EMMEP)

Major European Mining Course (EMC)

Thesis supervisor Jussi Leveinen (Aalto)

Thesis advisor(s) Univ. Prof. Dr. Lottermoser, Dr. rer nat. Stephanie Lohmeier

Collaborative partner LKAB

Date 15.03.2021 **Number of pages** 115 **Language** English

Abstract

IOA (iron oxide apatite) or Kiruna-type deposits are an important source of iron and potentially other elements (e.g., REE, P, Co). However, their genesis still remains an unanswered question with theories ranging from a magmatic to a hydrothermal origin.

Trace element distribution in magnetite allows to differentiate between magmatic and hydrothermal origin of Kiruna-type deposits. Since apatite plays an important role in IOA formation and its chemistry is used as a monitor of halogen behaviour in magmatic-hydrothermal systems, apatite mineralogy can set new constraints on the formation of IOA deposits. Therefore, trace elements in apatite and magnetite are investigated in this work in order to gain a better understanding of IOA formation.

A total of 34 samples are collected from five cores from the Swedish Kiirunavara deposit and from four cores from the neighbouring Per Geijer (Henry) IOA deposit. The samples are investigated regarding their mineralogy and their major, minor and trace element composition. Conventional microscopy is used for mineralogical characterisation, electron microprobe analysis (EMPA) for spot analysis of apatite and magnetite grains and inductively coupled plasma mass spectrometry (ICP-MS) for bulk chemical composition of pulp samples. Apatites are additionally studied with a SEM.

Trace elements in magnetite have combined magmatic and hydrothermal signatures with relatively high contents of Co (0.177 - 0.2440 wt\% CoO) and V (0.067 - 0.175 wt\% V$_2$O$_3$) pointing towards a magmatic origin. Low contents, mostly below detection limit, of Ti, Ni and Cr indicate a hydrothermal origin. Trace element discrimination diagrams reveal that high-T rather than low-T hydrothermal fluids account for the hydrothermal signature. Apatites from Kiirunavaara and Per Geijer are all fluorapatites suggesting a magmatic origin. Several apatites exceed F end member composition (>3.77 wt\% F). Fluorine tends to overfill the apatite halogen site, when enough CO_3^{2-} is present within the system. In addition, fluorine plays an important role by generating liquid immiscibility between silicic melt and Fe-P rich melt. This leads to the assumption that the IOA deposits from Kiirunavaara and Per Geijer are generated due to 1) injection of a magma into the crust, 2) assimilation of carbonates and evaporates that change the initial composition of the magma, 3) magma immiscibility and separation of a P-Fe volatile-rich melt from the fractionating silicate magma due to oxidizing conditions caused by the high F content and high water activity within the magma, 4) concentration of volatiles within the residual melts causes temperature and pressure to drop, which shifts the conditions towards a hydrothermal signature. The presence of a former evaporite bed is supported by the regional occurrence of scapolite. Monazite inclusions within the apatites that are believed to crystallize at high temperature around 800°C are another hint for a magmatic origin of the Kiirunavara and the Per Geijer ores.

Keywords Kiirunavaara; Per Geijer; Trace elements; volatile elements, magmatic, hydrothermal, ore genesis

Table of Contents

List of Figures

List of Tables

List of Abbreviations

BSE backscattered-electron 71

Cl apatites chlorapatites 67

FW footwall 11

F apatites fluorapatites 53

HW hanging wall 12

IOA iron oxide apatite 1

IOCG iron oxide copper-gold 5

KUJ Kiirunavaara 17

LA-ICP-MS laser ablation inductively coupled plasma 63

OH apatites hydroxyapatites 67

QP quarz porpyry 12

OZ ore zone 31

PG Per Geijer 15

QP quarz porpyry 12

REE rare earth elements 1

SEM scanning electron microscope XI

SP syenite porphyry 11

Abstract

IOA (iron oxide apatite) or Kiruna-type deposits are an important source of iron and potentially other elements (e.g., REE, P, Co). However, their genesis still remains an unanswered question with theories ranging from a magmatic to a hydrothermal origin.

Trace element distribution in magnetite allows to differentiate between magmatic and hydrothermal origin of Kiruna-type deposits. Since apatite plays an important role in IOA formation and its chemistry is used as a monitor of halogen behavior in magmatic-hydrothermal systems, apatite mineralogy can set new constraints on the formation of IOA deposits. Therefore, trace elements in apatite and magnetite are investigated in this work in order to gain a better understanding of IOA formation.

A total of 34 samples are collected from five cores from the Swedish Kiirunavara deposit and from four cores from the neighboring Per Geijer (Henry) IOA deposit. The samples are investigated regarding their mineralogy and their major, minor and trace element composition. Conventional microscopy is used for mineralogical characterisation, electron microprobe analysis (EMPA) for spot analysis of apatite and magnetite grains and inductively coupled plasma mass spectrometry (ICP-MS) for bulk chemical composition of pulp samples. Apatites are additionally studied with a scanning electron microscope (SEM).

Trace elements in magnetite have combined magmatic and hydrothermal signatures with relatively high contents of Co (0.177 - 0.2440 wt% CoO) and V (0.067 - 0.175 wt% V_2O_3) pointing towards a magmatic origin. Low contents, mostly below detection limit, of Ti, Ni and Cr indicate a hydrothermal origin. Trace element discrimination diagrams reveal that high-T rather than low-T hydrothermal fluids account for the hydrothermal signature. Apatites from Kiirunavaara and Per Geijer are all fluorapatites suggesting a magmatic origin. Several apatites exceed F end member composition (>3.77 wt% F). Fluorine tends to overfill the

apatite halogen site, when enough CO_3^{2-} is present within the system. In addition, fluorine plays an important role by generating liquid immiscibility between silicic melt and Fe-P rich melt. This leads to the assumption that the IOA deposits from Kiirunavaara and Per Geijer are generated due to 1) injection of a magma into the crust, 2) assimilation of carbonates and evaporates that change the initial composition of the magma, 3) magma immiscibility and separation of a P-Fe volatile-rich melt from the fractionating silicate magma due to oxidizing conditions caused by the high F content and high water activity within the magma, 4) concentration of volatiles within the residual melts causes temperature and pressure to drop, which shifts the conditions towards a hydrothermal signature. The presence of a former evaporite bed is supported by the regional occurrence of scapolite. Monazite inclusions within the apatites that are believed to crystallize at high temperature around 800°C are another hint for a magmatic origin of the Kiirunavara and the Per Geijer ores.

1 Introduction

The genesis of the iron oxide apatite (IOA) ores, including the well-known Kiirunavaara ores, is until today a controversial topic. IOA deposits occur globally and are commonly hosted in volcanic and plutonic rocks in convergent tectonic settings and rift-related environments (Barton, 2014; Groves et al., 2010; Simon et al., 2018; Williams et al., 2005). Although IOA deposits are an important source of iron, mainly present as magnetite (Fe_3O_4), phosphorus and possibly rare earth elements (REE), their formation remains a great matter of discussion. Two main theories of formation exist: the magmatic model, established by pioneer Per Geijer (Geijer, 1930, 1931) associated with the generation and co-mingling of an iron-oxide rich, immiscible melt in coexistence with a silicic melt (Frietsch, 1978; Nyström & Henriques 1994, Nyström et al., 2008) and a hydrothermal model with the large-scale circulation of high-salinity fluids of either magmatic or non-magmatic origin (Hitzman et al., 1992; Smith et al., 2009, 2013). A new study outlines a combination of magmatic and hydrothermal processes by crystallization of magnetite microlites from a silicate melt, subsequent nucleation of aqueous fluid bubbles on magnetite surfaces and finally the formation and ascent of buoyant fluid bubble-magnetite aggregates (Knipping et al., 2015).

The trace element variability of magnetite, in response to formation conditions, has been the focus of different studies over the last decades (e.g., Nadoll et al., 2014). However, the answer to the question of the genesis of IOA deposits has not been found yet. In recent studies, a different approach was applied by investigating the role of P, F and Cl in apatite from these deposits (La Cruz et al., 2020; Palma et al., 2019; Zhang

et al., 2017). Apatite with the chemical formula $Ca_5[(F, Cl, OH)|(PO_4)_3]$ is a common accessory mineral in igneous rock (Piccoli & Candela, 2002) but represents a major constituent in IOA's. Fluorine, Cl and OH can be substituted for one another within the apatite structure, their concentration and proportion subsequently act as a monitor of magmatic-hydrothermal processes (Webster & Piccoli, 2015). Moreover, apatite can accommodate a wide range of trace elements including As, Sr, S, Th U, Y and REE that are sensitive to geochemical changes. These elements can record the composition of magmatic processes at the time of crystallization or can provide insights in fluid composition in hydrothermal systems (Bea et al., 1994; Belousova, 2000; Belousova et al., 2001; Sha & Chappell, 1999).

This study aims to set new constraints on the formation of IOA deposits in the Norrbotten area, exemplified by the deposits Kiirunavaara and Per Geijer, by combining a trace element study of iron ore with a trace element- and volatile element study of apatites. Most recent halogen studies examine apatites from the Chilean iron ore belt (Cruz et al., 2020; Palma et al., 2019) but not many apatite studies have yet been carried out in IOA's from Norrbotten. The deposits of Kiirunavaara and Per Geijer represent different formations of IOA-type deposits in the Norrbotten craton. The Per Geijer mineralizations are higher in the regional stratigraphy and are therefore younger than the Kiirunavaara ores. Both deposits also differ in iron ore composition and apatite contents. The Kiirunavaara ores are predominantly composed of magnetite and show a lower apatite content, whereas the Per Geijer mineralizations have a larger hematite and apatite content (Martinsson, 2015; LKAB, 2019).

In the scope of this study, samples are taken from Kiirunavaara and Per Geijer drillcores. They are investigated petrographically and geochemically in order to characterise the general mineralogy and the trace element composition of both ore zones and host rock zones. Inductively coupled plasma mass spectrometry (ICP-MS) is used for major and trace element analysis on bulk rock, electron microprobe analysis (EMPA) is applied for spot analysis on magnetite and apatite. This project is performed in collaboration with the company Luossavaara-Kiirunavaara Aktiebolag (LKAB) and the

Institute of Mineral Resource Engineering (MRE) of the RWTH Aachen University, Germany.

2 Working Objectives

This study is carried out to evaluate the petrography and trace element geochemistry of drillcore samples from the Kiirunavaara and Per Geijer orebodies in order to put new constraints on their genesis. This is achieved by drillcore sampling (34 samples) at different depths in the orebodies. The composition of the samples is investigated by using a combination of conventional transmitted and reflected microscopy, ICP-MS and EMPA. ICP-MS is applied on bulk rock pulps to determine major and trace element composition, EMPA spot analysis targets minor and trace element contents of magnetite and apatite. Discrimination diagrams serve to distinguish between magmatic and hydrothermal magnetite and apatite.

An additional benefit of this study is to obtain information of the so far underexplored Per Geijer ore bodies. The world class Kiirunavaara deposit belongs to one of the best-known deposits, whereas only minor research was done on the Per Geijer ore bodies. These deposits comprise five mineralized sites, of which four have been mined in the 20th century. A few years ago, LKAB launched a reassessment campaign to evaluate the mining potential of the remaining Per Geijer deposits. In order to take a concise decision, a detailed characterisation of the trace element composition of ore and waste is necessary since minor and trace elements have a direct impact on the final product with regard to the steel making process (Kroplop et al., 2020).

3 The Controversy about the Origin of IOA Deposits

IOA or Kiruna-type deposits are often classified as the "Cu-poor end member" of iron oxide copper-gold (IOCG) deposits (Knipping et al., 2015). They occur globally in a wide span of geological settings and range in age from Late Archean (2.5 Ga) to Mesozoic (Williams et al., 2005). The Kiirunavaara deposit is of early Proterozoic age (1.9 Ga; Martinsson et al., 2016) and thus belongs to the older ones, whereas the deposits from the Chilean iron ore belt (e.g., Los Colorados, Carmen, Fresia) and El Laco have a Late Jurassic to Early Cretaceous (130–100 Ma) age (Palma et al., 2020). In the Norrbotten area, in Chile and in many other mining provinces worldwide (e.g., Missouri iron metallogenic province) IOA's are spatially associated with IOCG deposits and a genetic link between these two deposit types has been proposed by several authors (Hitzman et al., 1992; Velasco & Tornos, 2009; Naslund et al., 2002; Nold et al., 2014). It is widely accepted that IOCG's are formed by hydrothermal processes. The fluids are argued to have a magmatic, or a non-magmatic metal source (Williams et al., 2005, 2010; Porter, 2010).

The debate about the origin of IOA deposits is even more complex. Some hypotheses invoke a strictly orthomagmatic origin (e.g., Nyström Henríquez, 1994; Naslund et al., 2002; Nyström et al., 2008) associated with liquid immiscibility between an oxide melt rich in iron, phosphorus and volatiles and a co-mingling silicate-rich melt, with separation and crystallization of the Fe-, P-, fluid-rich oxide melt forming IOA ores.

Other authors suggest a hydrothermal origin with fluids of either non-magmatic origin leaching iron from the surrounding plutons and metasomatic replacement of host rock (Rhodes et al., 1999; Haynes, 2000; Sillitoe Burrows, 2002) or of magmatic-hydrothermal origin with a fluid directly sourcing iron from magmas (Pollard, 2006). A hydrothermal origin would allow a genetic link between IOCG and IOA deposits.

4 Geochemical Background

4.1 Trace Element Geochemistry

Trace and minor elements only constitute a (very) minor fraction in a system. However, they provide valuable geochemical and geological information related to their abundance (White, 2013). In general, ten (eleven in sulfidic ore) or less major elements represent about 99% of bulk rock. Consequently, minor and trace elements are volumetrically mostly unimportant, but of high importance for ore characterisation. Variations in the concentrations and proportions of many trace elements are much larger than variations in the concentrations of major elements. The trace element abundance therefore contains information not available from the concentrations of major elements. Thus, trace element studies are a powerful tool in geochemistry as they serve as a "chemical fingerprint" of a geological system (White, 2013) and indicate the origin of rock/ore directly.

4.1.1 Trace Elements in Magnetite

Magnetite with the chemical formula Fe_3O_4 belongs to the most abundant oxide minerals in the continental crust and accounts for most of the iron in IOA deposits (Nadoll, 2014). This mineral can incorporate a large abundance of trace elements in it's inverse spinel structure (figure 4.1) and is therefore used in petrogenetic and geochemical studies since the early 20th century (Ramdohr, 1926). The general stoichiometry of magnetite is AB_2O_4 (Fleet, 1981), where A can be occupied by divalent cations such as Mg^{2+}, Fe^{2+}, $Ni^{2+}+$, Mn^{2+}, Co^{2+}, or Zn^{2+} and B by trivalent cation such as Al^{3+}, Fe^{3+}, Cr^{3+}, V^{3+},

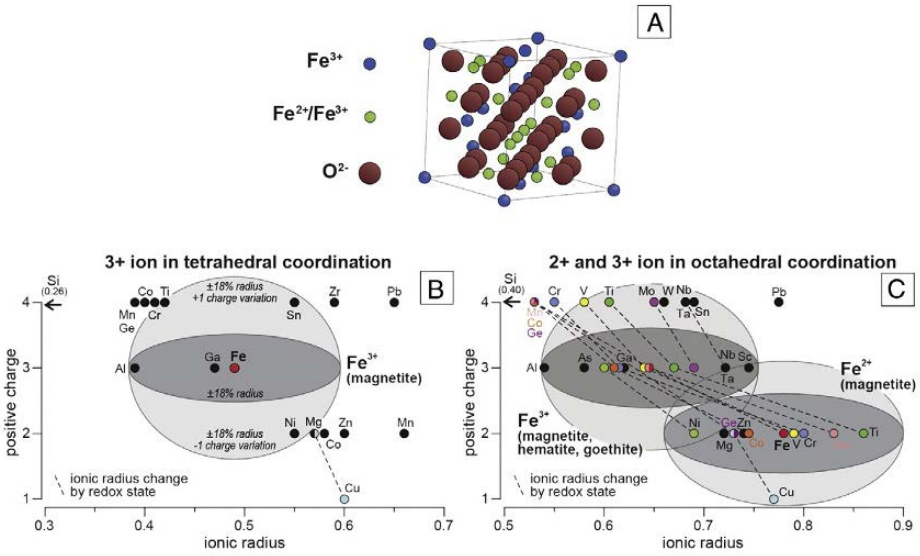

Figure 4.1 A: The cubic inverse spinel structure of magnetite. B, C: The ionic radius [Å] vs. the cation charge for the tetrahedral site (B) and the octahedral site (C) of magnetite. The incorporation of foreign cations is possible when the substituting cation has a similar charge and ionic radius (±15–18%; Goldschmidt, 1954). Figure is from Nadoll (2014).

Mn^{3+}, or Ga^{3+} (Lindsley, 1976a; Wechsler et al., 1984). The possibility to substitute Ti^{4+} on the B site is given when substitution is coupled with a divalent cation (Wechsler et al., 1984). Octahedral sites in the crystal lattice are randomly occupied by unequal numbers of Fe^{3+} and Fe^{2+}, whereas tetrahedral sites can exclusively be occupied by the smaller Fe^{3+} iron atoms (Lindsley, 1976a; Waychunas, 1991; Wechsler et al., 1984). This results in: $Fe^{3+} + [Fe^{2+} + Fe^{3+}]O_4$.

Due to the large amount of cations that magnetite can incorporate, specific formation conditions are reflected by the composition of magnetite (Dare, 2014a). Different discrimination diagrams based on element concentrations and ratios of the most common trace elements in magnetite (Al, Co, Cr, Ga, Mg, Mn, Ni, Sn, Ti, V, Zn) are proposed by several authors (Knipping et al. 2015; Dare et al. 2014a, 2014b; Nadoll et al. 2014). They are applied in order to help to discern the type of origin of the Kiirunavaara and Per Geijer deposits.

4.1.2 Trace Elements in Apatite

Apatite is a major constituent of IOA deposits and can be described by the general formula $A_5(XO_4)3Z$. The A-site is incorporated by large cations (e.g., Ca^{2+}, Sr^{2+}, Pb^{2+}, Ba^{2+}, Mg^{2+}, Mn^{2+}, Fe^{2+} ,REE^{3+}, Eu^{2+}, Cd^{2+}, Na^{+}) and comprises two sites that have VII-fold (Ca2) and IX-fold (Ca1) coordination. The X-site, accommodates predominately P^{5+} (as PO_4^3+) and has IV-fold coordination and can host other 4^{+}, 6^{+}, 5^{+} cations (e.g., Si , S , As , V). The Z site is occupied by the halogens F and Cl, as well as OH. Due to its ability of incorporating a wide range of trace elements into the mineral structure, apatite is considered a trace element recorder of magmatic processes at the time of crystallization as well as a recorder of fluid composition in hydrothermal processes (Bea et al., 1994; Toplis & Dingwell, 1996; Sha & Chappell, 1999; Belousova, 2000; Belousova et al., 2001). In addition, apatite helps to monitor volatiles in magmatic-hydrothermal processes because of the incorporation of F, Cl and OH in the Z-site of its structure (Pan & Fleet, 2002; Schettler et al., 2011). Hence, the halogen composition of apatite can provide important information of its origin as well as the origin of the associated ore (Palma et al., 2019).

5 Geological Background

The Fennoscandian shield (figure 5.1) and related deposits belong to the most important mining provinces in Europe. Economically most important are the apatite iron ores related to the Kiruna area in Norrbotten (figure 5.1) with more than two billion tons of ore mined since 1888 (Martinsson, 2015; Martinsson et al., 2016). These deposits belong to the IOA or Kiruna type deposits. Over 40 apatite iron sites are known to be located in the northern part of Sweden. They vary significantly in host rock lithology, degree of host rock alteration, P-content and Fe-content as well as associated minor components (Martinsson, 2004a). This study focuses on the geology of the Kiirunavaara and the Per Geijer deposits.

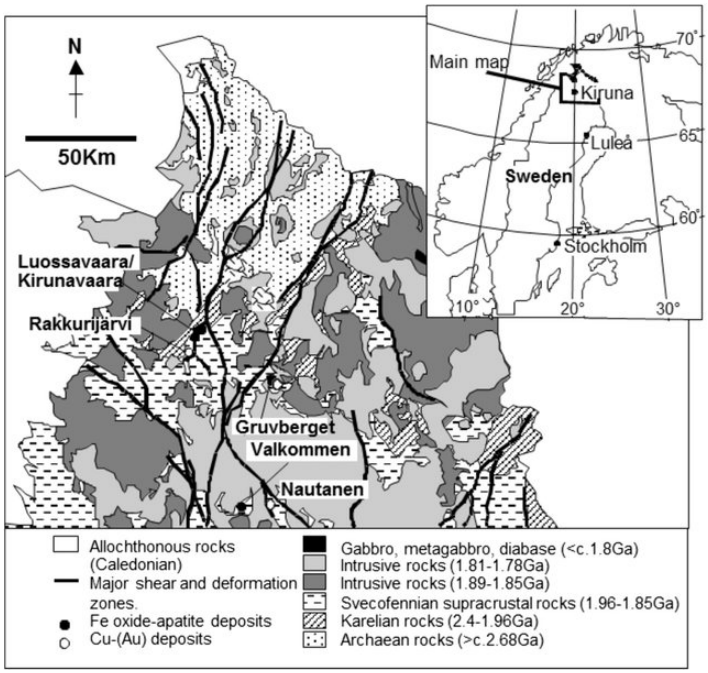

Figure 5.1 The Fennoscandian shield and the Norrbotten area (Storey & Smith, 2017).

5.1 Local Geology

5.1.1 Bedrocks

The basement of the Kiruna area is composed of Archaen rocks, which are heavily deformed and metamorphosed (Martinsson & Wanhainen, 2000). They are overlain by the Karelian (2.3-2.0 Ga) greenstones. The greenstones vary in composition ranging from ultramafic and intermediate-volcanic to volcano-sedimentary. The rocks become younger towards the east (Martinsson, 1997). The Kurravaara conglomerate was deposited on top of the Kiruna greenstones (table 5.1). The conglomerate is overlain by the Kiirunavaara group that hosts the IOA's.

The Kiirunavaara group can be divided into the Hopukka, Luossavaara and Matojärvi formation (Martinsson et al., 2013). These units are explained in the following and summarized in table 5.1. Note that this section is largely based on own observations from drillcore-logging. References are only given where necessary.

5.1.2 Hopukka Formation

The trachyandesitic Hopukka sequence is commonly called syenite porphyry (SP) (Geijer, 1910) and forms the footwall (FW) of the Kiirunavaara ores. These rocks represent a thick lava pile and are of intermediate volcanic composition. Subhedral to anhedral plagioclase phenocrysts and black nodular amygdules, mainly composed of actinolite, magnetite or biotite, are set into a grey to greenish-grey groundmass. The rocks show an overall moderate degree of potassic (K-feldspar + biotite), sodic (albite + actinolite ± titanite) and chloritic (chlorite) alteration. Magnetite veins or disseminations and schlieren of apatite also occur often. This sequence is not associated with the Per Geier ores.

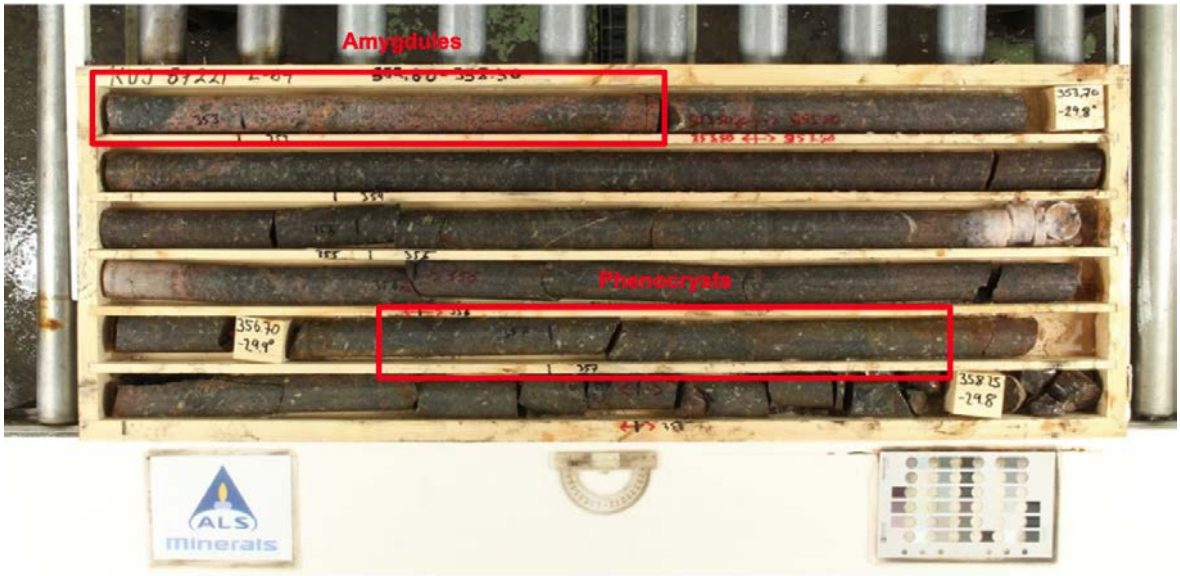

Figure 5.2 SP from drillhole KUJ-872112. Amygdules can be seen in the potassic altered zone at the top of drillcore. Anhedral phenocrysts are present at the bottom of drillcore.

5.1.3 Luossavaara Formation

The porphyritic rhyodacite of the Luossavaara formation, commonly called quarz porpyry (QP) forms the hanging wall (HW) of the Kiirunavaara ores and the FW of the Per Geijer mineralizations. The sequence is composed of grey, brown to red volcanics in the Kiruna deposit and grey to reddish pyroclastic tuffs and ignimbrites in Per Geijer. The rhyodacite has a fine-grained groundmass with mostly euhedral feldspar phenocrysts. The amount of phenocrysts is distinctly larger than in the trachyandesite. Magnetite veining or disseminations are very common. Rarely, apatite occurs as veining. These rocks of the Luossavaara formation are largely sodic altered, with minor potassic and weakly chloritic overprint. The Luossavaara formation in Kiirunavaara shows an overall moderate degree of alteration, whereas in Per Geijer these rocks are strongly to pervasive altered.

5.1.4 Matjärvi Formation

The Matjärvi formation has a metavolcanic and metasedimentary composition. The sequence begins with the Rektor porphyry, a strongly alkali altered volcanic rock or basalt. Above this volcanic unit follows a sedimentary sequence of volcani-clastic con-

Figure 5.3 QP from drillhole KUJ-872115. Rock is characterized by euhedral phenocrysts, which are typical of the QP. The rock is sodic altered.

Figure 5.4 Matjärvi fromation from drillcore PG-81156. The uppermost part of drillcore shows conglomerate, which is stratigraphically seen, followed by greywacke and conglomerate.

glomerates and greywackes. The upper part of the formation consists of mudstone and fine-grained greenschist. The entire Matjärvi formation is heavily altered. Hematite veins consist largely of specularite. In addition, specularite clasts are very common in conglomerate.

5.1.5 Iron Ore Mineralizations (Kiirunavaara & Per Geijer)

Magnetite mineralization in Kiruna is present in lower contact with the trachyandesite (SP) and in upper contact with the rhyodacite (QP). The ore zone consists of up to 150 m massive magnetite. Calcite veinlets such as patches of actinolite, chlorite, titanite and sulfide minerals are common throughout the ore zone. Apatite is likewise present

as veins, but can form dissemination or schlieren.

Figure 5.5 Massive ore from core KUJ-87115. The ore zone of this drillcore is about hundred meters long.

In the Per Geijer deposit, the mineralization is found in lower contact with the rhyodacite and in upper contact with the Matjärvi formation. The ore zone consists of several layers of hematite and magnetite. Hematite is more abundant towards the upper contact, whereas magnetite is more abundant towards the lower contact. Apatite veins and clasts occur frequently. The ore is not a massive horizon as in Kiirunavaara, rather brecciated with intercalated layers of host rock.

Figure 5.6 Brecciated ore from drillcore PG-81716. The ore zone comprises hematite and magnetite layers.

Table 5.1 Stratigraphic units in the Kiruna area.

Lithological unit		Rock types/ mineralizations	Comments
Kiirunavaara group	Matjärvi formation	Mudstone Greywacke Conglomerate Rektor porphyry/ Basalt	Conglomerate contains hematite in clasts & veins
	Per Geijer ore	Hematite Magnetite	Hematite >Magnetite
	Luossavaara formation	Rhyodacite	Magnetite veins/ patches & disseminations
	Kiruna ore	Magnetite	-
	Trachyandesite	Trachyandesite	Magnetite in veins & dissemination's

5.1.6 Hauki Quartzite

The youngest formation that overlies the rhyodacite in Kiruna and the Matojärvi formation in Per Geijer is the <1.88 Ga Hauki quartzite. The unit consists of arkose, quartzite and conglomerate layers. The detailed stratigraphy in the Kiruna area is presented in figure 5.7.

5.2 The Kiirunavaara Deposit

Kiirunavaara is the largest iron ore deposit in Europe with pre-mining resources of two billion tons with an iron (Fe) content between 60% and 68%. The ore body is massive, tabular and stratabound, five km long, up to 100 m thick, and it extends at least 1500 m below surface. The deposit stratigraphy is illustrated in figure 5.7. The phosphorus content of the ore zone averages 1%. Ore, low in apatite, is situated close to the FW, ore rich in apatite is mostly found near the HW (Martinsson & Wanhaien, 2000).

5.3 The Per Geijer Deposit

The Per Geijer (PG) deposit is located only a few kilometres northeast of Kiirunavaara and comprises five mineralized sites: Rektorn, Henry, Haukivaara, Nuktus and Lappmalmen (figure 5.7). The first four orebodies have been mined in the 20th century,

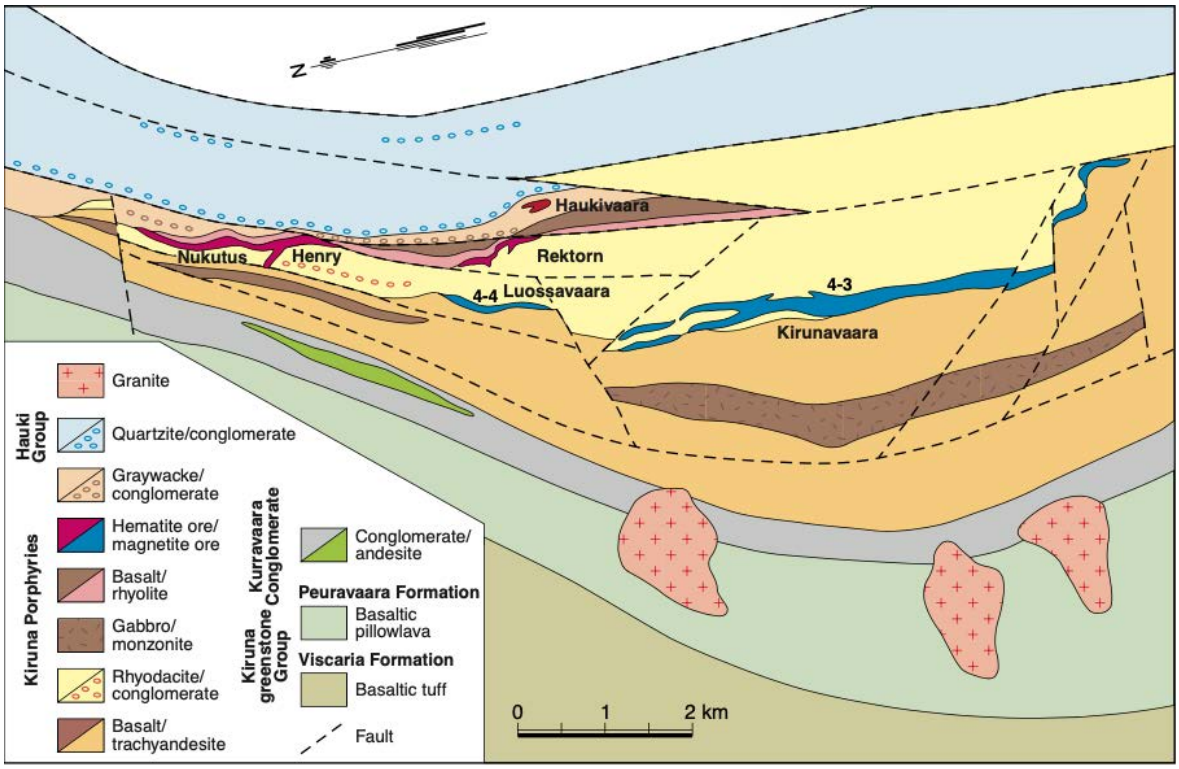

Figure 5.7 Regional geology of the Kiruna area (Martinsson et al., 2013).

the deeper Lappmalmen orebody is still untouched. A total of 10.98 Mt ore have been mined in Per Geijer (LKAB, 2019). The deposit is higher in the stratigraphy than Kiirunavaara (figure 5.7) and also differs in chemical composition. Iron ore mineralizations are linked to several horizons. The lowermost horizon is dominated by magnetite, the uppermost contains hematite only. Both iron oxides occur mainly intergrown with each other. The PG deposit is, with an average content of 3-5% P, richer in phosphorus than Kiirunavaara, but average iron content is with 40% Fe less. PG also shows REE anomalies reflected by monazite, allanite and xenotime, mainly associated in the apatite rich parts (Martinsson, 2015). LKAB is reevaluating the mining potential of PG for a few years. The exploration potential of the remaining ore was estimated to be 1465 Mt of 34% Fe (LKAB, 2019).

6 Sampling Process

6.1 Drillcore Selection

A total of five drillcores from Kiirunavaara (KUJ) and four from Henry, Per Geijer (PG) were chosen for detailed analysis. Their location is shown below (figure 6.1 - 6.4). These most promising drillcores were selected by LKAB and logged at the 1045 level in the Kiruna mine. The PG drillcores were all drilled from surface right in proximity of the former open pit. Drillcore 81163, 81156 and 81165 represent the shallow/ intermediate part, whereas drillcore 81617 reflects the deep part of Henry. Drillcores 81165 and 81163 have been drilled north, drillcore 81617 east and drillcore 81156 south-west within the deposit (figure 6.3). The KUJ drillcores were all drilled from the 1375 m level exploration drift and represent the deep part of the system.

6.2 Drillcore Logging

All nine drillcores have been logged in order to determine the lithology, mineralogy, cross cutting relationships and alteration zones. Results of drillcore logging are in the appendix.

6.3 Sample Selection

After the drillcore logging was completed, 34 samples were collected from different depths of the nine drillholes. The locations from where the samples were taken are

marked in figure 6.1 and figure 6.3, a sample overview can be found in table 6.2 and table 6.3. The clear area of interest for sampling was the host rock/ore contact zone at the HW and FW boundary. The following criteria were applied during sample selection:

- Sampling targeted the halogen concentration in the ore zone and the host rock zone. Consequently, apatite from both lithological areas should be sampled.
- Samples should contain an ore mineral and an immediately adjacent gangue mineral.
- The samples should be taken close to the lithological boundary between the ore and the host rock. This maximizes the possibility to take samples reflecting the greatest rate of change in geochemistry.
- Ore and gangue minerals should represent similar final conditions with regards to temperature and pressure. The sampled area should therefore be as free as possible of any type of veining or alteration in order to avoid any post-mineralization modification of ore and gangue minerals in the samples.

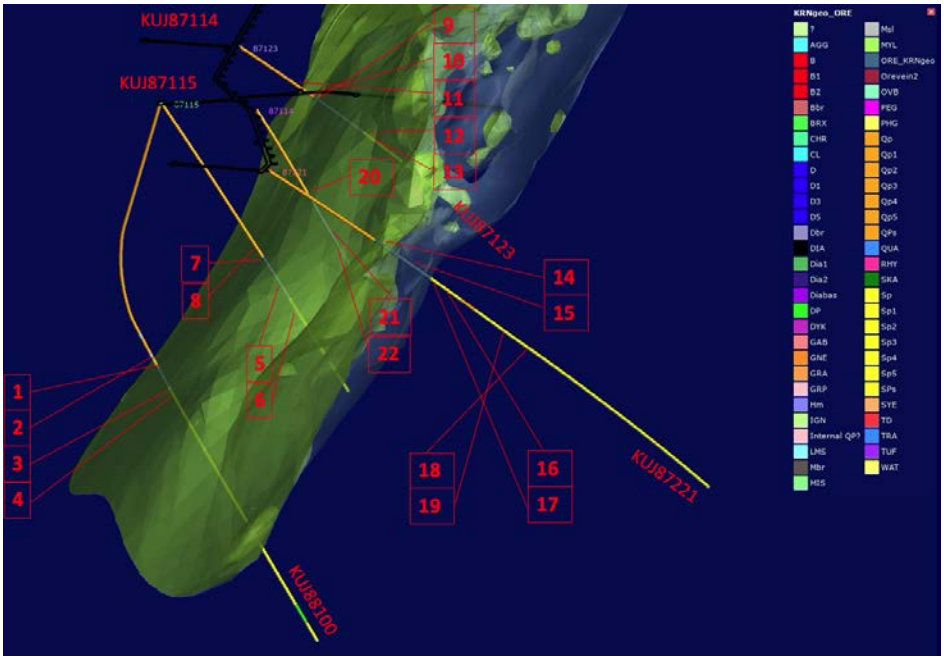

Figure 6.1 Location of all five Kiruna drillholes in vertical view. Image was taken with Leapfrog software.

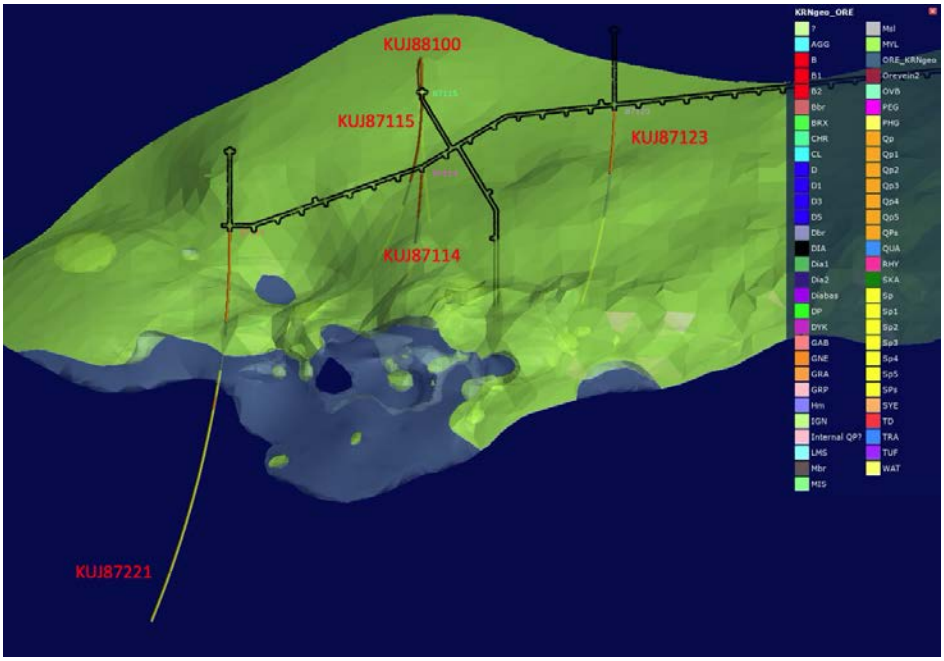

Figure 6.2 Location of all five Kiruna drillholes in horizontal view. Image was taken with Leapfrog software.

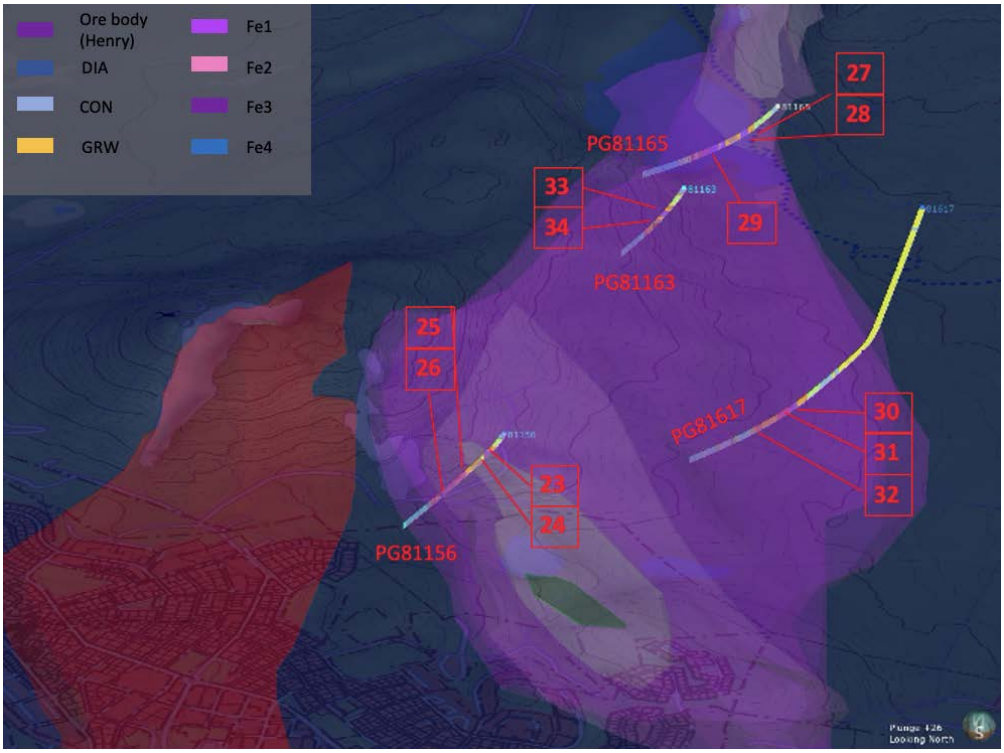

Figure 6.3 Vertcial drill hole orientation of all four Per Geijer drillholes. Image was taken with Leapfrog software.

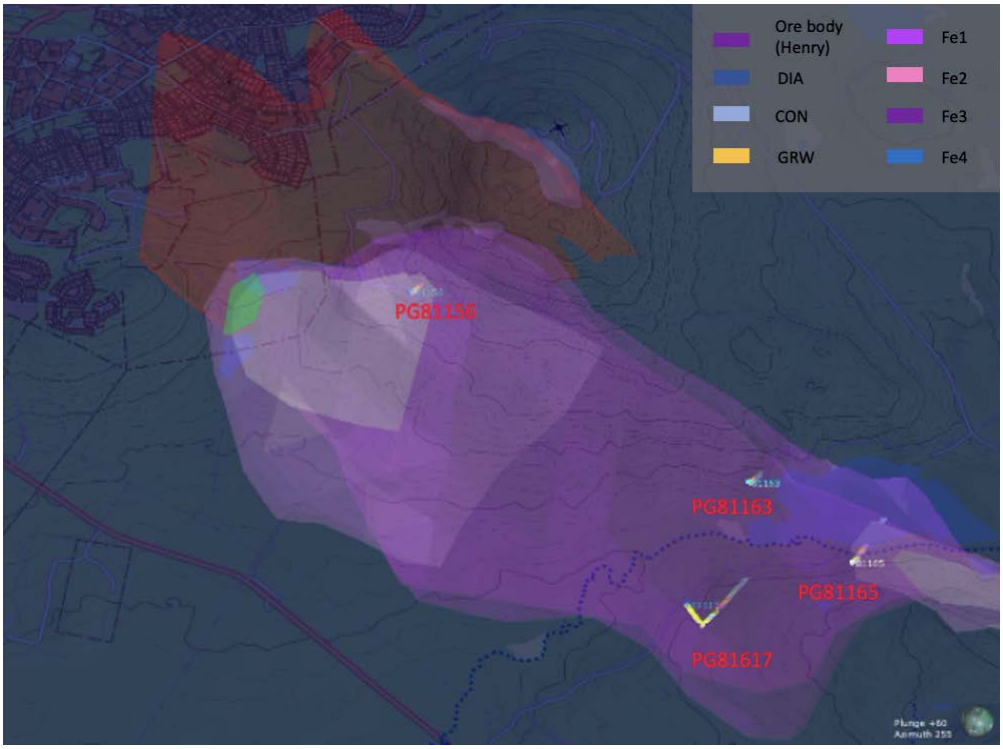

Figure 6.4 Horizontal drill hole orientation of all four Per Geijer drillholes. Image was taken with Leapfrog software.

6.3.1 Sample Overview

In total 22 samples were taken from the Kiirunavaara orebody, from which 11 originate from the host rock and 11 from the ore zone. Different ore types including massive ore from the ore zone and disseminated, layered and patched ore from the host rock zone have been sampled. A total of 12 samples were taken in Per Geijer, 11 from the ore zone, one from the host rock. In KUJ samples were taken from HW, ore zone and FW. However, no suitable area for sampling in the HW was found in Per Geijer due to the higher degree of alteration in this deposit. Therefore, 11 from the 12 PG samples originate from the ore zone, one from the FW. Ore types include massive, disseminated, layered and patched ore. The 34 samples are listed in table 6.2 and table 6.3 with a short description. A detailed description including pictures can be found in the appendix. The abbreviations used for the different minerals are shown in table 6.1. The coding scheme of the samples is arranged as presented below.

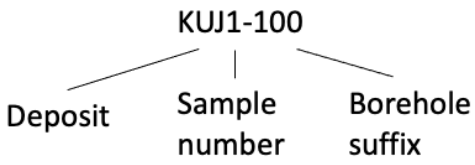

Note that the depth given in the tables represents depth below surface for the PG samples, but not for the KUJ samples that have been drilled from the 1375 m level.

Table 6.1 Abbreviations used for minerals.

Mineral	Abbreviation	Mineral	Abbreviation	Mineral	Abbreviation
Magnetite	Mt	Apatite	Ap	Actionolite	Act
Hematite	Hem	Potassium feldspar	KF	Biotite	Bio
Chlorite	Chl	Titanite	Tit	Quarz	Qz
Calcite	Cal	Limonite	Lim	Albite	Alb

Table 6.2 Brief sample description of mapped sample KUJ1-100 to KUJ13-123 with sampled intervals.

Sample Nr	Core	Depth	Description
KUJ1-100	KUJ-88100	479.78 m	sample taken at HW/ore boundary
			contains layered Ap + KF + Act + Mt rich in Ap
KUJ2-100	KUJ-88100	475.70 m	taken in HW
			Mt patch + Act + Tit + Ap
KUJ3-100	KUJ-88100	517.70 m	taken at the FW/ ore boundary
			Mt patch + Act + Ap + Tit
KUJ4-100	KUJ-88100	530.50 m	taken in FW
			disseminated Mt + Act
KUJ5-115	KUJ-87115	390.80 m	taken in ore zone
			massive Mt + Act rich in Mt, very little gangue
KUJ6-115	KUJ-87115	404.52 m	taken in FW
			Mt patch + Act + little Chl
KUJ7-115	KUJ-87115	308.45 m	take in ore zone close to HW contact
			massive Mt + Act + Ap rich in Mt, little gangue
KUJ8-115	KUJ-87115	304.12 m	taken in HW
			Mt patch + Act + KF + Ap
KUJ9-123	KUJ-87123	148.78 m	taken in ore zone
			massive Mt + Ap + Act rich in Mt, little gangue
KUJ10-123	KUJ-87123	148.08 m	taken in ore zone close to HW contact
			massive Mt + Ap + Act rich in Mt, little gangue
KUJ11-123	KUJ-87123	145.85 m	sample taken in HW
			Mt patch and disseminated Mt + KF + Bio + Ap rich in gangue
KUJ12-123	KUJ-87123	242.09 m	taken in FW/ ore contact
			massive Mt + Bio + Ap + Act
KUJ13-123	KUJ-87123	259.99 m	taken in FW
			disseminated Mt + Tit + KF + Act rich in gangue

Table 6.3 Brief sample description of mapped sample KUJ14-221 to KUJ34-163 with sampled intervals.

KUJ14-221	KUJ-87221	209.15 m	taken directly at HW/ ore contact
			layered Mt + Ap + Bio + KF
KUJ15-221	KUJ-87221	220 m	taken in ore zone (close to HW)
			massive Mt + Ap rich in Mt, little Ap
KUJ16-221	KUJ-87221	324.72 m	taken in ore zone
			massive Mt + Act rich in Mt and Act
KUJ17-221	KUJ-87221	317.45 m	taken in ore zone close to FW
			massive Mt + Act + Ap rich in Mt, little gangue
KUJ18-221	KUJ-87221	439.0 m	taken in FW
			Mt patch + KF + Ap rich in Mt, little gangue
KUJ19-221	KUJ-87221	426.70 m	taken in FW
			Mt patch + Act + Bio
KUJ20-114	KUJ-87114	199.34 m	taken in ore zone
			massive Mt + Ap + Act rich in Mt, little gangue
KUJ21-114	KUJ-87114	278.77 m	taken in ore zone
			massive Mt + Ap rich in Mt, very little Ap
KUJ22-114	KUJ-87114	294.53 m	sample taken in FW
			massive & veined Mt + KF + Ap + Tit + Bio + Act rich in gangue
PG23-156	PG-81156	260.03 m	taken in ore zone close to HW
			layered Hem + Ap rich in Ap
PG24-156	PG-81156	292.08 m	taken in ore zone
			Hem patch + Ap + Cal
PG25-156	PG-81156	297.45 m	taken in ore zone
			Mt patch + Ap + Cal + Chl
PG26-156	PG-81156	331.85 m	taken in ore zone
			dense Mt dissemination + Act + Tit + Ap
PG27-165	PG-81165	309.59 m	taken in ore zone massive Mt + Ap + Alb rich in Mt, little gangue
PG28-165	PG-81165	314.50 m	taken in ore zone
			massive Mt + Hem + Ap little Ap
PG29-165	PG-81165	330.62 m	taken in FW
			disseminated Mt, lim, rich in gangue, strongly altered
PG30-617	PG-81617	913.40 m	taken in ore zone
			massive Mt & Hem + Ap clasts
PG31-617	PG-81617	926.10 m	taken in ore zone
			massive Mt & Hem+ Ap clasts
PG32-617	PG-81617	1093.96 m	taken in ore zone
			massive Hem & Mt layering + Ap clasts
PG33-163	PG-81163	187.60 m	taken in ore zone
			layered Hem & relict Mt layering + Cal + Qz
DB34-163	PG-81163	189.90 m	taken in ore zone
			layered Hem & Hem veining + Qz + KF + Cal

7 Methodology

7.1 Sample Preparation

Drillcore samples (>1 kg) were cut in half. Part of each sample split was crushed and then milled to analytical fineness using a tungsten-carbide swing mill in the "Technicum" of the Institute of Mineral Processing at RWTH Aachen University. The other half was send to Clausthal University of Technology for preparation of polished thin sections for transmitted and reflected microscopy and for EMPA.

7.2 Bulk Rock Analysis of the Drillcores

The bulk rock composition of the nine drillholes was determined by inductively coupled plasma-optical emission spectroscopy (ICP-OES) and multi-element X-ray fluorescence spectroscopy (ME-XRF). The analyses were conducted by LKAB using ME-ICP06 and ME-XRF21n. A total of 55 elements and element oxides were analyzed in the KUJ cores, 65 in the PG cores. Note that not the entire drillcore was geochemically investigated, only the parts where at least 50% ore was found during logging. This includes not only the ore zone, but also a range of about 100 m into HW and FW, which equally represents the area of interest for this project.

7.3 Petrography

Microscopy of all polished thin sections was done using a LEICA DFC295 polarization microscope at the Institute of Mineralogy & Economic Geology at RWTH Aachen University. Main goals were to ensure equilibrium conditions between ore and gangue minerals on the microscale and to choose, based on these results, samples for electron microprobe analysis. Further examination included the identification of all gangue and ore/opaque minerals in the samples as well as to characterize and describe textural parameters including ore texture, grain-size variations and to assess the degree of alteration.

7.4 Electron Micoprobe Analysis (EMPA)

Electron microprobe analysis (EMPA) was used for spot analysis of major, minor and trace element composition of apatite and magnetite grains. The analysis was performed at the Institute of Mineralogy & Economic Geology at the RWTH Aachen University using a JEOL JXA-8900R microprobe. Al, Ca, Co, Cr, Fe, Mg, Mn, Mo, Nb, Ni, Si, Sn, Ti, V, W, Y and Zr were analyzed in magnetite grains and As, Ca, Ce, Cl, F, La, P and Zr in apatite grains from a total of four Kiirunavaara- and four Per Geijer samples. Detection limits for apatite are listed in table 7.2 and for magnetite in table 7.1. A 15 μm beam size was used for apatite measurements and a 1 μm for magnetite measurements. In-house standards were used for calibration. Detailed measuring conditions can be found in the appendix.

Table 7.1 Measurement conditions for apatite.

Element in apatite	Peak [mm]	Net [cps]	S.D [%]	D.L [ppm]
As	105.15	0.4	100	343
F	199.28	10.8	4.28	546
P	197.17	791.3	0.8	184
Ca	107.50	5055	0.45	188
Ce	178.24	0.7	79.70	248
Zr	194.41	1.6	23.98	333
Cl	151.46	3.2	18.78	73
La	185.44	0.6	100	256

Table 7.2 Measurement conditions for magnetite.

Element in magnetite	Peak [mm]	Net [cps]	S.D [%]	D.L [ppm]
Mg	107.50	2.9	39.19	86
Sn	115.07	6.2	37.36	233
Y	206.50	0.4	122.06	299
Ca	107.51	2.3	100	134
Fe	134.97	28458	0.19	149
Al	90.58	9.0	24.83	112
V	79.86	28.6	8.75	110
Nb	183.33	0.2	374.17	171
Ti	87.91	1.4	100	98
Ni	115.74	0	100	98
Si	77.33	28.6	8.69	82
Mo	173.21	0	100	307
Co	124.81	46.0	6.1	97
W	75.79	0.3	851.66	210
Mn	146.49	0.9	100	130
Cr	159.45	34	56.80	90

7.4.1 Calculation of OH in Apatite

Since the direct analysis of OH in apatite by EMPA is precluded, the OH content of apatite was calculated as difference to F and Cl to obtain the complete halogen composition of the apatites. Therefore, the method after Picolli & Candela (2002) was used assuming that the halogen site is full. FAp represents the mole fraction of fluorapatite and is calculated using equation (7.1) with C_F^{Ap} being the concentration of F in apatite in wt%. ClAp represents the mole fraction of chlorapatite and is calculated via equation (7.2) with C_{Cl}^{Ap} being the concentration of Cl in wt%. The OH concentration can then be calculated using equation (7.3).

$$X_{FAp}^{Ap} = C_F^{Ap}/3.767 \tag{7.1}$$

$$X_{ClAp}^{Ap} = C_{Cl}^{Ap}/6.809 \tag{7.2}$$

$$X_{OHAp}^{Ap} = 1 - X_{FAp}^{Ap} - X_{ClAp}^{Ap} \tag{7.3}$$

7.5 Inductively Coupled Plasma Mass Spectrometry (ICP-MS)

Conventional inductively coupled plasma mass spectrometry (ICP-MS) was conducted on milled pulps of all 34 samples at SGS Bulgaria, Bor Laboratory/Serbia. At total of 48 elements (Ag, Al, As, Ba, Be, Bi, Ca, Cd, Ce, Co, Cr, Cs, Cu, Fe, Ga, Hf, In, K, La, Li, Lu, Mg, Mn, Mo, Na, Nb, Ni, P, Pb, Rb, S, Sb, Sc, Se, Sn, Sr, Ta, Tb, Te, Th, Ti, Tl, U, V, W, Y, Yb, Zn, and Zr) were analyzed after HNO_3-HF-$HClO_4$ and HCl digestion of the sample aliquot. Digestion with four acids ensured complete dissolution, except for the refractory elements, of the samples and allowed the detection of total metals. Detection limits can be found in table 8.2. Analysis of duplicates and internal standards give evidence for high quality. Detailed ICP-MS procedure can be found in Olesik (1991).

7.6 Data Analysis

Several statistical methods were performed, including the calculation of mean, min and max values, in order to evaluate the geochemical data. However, min and max values are (when considering trace elements mainly min values) defined by analytical detection limits, therefore boxplots were chosen for data visualization of the most important trace elements that show lower quartile, median, upper quartile, as well as statistical outliers. In addition, correlations between all elements in the ICP-MS and EMPA data were determined by calculating the correlation coefficient after Schober et al. (2018), using equation (7.4). The correlation matrices are shown in the appendix.

$$\mathrm{Korr}(X,Y) = \frac{\mathrm{Cov}(X,Y)}{\sqrt{\mathrm{Var}(X)}\sqrt{\mathrm{Var}(Y)}} = \frac{\sigma_{X,Y}}{\sigma_X \sigma_Y} =: \rho_{X,Y}. \tag{7.4}$$

Since statistical outliers, including analytical artefacts like parallels to x-axis or y-axis, can have a great influence on the correlation coefficient (cc), the data of all element pairs were subsequently visually checked in order to verify that a clear correlation was given.

7.7 Magnetite Discrimination Diagrams

Two modified trace element discrimination diagrams were used in chapter 9 in order to differentiate between magmatic and hydrothermal ore. The first one distinguishes between magmatic and high-T hydrothermal magnetite. The diagram was elaborated by Dare et al. (2014a) and is based on factors controlling element substitution in magnetite:

- "the concentration of the element in the liquid from which it crystallizes.
- Whether other minerals crystallizing at the same time are competing for that element.
- The partition coefficient of the element into magnetite, which can vary up to several orders of magnitude with composition of the silicate melt, temperature, pressure, oxygen fugacity (fO_2), and cooling rate" (Dare et al. 2014a).

Figure 7.1 Discrimination diagram for magmatic and high-T hydrothermal magnetite. Modified version after Dare et al. (2014a) created with Python.

The trace elements are plotted along the x-axis in order of increasing compatibility into magnetite, using the compilation of experimental and empirical partition coefficients

between magnetite and silicate magmas (Dare et al., 2012). The magnetite data to be plotted into the diagram is normalized to bulk continental crust.

The second diagram elaborated by Dare et al. (2014a) differentiates between low T-hydrothermal and high-T hydrothermal magnetite. Compared to high-T hydrothermal-, magnetite forming from lower-T fluids are depleted in elements like Co, V, Ni or Cr that are compatible with magnetite during fractionation. Dare et al. (2014a) explain this by low solubility of these elements in fluids at lower temperatures. As a result, they have the lowest overall abundance of trace elements.

Figure 7.2 Discrimination diagram for low-T hydrothermal and high-T hydrothermal magnetite. Modified version after Dare et al. (2014a) created with Python.

8 Results

8.1 Bulk Rock Geochemistry of the Drillcores

Due to the very large size of the drillcore data sets, they included on the CD that comes attached with this work. The host rocks from Kiirunavaara (and the HW in PG) show a mineralogy typical for volcanic rocks. Quartz content is negatively correlated with ore content and ranges from 1.26 wt% to 71.1 wt%. Quartz content in Per Geijer is variable as well and dependant on the ore content with values ranging from 5.11 wt% to 72.5 wt%. The mudstone and greywacke (HW) in Per Geijer are as well dominant in quartz. Figure 8.1 shows that in Kiirunavaara such as Per Geijer rocks from HW and FW are mainly of intermediate and partly of mafic and felsic composition.

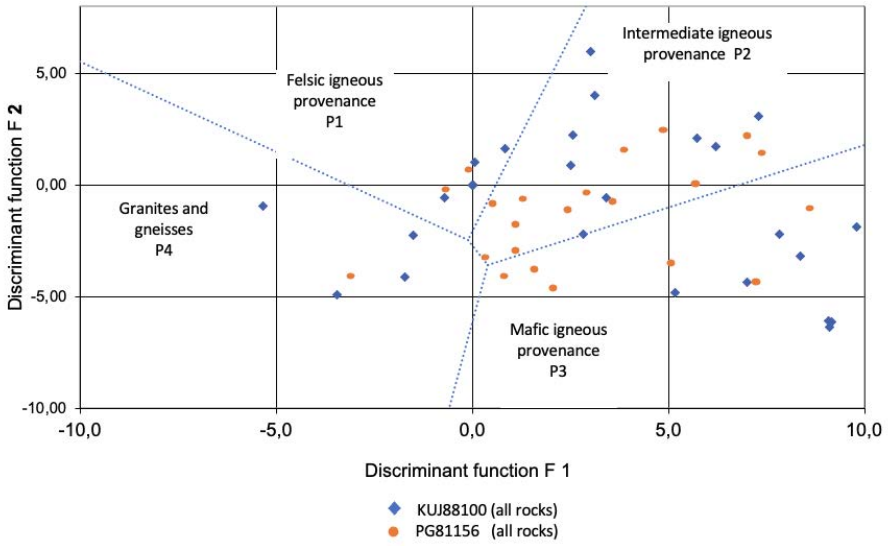

Figure 8.1 Discriminant plot after Roser and Korsch (1988) shows that PG and KUJ samples in the example of KUJ-88100 and PG-81156 are of mainly intermediate composition.

8.2 Petrography

This section includes a summary of the petrographical results. Pictures of the thin section can be found int the appendix.

8.2.1 Ore Minerals - Kiirunavaara

The major ore mineral of the samples from Kiirunavaara is magnetite. The ore shows variations in texture and grain size, but can be grouped into four morphological categories: 1) massive 2) disseminated 3) patched and 4) layered. Only minor hematite as replacement or martitization is found in two samples. The samples that originate from the ore zone (OZ) consist of about 85% ore minerals. Magnetite from the ore zone occurs massive with fine grained anhedral to subhedral crystals of about 10-30 μm diameter (figure 8.3). In sample KUJ21-114 the magnetite is particularly massive, consequently individual grain shapes are hardly recognizable (figure 8.2). Hematite replacement can be observed in sample KUJ20-114.

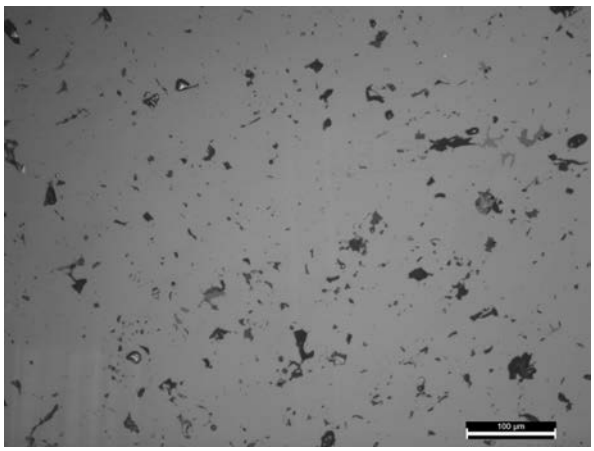

Figure 8.2 Massive magnetite from ore zone sample KUJ21-114. Grain boundaries are not noticeable.

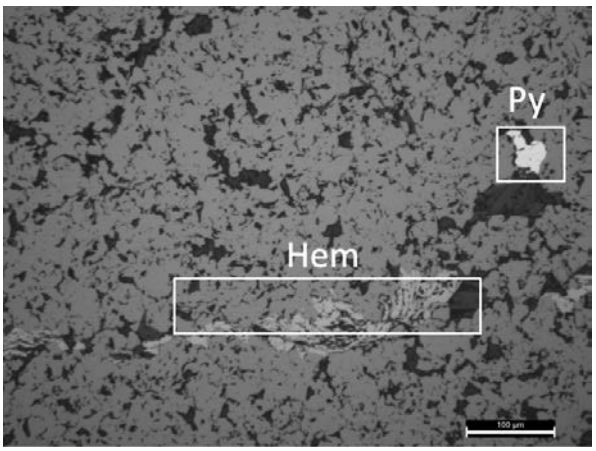

Figure 8.3 Massive magnetite from ore zone sample KUJ20-114, little hematite replacement and an anhedral pyrite grain in the top left.

.

Ore category 2) - 4) is found in the host rock samples, where the ore content ranges between 5% and 75%. Disseminated magnetite occurs in different grainsizes from anhedral to subhedral shape with grain diameter ranging from to 20 μm (figure 8.5) to 100 μm (figure 8.6). The disseminated magnetite generally has a larger grain size than the one from the ore zone and is often associated with leucoxen dissemination or intergrown with it (figure 8.4). Magnetite patches are composed of clusters of anhedral magnetite with crystals of 20-80 μm (figure 8.7) diameter.

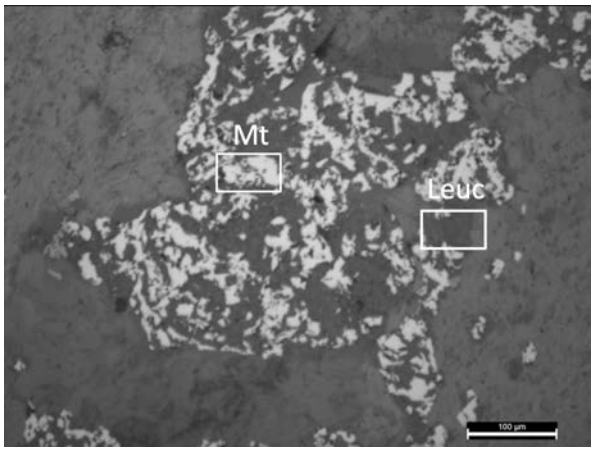

Figure 8.4 Intergrown magnetite and leucoxen from FW sample KUJ4-100.

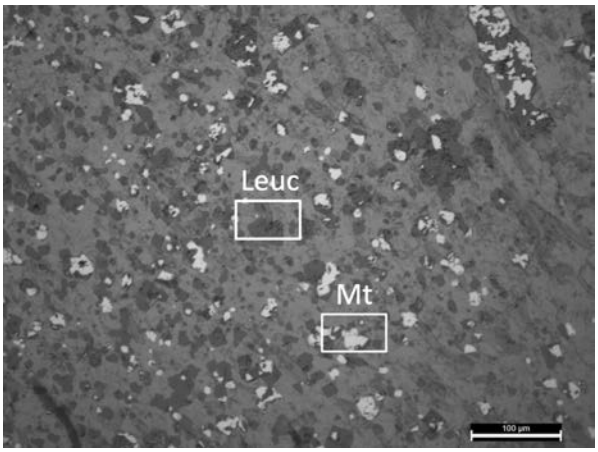

Figure 8.5 Anhedral magnetite and subhedral leucoxen dissemination from FW sample KUJ3-100.

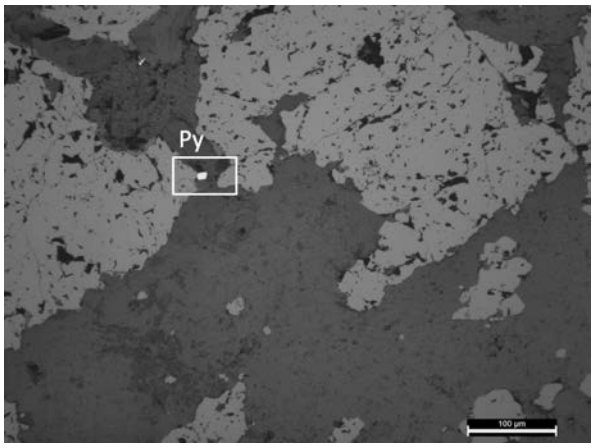

Figure 8.6 Magnetite dissemination and anhedral pyrite grain from FW sample KUJ13-123.

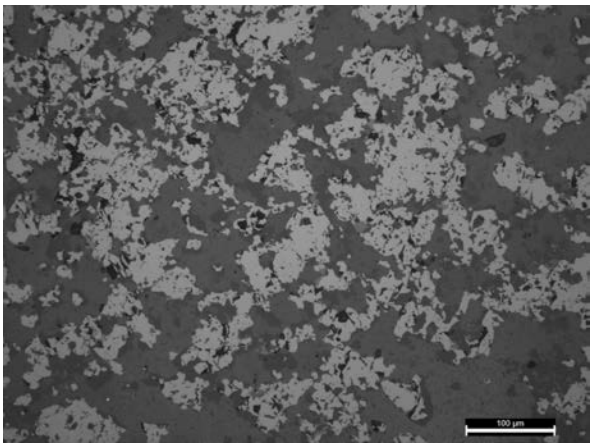

Figure 8.7 Semi massive magnetite from ore patch of HW sample KUJ07-115.

Layers are characterised by anhedral crystals of 50-100 μm diameter with sharp boundaries between the gangue minerals. Pyrite and chalcopyrite occur in almost every thin section in accessory quantity.

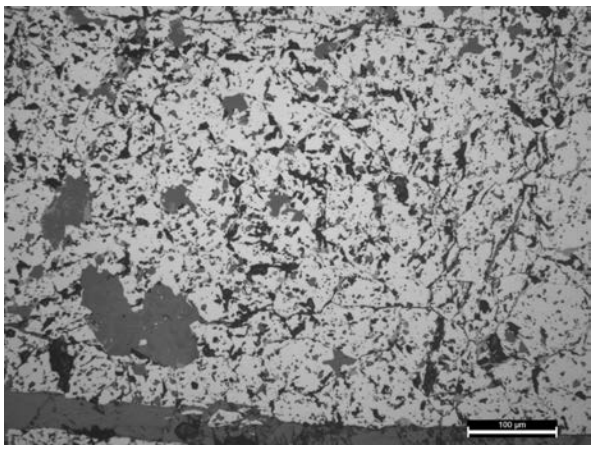

Figure 8.8 Massive magnetite from ore band in FW sample KUJ18-221.

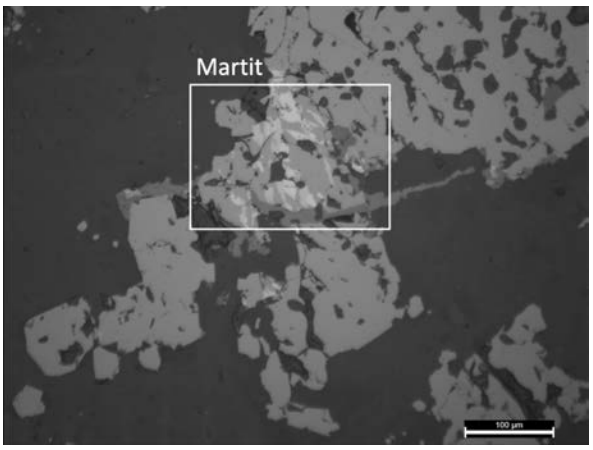

Figure 8.9 Martitization from FW sample KUJ18-221.

8.2.2 Ore Minerals - Per Geijer

The samples from the Per Geijer deposit originate all from the ore zone, except FW sample PG29-165. Their ore mineral content ranges from 12% to 86%, whereas the FW sample has an ore content of only 7%. The main ore minerals are hematite and magnetite (average: 60% Hem; 40% Mt), except for FW sample PG29-165, where the main ore mineral is limonite. Goethite is found in several samples in low quantities. Grain size and texture strongly differ from sample to sample. Again the ore can be grouped into four categories 1) massive 2) disseminated 3) patched 4) layered. However, unlike the Kiirunavaara samples, where the ore within one category has a similar appearance, the ore of the Per Geijer samples also differs greatly within each category with respect to grain size and texture. Some samples show deformation features. In the majority of the samples the ore occurs massive and consists of either hematite with small amounts of relict magnetite of 10 μm diameter (figure 8.10) or phenocryst like magnetite up to 100 μm diameter within a fine grained hematite groundmass (figure 8.12) or coarse grained hematite mass (figure 8.13). Where hematite occurs as massive ore, ilmenite

exsolution is a common feature. PG32-617 is the only sample where the major ore mineral (>90%) is magnetite. The ore occurs massive with grain size ranging from 10-20 μm diameter (figure 8.11). Magnetite dominates as well in sample PG31-617 and

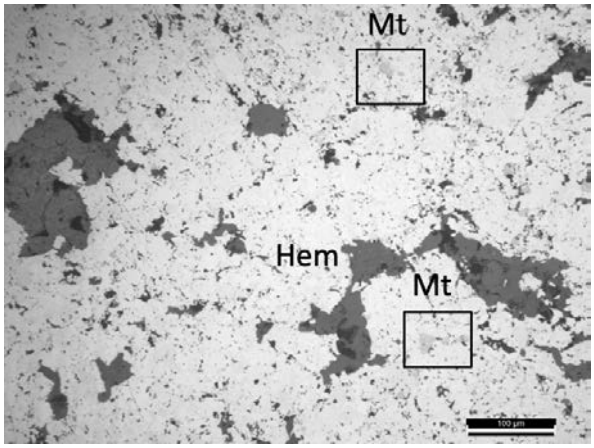

Figure 8.10 Massive hematite with relict magnetite crystals of OZ sample PG24-156.

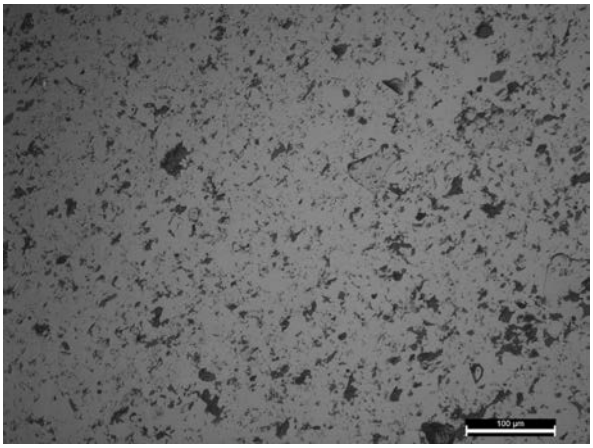

Figure 8.11 Massive magnetite from OZ sample PG32-156.

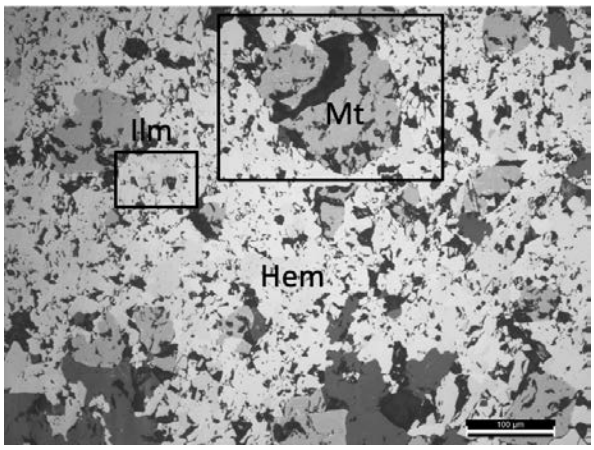

Figure 8.12 Massive hematite groundmass with coarse grained magnetite crystals and ilmenite exsolution patches from OZ sample PG27-165.

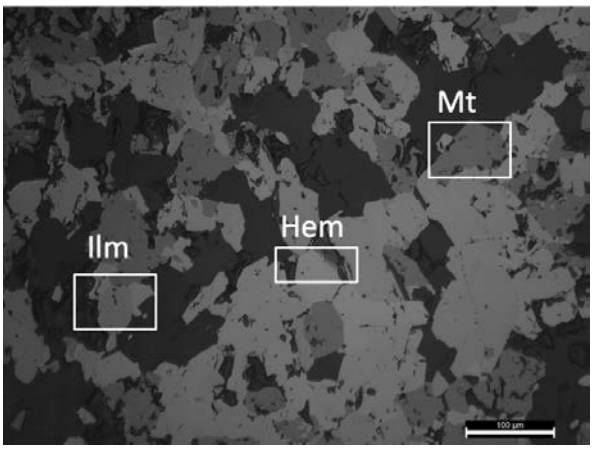

Figure 8.13 Semi massive hematite intergrown with magnetite and ilmenite exsolution patches of sample PG31-617.

PG30-617. In contrast, sample PG23-156 consists of only hematite, which appears as dense dissemination of 10-20 μm diameter (figure 8.15). Sample PG23-156 has probably undergone a deformation process, since the hematite grains have a brittle appearance. A relationship between magnetite content and depth was determined. The samples with only hematite originate from the most shallow parts of the system. Borehole PG-81617 constitutes the deep part of Henry, the magnetite content here increases along the borehole and is highest (>90%) in the deepest sample from 1093 m below surface. Dissemination is also present as needles with length up to 150 μm, where magnetite is

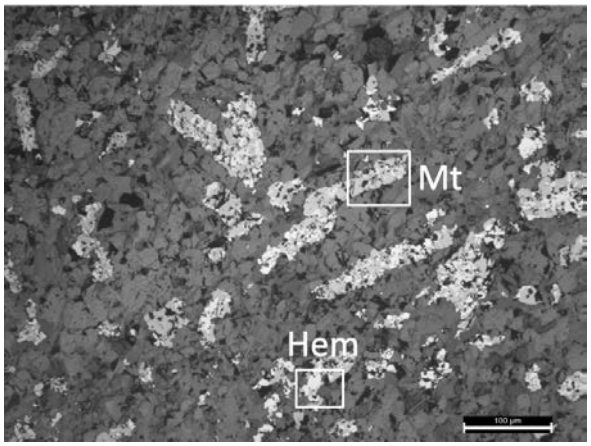

Figure 8.14 Needles of intergrown magnetite and hematite from disseminated OZ sample PG26-156.

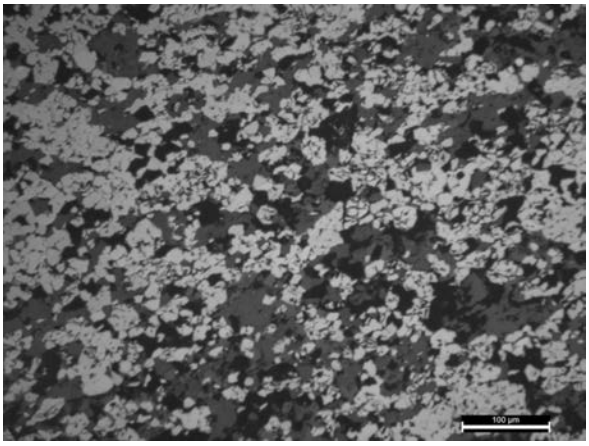

Figure 8.15 Dense hematite dissemination with brittle appearance from sample PG23-156.

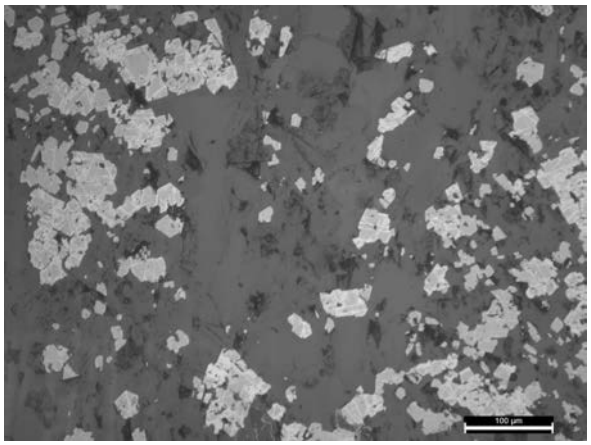

Figure 8.16 Magnetite dissemination with martitization from FW sample PG29-165.

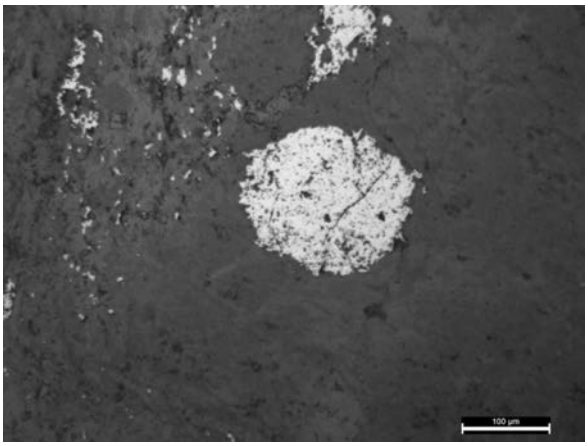

Figure 8.17 Well rounded hematite dissemination from ore zone sample PG34-163.

intergrown with hematite (figure 8.14), such as anhedral rectangular magnetite of about 10-50 μm grain diameter with martitization (figure 8.16). In the samples where the ore occurs layered hematite appears as well rounded dissemination with diameter of 120 μm (figure 8.17) or as rectangular magnetite dissemination of about 100 μm grainsize (figure 8.18). The small grains around the martites in PG28-165 are already fully oxidized to hematite. In sample PG25-156 the ore is present as patch of semi massive magnetite, where anticipating martitization appears on the magnetite rims (figure 8.20). An inverse relationship between depth and degree of martitization was observed. Samples closer to surface show a stronger degree of martitization. In sample PG33-163 the layered ore occurs as semi massive hematite patch. The ore here has a stretched appearance implying a local deformation event. Sulfides including pyrite and chalcopyrite were also found in the PG samples, but are less common than in Kiirunavaara.

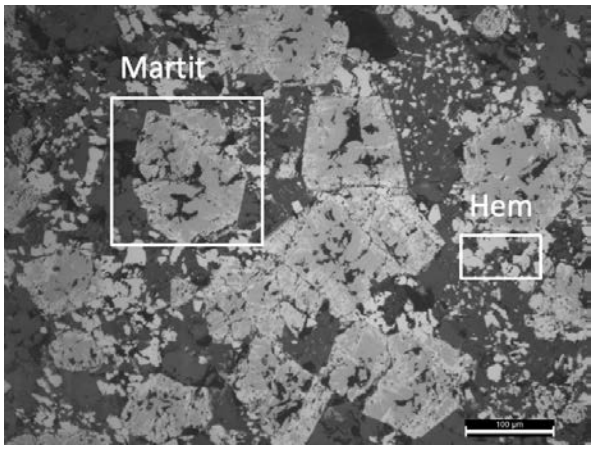

Figure 8.18 Magnetite dissemination with martitization from layered ore zone sample PG28-154.

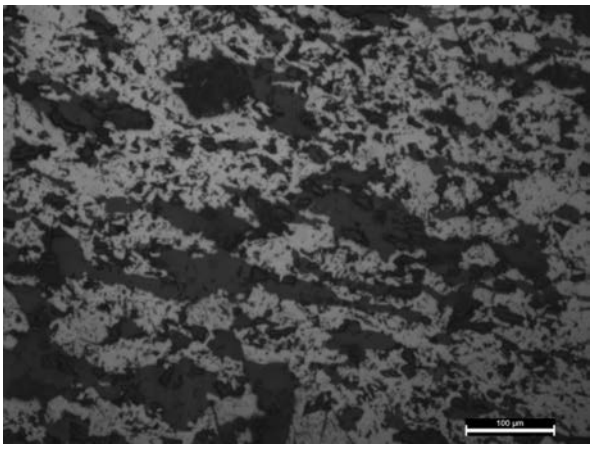

Figure 8.19 Semi massive stretched hematite from layered OZ sample PG33-163.

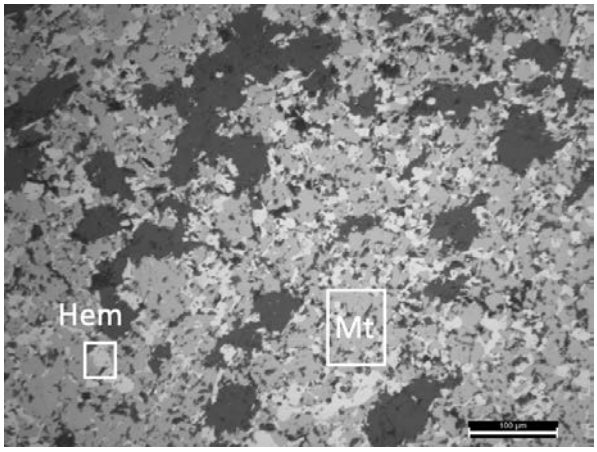

Figure 8.20 Semi massive magnetite with anticipating martitization from OZ sample PG25-156.

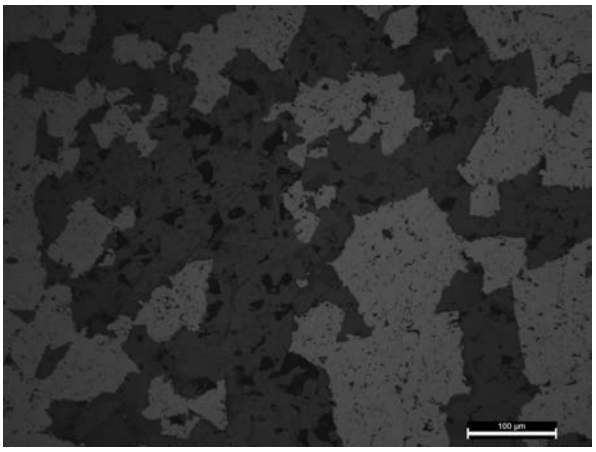

Figure 8.21 Hematite dissemination from ore zone sample PG24-156.

8.2.3 Gangue Minerals - Kiirunavaara

The ore zone samples from Kiirunavaara consist of about 10-20% gangue minerals. Based on the ganuge minerals, the magnetite is associated with, the ore zone is classified as D and B ore. If the ore is associated with interstitial apatite, biotite and sometimes calcite its classified as D-ore (high P) (figure 8.23). Apatite is here the dominant gangue mineral phase ± actinolite, plagioclase, and quartz. The B-ore is characterized by minor amounts of interstitial biotite, calcite, and apatite (P-poor ore) (figure 8.22). Titanite and chlorite occur in accessory quantity within the OZ.

The host rock samples consist of about 90-30% gangue minerals and feature a mineralogy typically for volcanic rocks. Major gangue mineral in both the trachyandesite and the rhyodacite is quartz, which mainly represent the groundmass. Further common gangue minerals are feldspar, mica, (both biotite and muscovite) and actinolite. Titanite, apatite, zircon and epidote are present in low quantities. These minerals commonly occur as bigger crystals within the fine grained quartz groundmass (figure 8.24, figure 8.25). Secondary minerals including chlorite and calcite are also common and are more prominent in the FW that generally shows a higher degree of alteration than the HW.

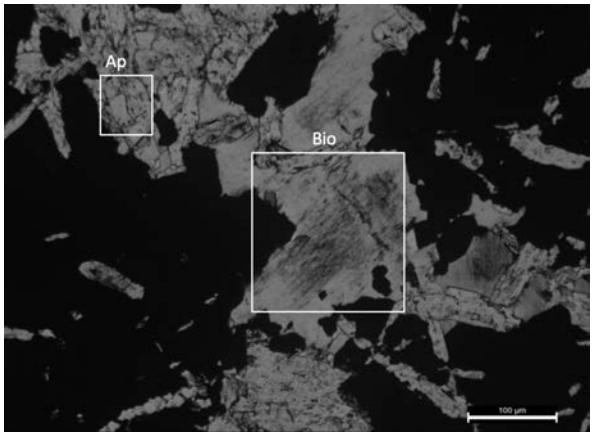

Figure 8.22 Biotite surrounded by ore and needles of apatite in OZ sample KUJ12-123 (B-ore).

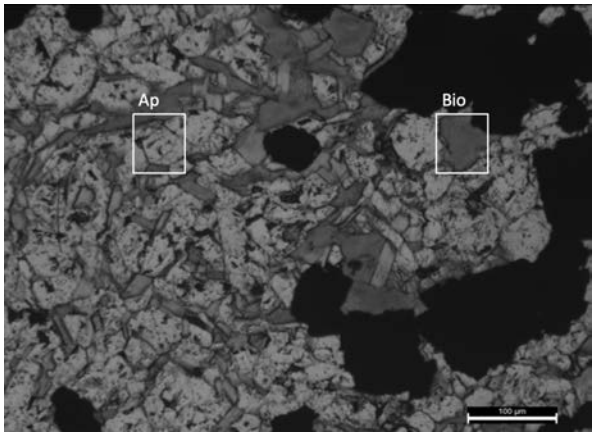

Figure 8.23 Clusters of apatite and interstitial biotite in OZ sample KUJ17-221 (D-ore).

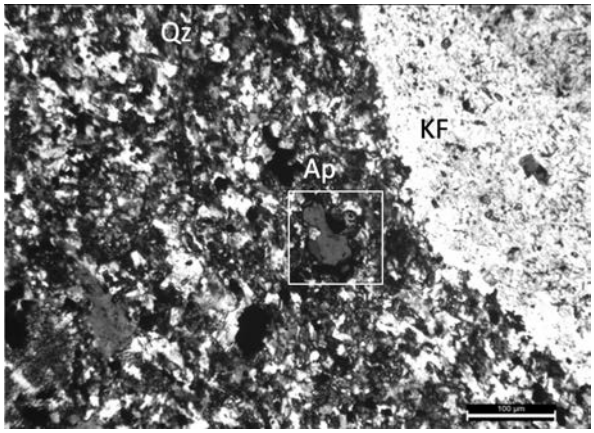

Figure 8.24 Anhedral apatite crystal within quartz groundmass and a feldspar phenocryst on the right in FW sample KUJ6-115.

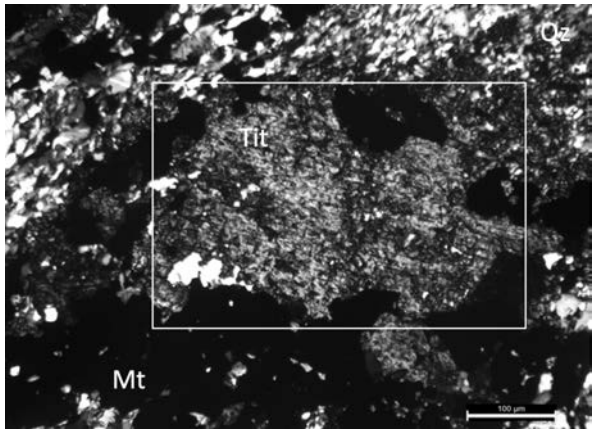

Figure 8.25 Titanite crystal in the center surrounded by opaque magnetite within a quartz groundmass in HW sample KUJ1-100.

Based on the results from the microscopy, samples for EMPA were chosen. The deciding factor therefore was the degree of alteration estimated based on the presence of secondary minerals that do not belong to the magmatic phase, like chlorite and calcite and further the presence of apatite in several generations. Sample KUJ1-100, KUJ4-100, KUJ9-123, KUJ13-123 and KUJ17-221, KUJ19-221 were chosen for EMPA.

8.2.4 Gangue Minerals - Per Geijer

The Per Geijer ore zone samples consist of about 30% gangue minerals in the ore zone, whereas the FW sample PG29-165 consist of 93% gangue minerals. Major gangue minerals in the PG OZ samples are quartz and apatite. They occur interstitially with the ore. Mica (biotite > muscovite), allanite, epidote, and chlorite were detected in every sample. Calcite and feldspar are common and were found in about half of the samples. Small amounts of zircon >1% were detected in PG31-617 and PG33-163. The PG ore zone samples show an overall moderate degree of alteration. Secondary minerals like calcite and chlorite occur more often and in large quantities indicating a higher degree of alteration than in Kiirunavaara. Some samples (PG24-156, PG27-165, PG29-165) have a chloritized and carbonatized groundmass or propylitic altered groundmass. In those samples the alteration from calcite to clay minerals could also be well observed. The samples from shallow to intermediate depth show a higher degree of alteration than the samples from depth. Sample PG23-156 and PG33-163 have deformation features. In PG23-156 the apatite crystals show a brittle appearance (figure 8.26), in PG33-163 they are stretched (figure 8.27). These features are consistent with the observations from the ore microscopy.

The host rock sample PG29-165 differs from the other PG samples in several ways. The sample consists of a chloritized and carbonatized groundmass that has quartz porphyroblasts within it. Degree of alteration is strong. Main minerals are chlorite, calcite, quartz, muscovite, scapolite and clay.

Sample PG26-156, PG28-165, PG31-617 and PG33-163 were chosen for EMPA analysis due to the presence of apatite crystals in several generations and low degree of alteration compared to the other PG samples.

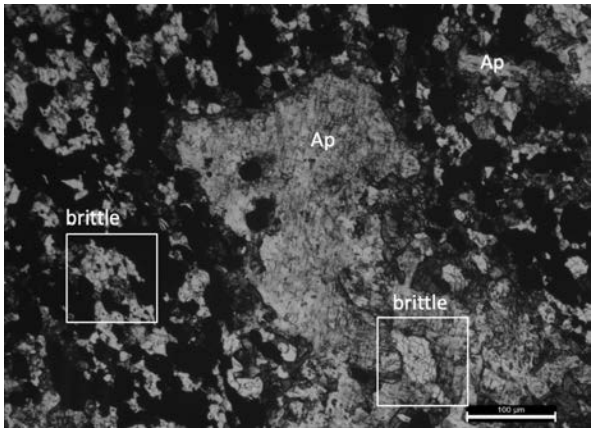

Figure 8.26 Apatite grains with brittle appearance from OZ sample PG23-156.

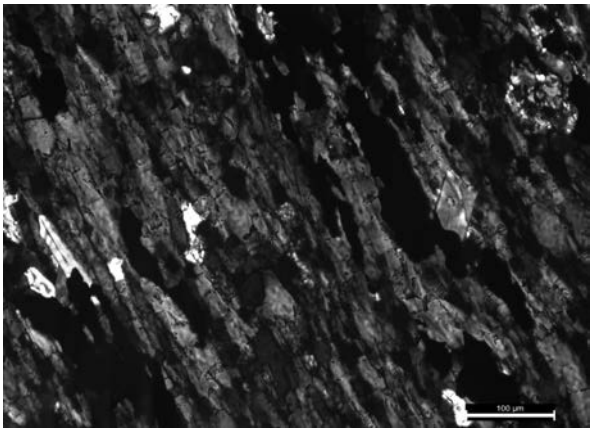

Figure 8.27 Stretched apatites from ore zone sample PG33-163.

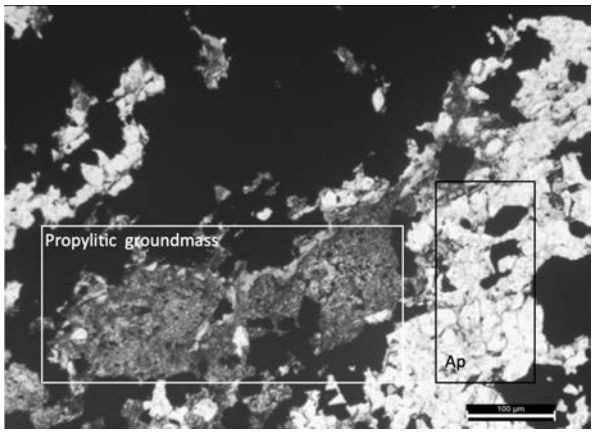

Figure 8.28 Propylitic groundmass and apatite crystals from OZ sample PG24-156.

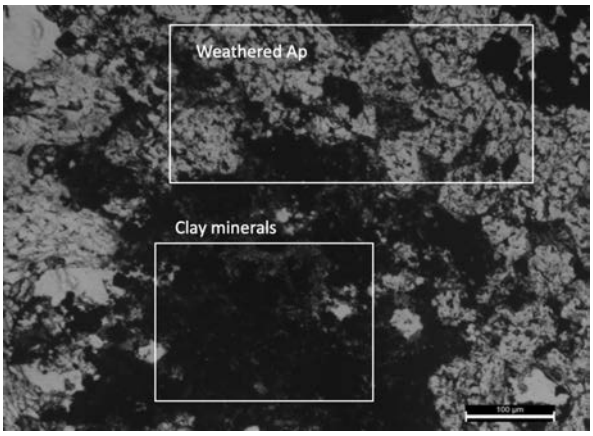

Figure 8.29 Clay minerals surrounded by weathered apatites from OZ sample PG27-165.

8.2.5 Apatite Textures

The apatites that were measured by EMPA were studied with a coupled SEM. Since apatite is a mineral of special interest within the scope of this study, the textures occurring in this mineral are closely examined. The apatites from KUJ that originate from the host rock zone and that are associated with disseminated ore (KUJ4-100; KUJ13-123) are generally undeformed and free of inclusions (figure 8.30). The apatites from the KUJ ore zone (KUJ17-122) and the ones from the host rock that are associated with layered and patched ore (KUJ1-100; KUJ19-221) are partly porous and contain fractures (figure 8.31). Few of them contain monazite inclusions (figure 8.38). Many of the apatite crystals in KUJ are zoned displaying a lighter grey within the crystal core and a darker grey towards the rim (figure 8.35, figure 8.34). These features are not observed in the host rock samples KUJ4-100 and KUJ13-123. In sample KUJ17-221, KUJ1-100 and KUJ19-221 almost all apatite crystals show this kind of zonation. In Per Geijer the samples that originate from shallow and intermediate depth are heavily altered (PG26-156, PG28-165 and PG33-163) (figure 8.32, figure 8.33). They are porous and contain many fractures. The apatite in those samples is associated with disseminated and layered ore respectively. These features become less with depth. Apatites from Per Geijer display the same zonation that is observed in KUJ (figure 8.36, figure 8.37). Only the deep sample PG31-617 that is associated with massive ore does not show any zonation. Monazite inlcusion within the apatites from Per Geijer are very common (figure 8.39), especially in the samples from shallow to intermediate depth.

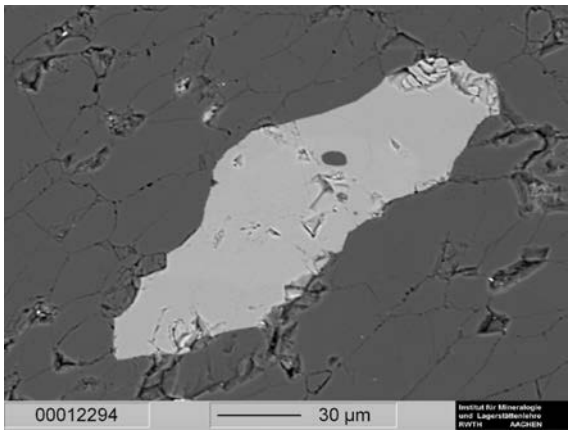

Figure 8.30 SEM image of undeformed/ unaltered apatite crystal from HW sample KUJ1-100.

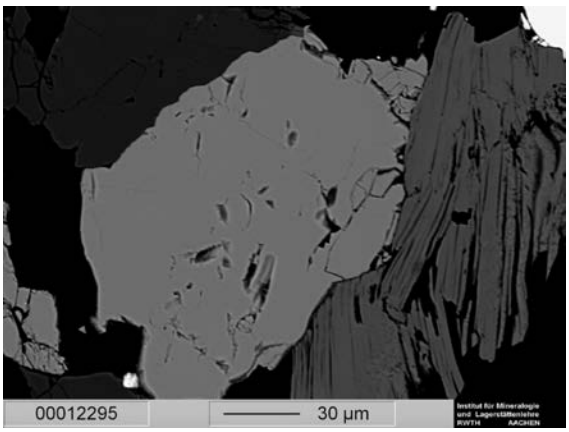

Figure 8.31 SEM image of slightly altered apatite with few fractures from FW sample KUJ19-221.

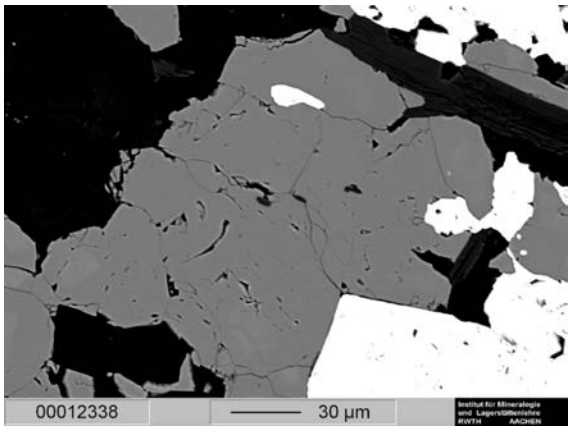

Figure 8.32 SEM image of altered apatite crystals with fractures from OZ sample PG28-165.

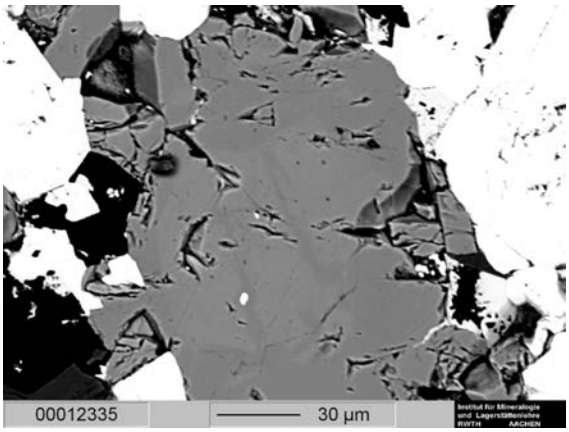

Figure 8.33 SEM image of heavily altered apatite crystals with many fractures from OZ sample PG33-163.

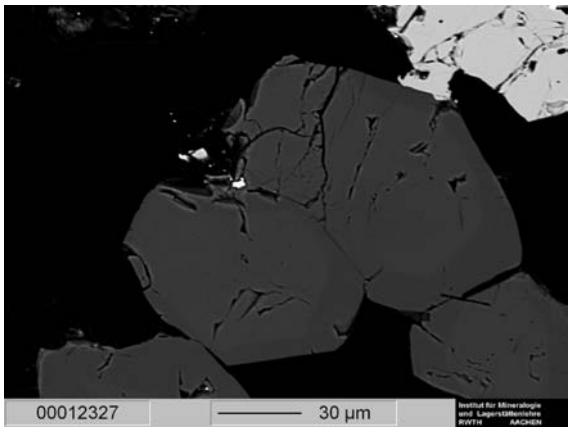

Figure 8.34 SEM image of zoned apatites from OZ sample KUJ19-221.

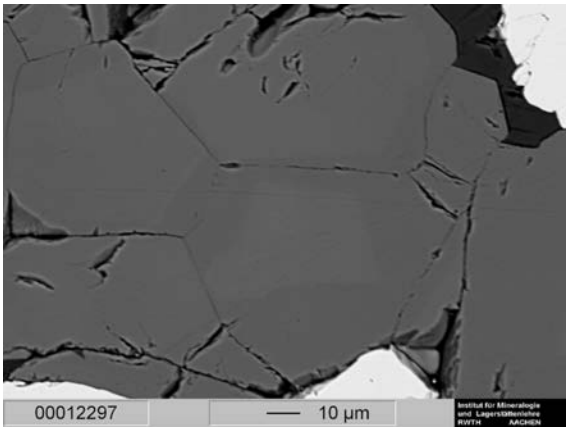

Figure 8.35 SEM image of zoned apatites from OZ sample KUJ17-221.

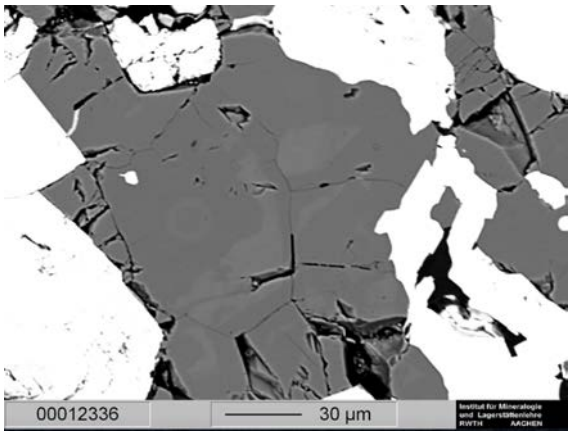

Figure 8.36 SEM image of zoned apatite from OZ sample PG33-163.

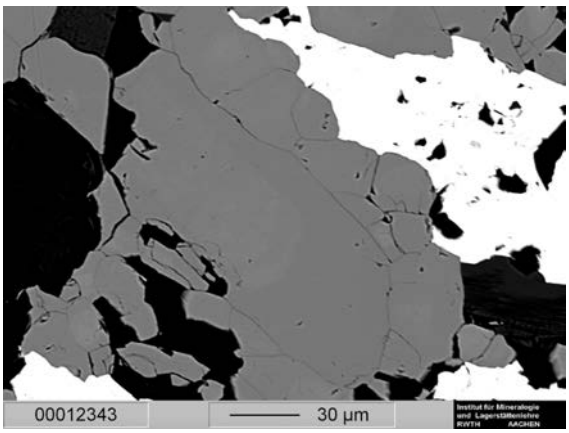

Figure 8.37 SEM image of zoned apatite from OZ sample PG28-165.

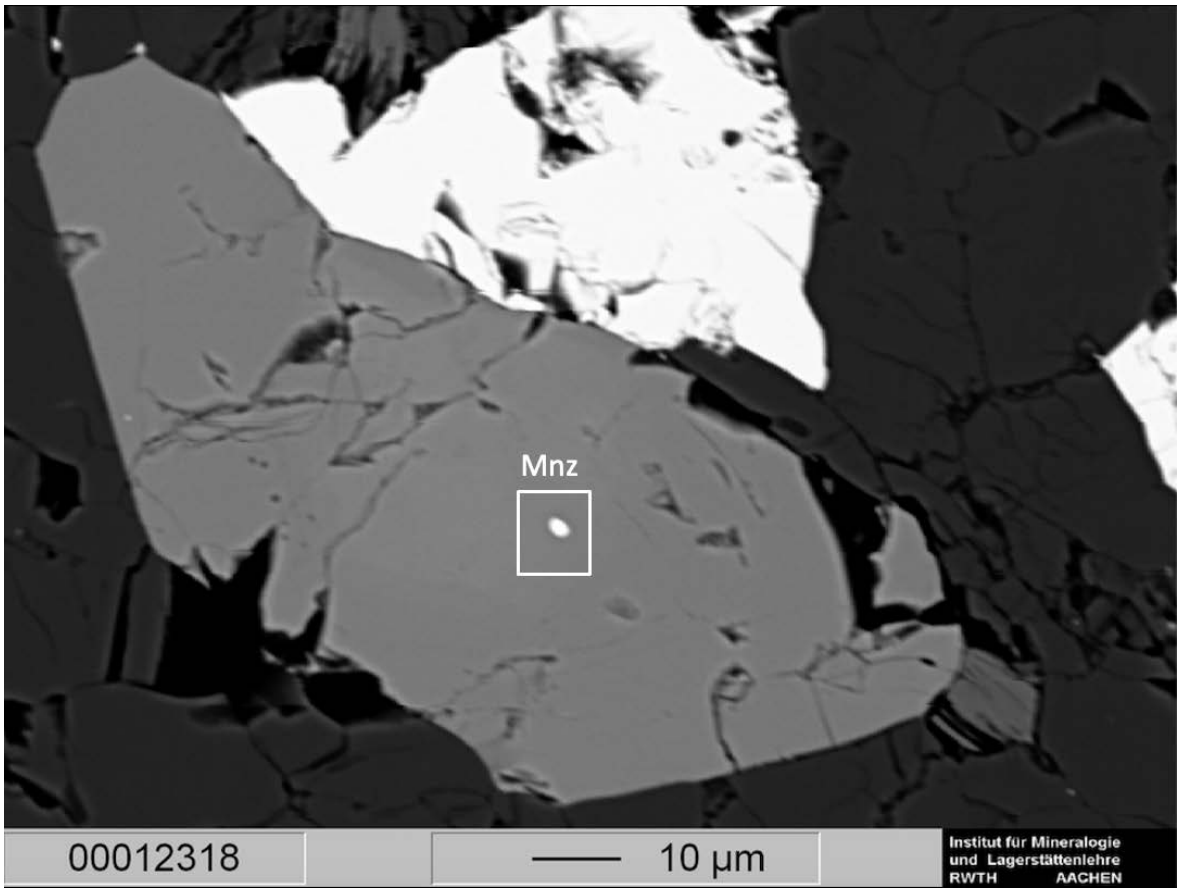

Figure 8.38 SEM image of monazite (Mnz) inclusions in apatite of OZ sample KUJ17-221.

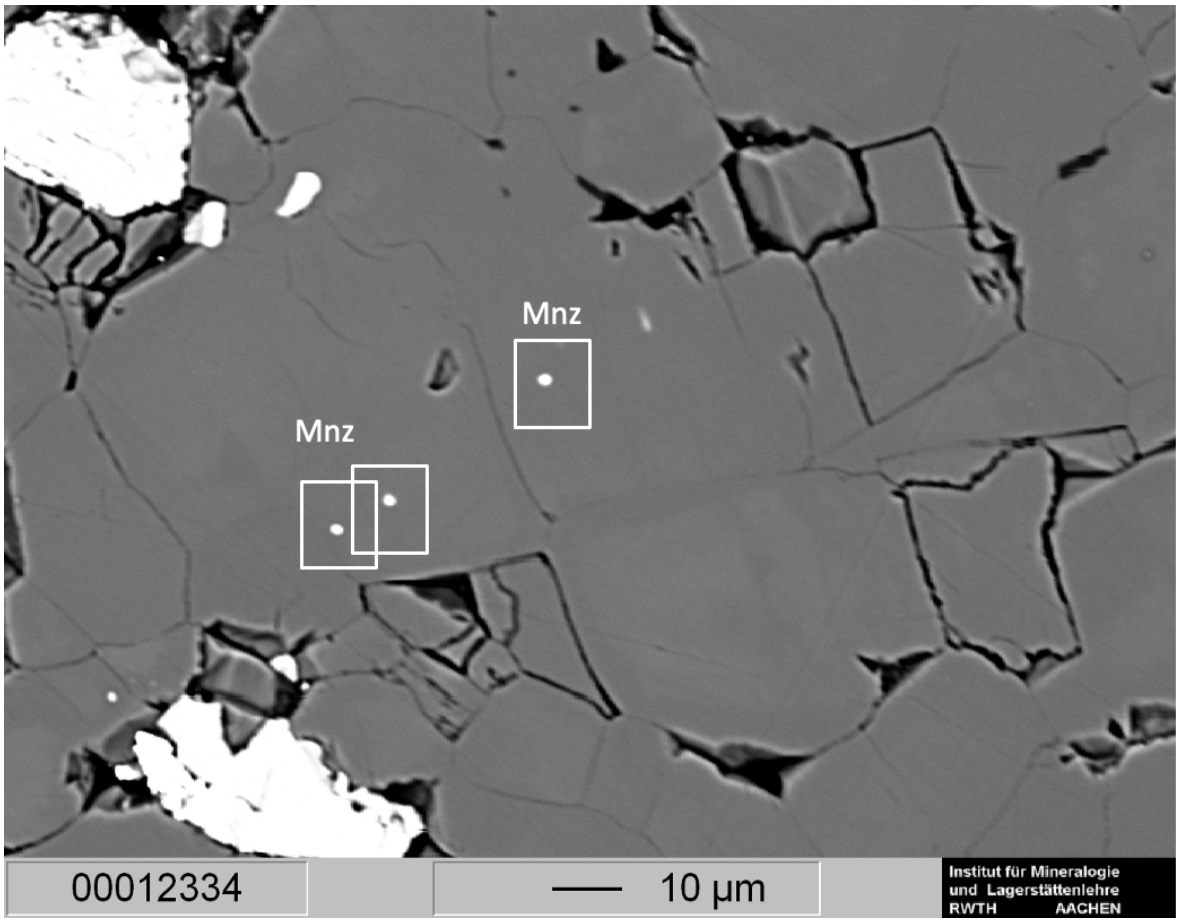

Figure 8.39 SEM image of several monazite inclusions in apatite grains from OZ sample PG33-163.

8.3 Major, Minor and Trace Element Geochemistry of the Samples

Major, minor and trace element composition of the samples was measured by EMPA and ICP-MS. ICP-MS was conducted on pulp samples.

8.3.1 Results determined by ICP-MS

Major, minor and trace element composition determined by ICP-MS is listed in table 8.2 - table 8.4. A summary of all major elements can be found in table 8.1. The mean values of the average major element composition normalized to bulk continental crust (Rudnick, 2003) is illustrated in figure 8.40 to shows which major elements are enriched and which are depleted within the KUJ and PG ore zone and host rock zone. Total iron content is reported as Fe_2O_3. Iron content varies significantly with location. In the Kiirunavaara ore zone samples, the iron content ranges between 80-98 wt% (mean: 90 wt%), in the host rock samples between 6-77 wt% (mean: 45 wt%). Neither a variation in ore grade between the different KUJ boreholes nor a variation in depth is given. The Per Geijer samples have with 12-82 wt% (mean: 32 wt%) in the ore zone and with 7 wt% in the host rock zone a lower iron content. Ore grade increases with depth (figure 8.41). Phosphate content is low in Kiirunavaara with an average 0.2 wt% P_2O_5 in the host rock samples and 0.5 wt% P_2O_5 in the ore zone samples. Only sample KUJ17-221 shows with 4.24 wt% P_2O_5 a value above 1 wt%. In Per Geijer P_2O_5 content is substantially higher with mean values of 6.6 wt% and 0.9 wt% for ore zone and host rock samples, respectively. Sample PG25-156 has with 18.88 wt% the highest P_2O_5 content. K and N values are low in Kiirunavaara and moderate in PG. Especially the ore zone shows a very low degree of alteration with average values of 0.41 wt% K_2O and 0.9 wt% K_2O such as 0.05 wt% Na_2O and 0.26% Na_2O for KUJ and PG, respectively. The PG host rock samples, in contrast, have higher K values with 4.9 wt% K_2O and 0.38 wt% K_2O. TiO_2 contents are higher in Kiirunavaara with values ranging from 0.03

wt% to 1.08 wt% in the ore zone and from 0.13 wt% to 1.42 wt% in the host rock zone, compared to 0.03 wt% and 0.32 wt% in the PG ore zone and to 0.2 wt% in the PG host rock zone.

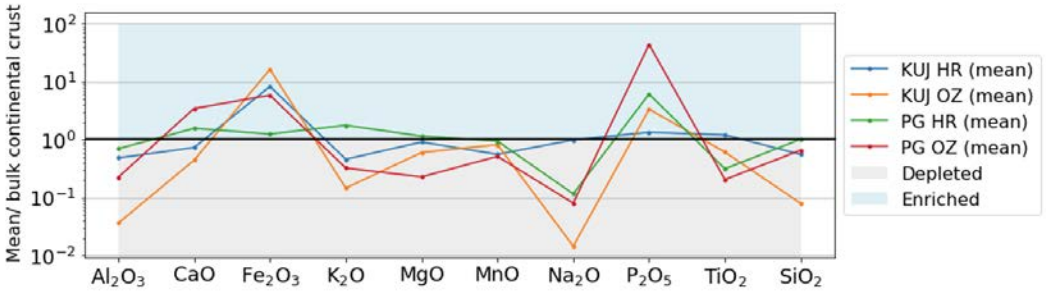

Figure 8.40 Average major elements measured by ICP-MS normalized to continental crust. The composition of the continental crust was taken from Rudnick (2003). Fe_2O_3, P_2O_5 and Na_2O contents differ greatly.

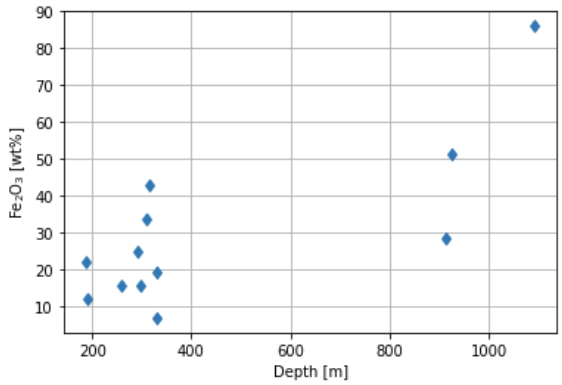

Figure 8.41 Relationship between depth and Fe_2O_3 in Per Geijer. The deepest - samples have the highest iron contents.

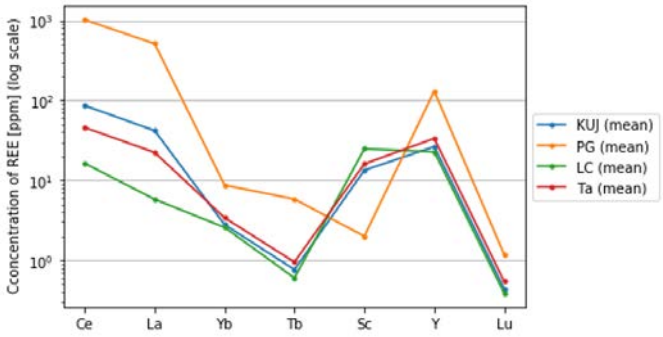

Figure 8.42 REE element composition of KUJ and PG samples compared to other IOA bulk rock samples from Los Colorados (LC) (Knipping et al. 2015) and Tarom (Ta) (Mokhtari et al., 2017).

Mean minor and trace element composition normalized to bulk continental crust to show enrichment and depletion for these elements is presented in figure 8.43. Boxplots illustrating the composition of the most important trace elements are shown in figure 8.44 and figure 8.45. IOA's are generally high in REE. The samples from Kiirunvaara are slightly enriched in REE (figure 8.40) and show about the same concentrations in REE as other IOA's like Los Colorados and Tarom (figure 8.42).

Table 8.1 Content of major and minor elements determined by ICP-MS. SiO_2 content was calculated[1].

Sample	Location	Al_2O_3 [%]	CaO [%]	Fe_2O_3 [%]	K_2O [%]	MgO [%]	MnO [%]	Na_2O [%]	P_2O_5 [%]	TiO_2 [%]	SiO_2 [%]
KUJ1	HW	7.77	1.15	56.91	0.81	1.59	0.05	3.8	0.16	0.43	27.17
KUJ2	HW	3.67	2.57	68.07	0.23	2.17	0.09	1.74	0.11	1.0	20.17
KUJ3	FW	2.29	2.62	64.35	0.39	2.69	0.07	0.94	0.02	1.07	25.40
KUJ4	FW	12.94	2.16	24.45	1.47	2.45	0.04	5.96	0.05	1.2	49.11
KUJ5	OZ	0.42	2.06	86.94	0.23	2.52	0.13	0.04	0.02	1.07	6.34
KUJ6	FW	13.47	9.25	5.93	3.3	2.26	0.06	5.76	0.5	1.42	57.87
KUJ7	OZ	1.06	0.59	87.09	0.83	1.53	0.07	0.03	0.02	0.43	8.17
KUJ8	HW	3.80	0.90	63.21	1.30	2.92	0.05	1.16	0.05	0.5	25.95
KUJ9	OZ	0.28	0.36	89.38	0.23	1.14	0.06	0.01	0.05	0.07	8.23
KUJ10	OZ	1.34	0.43	92.24	1.01	1.94	0.06	0.04	0.07	0.18	2.54
KUJ11	HW	5.18	1.79	55.48	1.39	2.22	0.05	1.7	0.09	0.82	31.14
KUJ12	OZ	0.89	1.85	89.95	0.63	2.82	0.13	0.09	0.05	1.08	2.30
KUJ13	FW	9.94	2.09	33.32	1.1	2.21	0.05	4.53	0.07	1.02	45.52
KUJ14	HW	12.83	3.41	8.61	2.7	5.92	0.04	5.24	0.07	0.12	60.88
KUJ15	OZ	0.28	0.45	97.49	0.19	0.8	0.05	0.07	0.09	0.02	0.41
KUJ16	OZ	0.34	2.55	84.08	0.19	2.04	0.09	0.07	0.37	0.67	9.40
KUJ17	OZ	0.30	6.56	80.94	0.25	0.61	0.07	0.04	4.24	0.05	6.68
KUJ18	FW	8.2	1.61	46.62	0.65	0.27	0.03	4.11	0.5	0.52	37.33
KUJ19	FW	0.23	1.71	76.79	0.11	0.65	0.07	0.04	0.71	0.13	19.38
KUJ20	OZ	0.21	0.56	94.52	0.19	0.71	0.06	0.01	0.07	0.03	3.47
KUJ21	OZ	0.43	0.45	94.24	0.31	0.71	0.1	0.07	0.02	0.28	3.14
KUJ22	FW	8.77	2.09	40.33	1.94	1.56	0.05	3.65	0.07	1	40.40
PG23	HW	0.45	0.76	15.59	0.01	0.02	0.01	0.01	0.14	0.03	80.13
PG24	OZ	1.70	14.41	25.03	0.65	0.41	0.08	0.04	7.65	0.15	49.58
PG25	OZ	18.84	15.81	15.44	2.43	1.72	0.09	1.23	8.46	0.32	35.36
PG26	OZ	1.55	41.98	19.31	0.65	0.76	0.03	0.09	18.88	0.25	16.03
PG27	OZ	0.32	5.93	33.75	0.12	0.05	0.07	0.01	3.37	0.1	56.11
PG28	OZ	0.91	18.61	43.04	0.37	0.08	0.03	0.03	11.8	0.07	24.74
PG29	FW	10.7	5.6	6.85	4.93	2.84	0.09	0.38	0.92	0.2	67.22
PG30	OZ	2.40	4.73	28.46	0.31	0.55	0.1	0.92	1.67	0.07	60.55
PG31	OZ	2.04	1.04	51.48	0.84	1.36	0.03	0.26	0.53	0.05	42.16
PG32	OZ	0.66	2.66	86.09	0.34	0.45	0.03	0.03	1.72	0.07	7.67
PG33	OZ	1.76	20.57	22.17	0.6	0.27	0.03	0.07	13.43	0.15	40.63
PG34	OZ	7.33	9.66	12.16	3.59	0.51	0.07	0.2	5.09	0.18	60.87

1 100% - major elements - minor elements - trace elements [wt%]

Per Geijer samples are strongly enriched in those elements and have significantly higher concentrations in REE than Kiirunavaara, Los Colorados and Tarom except for Sc. Other than REE, PG is enriched in several critical elements (USGS, 2018) including As, Ba, Co, V, and W (figure 8.43). Generally, the minor and trace element signature does not differ strongly between Kiirunavaara and Per Geijer. Most elements that are enriched in Kiirunavaara are as well enriched in Per Geijer (figure 8.40). However, there are some differences. Both deposits are high in V, but especially Kiirunavaara samples are strongly enriched in V. The ore zone has a higher V content than the host rock

zone in both deposits with values ranging from 589 ppm to 1343 ppm and from 2.37 ppm to 954 ppm for KUJ and PG, respectively (figure 8.45B). Nickel and W contents are also high in both deposits, slightly higher in KUJ (figure 8.44F), but with a wider span between min and max in PG. Nickel values range from 41.1 ppm to 243 ppm in KUJ and from 2.9 to 313.3 ppm in PG. Cobalt is also relatively high in both deposits (figure 8.44B), Co content ranges from 33 ppm to 133.8 ppm in KUJ and from 19 ppm to 80.7 ppm in PG. Arsenic content, in contrast, is low in KUJ and high in PG (figure 8.44A). Gallium, Cr, Mo, Nb and Ta concentrations are low in both deposits and do not show large differences. Chromium values range from 5 ppm to 39 ppm in KUJ and from 4 ppm to 10 ppm in PG. Zinc content is low in both deposits but significantly higher in KUJ (figure 8.45F). A difference in trace element signature with depth could not be observed. A tendency of higher trace element concentrations that are compatible with magnetite (e.g., V, Ni, Co) in KUJ compared to PG was determined (figure 8.44; figure 8.45).

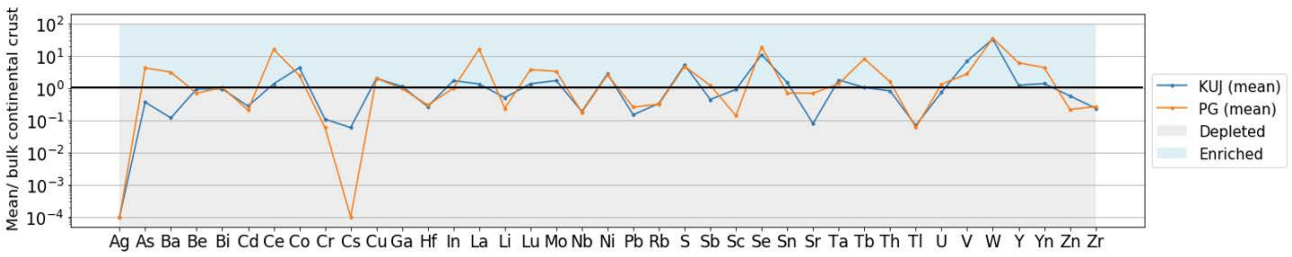

Figure 8.43 Average minor and trace elements contents measured by ICP-MS normalized to continental crust. The composition of the continental crust was taken from Rudnick (2003). The plot shows which elements are enriched and which are depleted. Apart from As, Ba and U, KUJ and PG samples are enriched or depleted in the same elements.

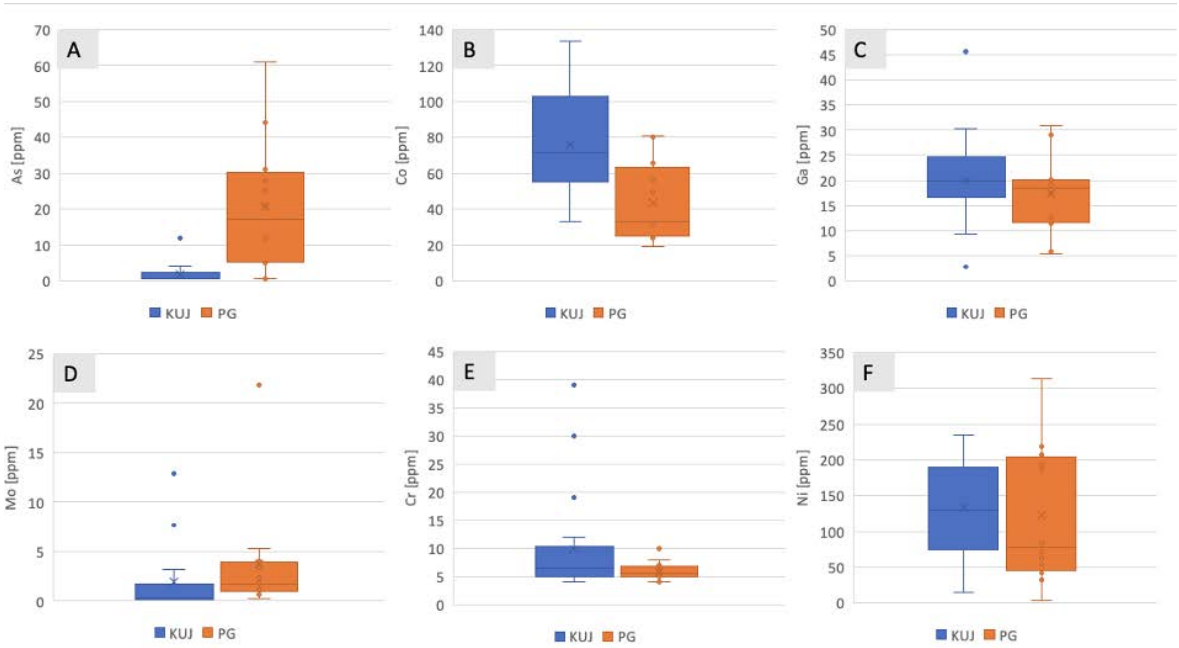

Figure 8.44 Arsenic (A), cobalt (B), gallium (C), molybdenum (D), chromium (E) and nickel (F) content of all samples from KUJ and PG measured by ICP-MS in bulk rock. As content is low in KUJ but significantly higher in PG. Co content is high in both samples but slightly higher in in KUJ. Ga, Mo, Cr and Ni do not show major differences. Mo, Cr and Ga contents are both low, whereas both Ni contents are relatively high.

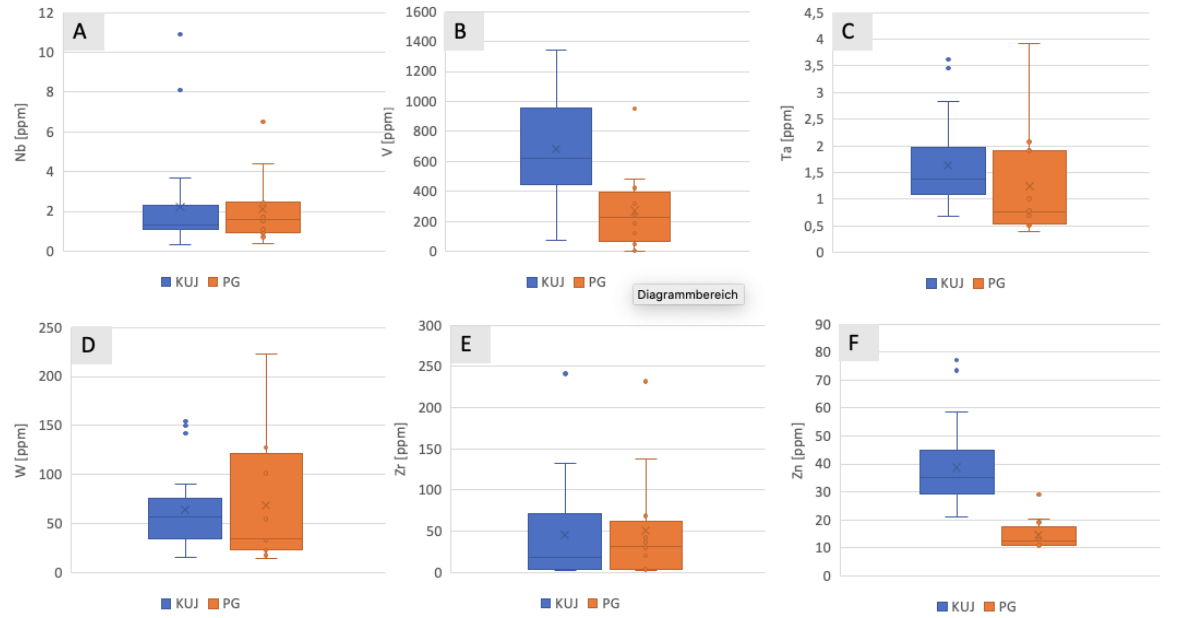

Figure 8.45 Niobium (A), vanadium (B), tantalium (C), tungsten (D), zircon (E) and tin (F) content of of all samples from KUJ and PG measured by ICP-MS in bulk rock. V content is high in both samples, but higher in KUJ. Zn in relatively high in KUJ and low in PG. Nb, Ta, W and Zr contents do not differ greatly. Nb and Ta contents are both low, W and Zr contents are both high. Note that the samples have been milled with a tungsten swing mill, which might cause W contamination.

Table 8.2 Element composition determined by ICP-MS (Ag-In).

	Location	Ag	Al	As	Ba	Be	Bi	Ca	Cd	Ce	Co	Cr	Cs	Cu	Fe	Ga	Hf	In
Unit		PPM	%	PPM	PPM	PPM	PPM	%	PPM	PPM	PPM	PPM	PPM	PPM	%	PPM	PPM	PPM
D.Limit		0.05	0.01	1	5	0.1	0.02	0.01	0.01	0.05	0.1	1	0.05	0.5	0.01	0.1	0.02	0.02
Upper Limit		10	15	10000	10000	100	10000	15	10000	5000	10000	10000	1000	10000	100	10000	500	500
KUJ1	HW	0.07	4.11	<1	47	4.3	0.37	0.82	0.01	55.6	56	30	0.31	28.2	39.8	19.1	2.39	0.1
KUJ2	HW	<0.05	1.94	3	103	4.5	0.34	1.84	0.01	66.3	58.7	5	0.07	81.3	47.6	18.5	0.9	0.19
KUJ3	FW	0.07	1.21	<1	25	2.9	0.21	1.87	<0.01	53.7	55.1	11	0.25	17.4	45	20.5	0.8	0.16
KUJ4	FW	<0.05	6.85	<1	87	3.2	0.13	1.54	0.06	135.5	33	12	0.4	21.4	17.1	26.1	3.08	0.06
KUJ5	OZ	<0.05	0.22	<1	21	1.4	0.13	1.47	<0.01	13.7	118.5	9	0.1	21.4	60.8	30.3	0.47	0.11
KUJ6	FW	0.32	7.13	<1	221	3.8	0.14	6.61	0.17	200	34.3	6	<0.05	120	4.15	21.3	6.37	0.13
KUJ7	OZ	<0.05	0.56	1	64	0.7	0.18	0.42	<0.01	14.8	74.1	10	0.47	23.6	60.9	17.4	0.61	0.09
KUJ8	HW	<0.05	2.01	3	182	2.1	0.19	0.64	<0.01	22.1	68.8	5	0.84	273.4	44.2	18.3	1.11	0.1
KUJ9	OZ	<0.05	0.15	2	44	0.9	0.12	0.26	<0.01	7.79	76.1	5	0.1	79.2	62.5	20.5	0.31	0.05
KUJ10	OZ	<0.05	0.71	<1	61	1	0.09	0.31	<0.01	9.9	80.5	6	0.41	25	64.5	20.8	0.81	0.06
KUJ11	HW	0.18	2.74	2	134	3.1	0.11	1.28	<0.01	109.3	55.3	4	0.59	21	38.8	19.5	2.13	0.12
KUJ12	FW/OZ	0.24	0.47	<1	31	1.2	0.08	1.32	<0.01	31.5	110.5	9	0.3	34.7	62.9	45.6	0.54	0.11
KUJ13	FW	0.08	5.26	<1	66	3	0.11	1.49	0.08	148.2	45	7	0.51	69.1	23.3	27.5	3.48	0.11
KUJ14	HW/OZ	0.07	6.79	4	127	4.6	0.17	2.44	0.05	251	67.7	6	1.33	77.9	6.02	27.3	3.99	0.23
KUJ15	OZ	<0.05	0.15	2	23	0.3	0.11	0.32	<0.01	10.5	86.9	4	0.09	22.8	68.8	11.8	0.27	0.04
KUJ16	OZ	0.32	0.18	3	29	1.3	0.09	1.82	<0.01	39.4	103.2	8	0.08	19.7	58.8	19.6	0.22	0.08
KUJ17	OZ	0.07	0.16	12	63	0.6	0.27	4.69	<0.01	543.1	113.2	4	0.12	103.1	56.6	9.4	0.15	0.04
KUJ18	FW	<0.05	4.34	<1	76	1	0.1	1.15	<0.01	51.6	60.4	39	0.07	21.3	32.6	2.8	0.66	0.03
KUJ19	FW	0.48	0.12	<1	24	0.3	0.07	1.22	<0.01	62.7	102.3	19	<0.05	31.2	53.7	2.9	0.16	0.07
KUJ20	OZ	<0.05	0.11	<1	17	0.3	0.1	0.4	<0.01	10.3	91	4	0.12	13.9	66.1	24.2	0.1	0.05
KUJ21	OZ	0.62	0.23	<1	40	0.3	0.14	0.32	<0.01	10.1	133.8	6	0.13	59	65.9	14.3	0.23	0.06
KUJ22	FW	<0.05	4.64	1	187	3.2	0.14	1.49	0.1	52.7	42.2	8	0.09	87.2	28.2	20.3	2.32	0.14
PG23	HW/OZ	0.15	0.24	12	>10000	0.05	0.17	0.54	<0.01	3892	24	5	<0.05	21.7	10.9	29	0.18	<0.02
PG24	OZ	<0.05	0.9	31	211	0.9	0.2	10.3	<0.01	993.6	19	7	0.1	45.2	17.5	19.1	0.22	0.07
PG25	OZ	0.14	9.97	28	506	3.2	0.14	11.3	<0.01	871.6	49.6	4	0.45	80.7	10.8	17.5	1.86	0.13
PG26	OZ	<0.05	0.82	44	105	2.3	0.19	>15	<0.01	2197	24.7	10	0.12	28.8	13.5	31	1.13	0.06
PG27	OZ	<0.05	0.17	6	64	0.3	0.12	4.24	<0.01	395.4	33.6	6	<0.05	26.2	23.6	11.4	0.12	<0.02
PG28	OZ	0.1	0.48	25	149	0.8	0.07	13.3	<0.01	1006	80.7	5	<0.05	17.5	30.1	20.2	0.31	0.02
PG29	FW	<0.05	5.66	<1	1313	5.6	0.11	4	0.1	174	65.6	4	0.67	106.1	4.79	12.6	6.87	0.2
PG30	OZ	0.35	1.27	13	142	0.7	0.29	3.38	0.001	372.2	33.1	5	0.07	135.1	19.9	5.9	0.97	0.02
PG31	OZ	0.47	1.08	<1	72	0.6	0.11	0.74	0.03	81.5	56.4	8	1.01	58.8	36	5.3	0.98	0.03
PG32	OZ	0.13	0.35	5	47	0.7	0.25	1.9	<0.01	221.6	79.9	6	0.1	88	60.2	17.9	0.67	0.03
PG33	OZ	1.71	0.93	61	184	0.9	0.25	14.7	<0.01	1315	25.8	6	0.21	49	15.5	19.1	1.54	0.03
PG34	OZ	0.19	3.88	21	1283	1.5	0.15	6.9	0.06	705.4	31.9	5	0.56	26.7	8.5	19.9	4.4	0.06

Table 8.3 Element composition of all samples determiend by ICP-MS (K-Se).

	Location	K	La	Li	Lu	Mg	Mn	Mo	Na	Nb	Ni	P	Pb	Rb	S	Sb	Sc	Se
		%	PPM	PPM	PPM	%	PPM	PPM	%	PPM	PPM	%	PPM	PPM	%	PPM	PPM	PPM
D.Limit		0.01	0.1	1	0.01	0.01	5	0.05	0.01	0.1	0.5	0.01	2	0.2	0.5	0.05	0.5	2
Upper Limit		15	5000	10000	1000	15	10000	1000	15	1000	10000	15	10000	10000	50	10000	10000	1000
KUJ1	HW	0.67	19.6	12	0.57	0.96	400	7.76	2.82	1.8	77.4	0.07	2.4	27.8	<0.5	0.69	9.5	<2
KUJ2	HW	0.19	26	5	0.84	1.31	695	1.58	1.29	1.4	91.3	0.05	<2	6.4	<0.5	1.4	12.8	<2
KUJ3	FW	0.32	21.3	17	0.52	1.62	525	0.3	0.7	1.3	121	0.01	3.5	19.5	<0.5	0.19	37.8	<2
KUJ4	FW	1.22	55	31	0.62	1.48	334	12.9	4.42	8.1	46.1	0.02	<2	35.7	0.5	<0.05	34.5	<2
KUJ5	OZ	0.19	4.3	3	0.24	1.52	1042	0.26	0.03	2.7	234.3	0.01	<2	10	<0.5	0.12	18.2	<2
KUJ6	FW	2.74	91.3	5	0.83	1.36	465	0.81	4.27	10.9	14.5	0.22	3.4	41	<0.5	0.09	10	<2
KUJ7	OZ	0.69	10.4	17	0.12	0.92	528	3.22	0.02	1.3	170.7	0.01	2.6	33.9	<0.5	0.33	10.6	<2
KUJ8	HW	1.08	10.1	24	0.23	1.76	416	0.49	0.86	1.3	100.8	0.02	2.2	51	<0.5	0.48	17.3	<2
KUJ9	OZ	0.19	4.8	8	0.12	0.69	456	0.25	0.01	0.7	177.8	0.02	<2	10.8	<0.5	<0.05	10.2	<2
KUJ10	OZ	0.84	4.8	22	0.08	1.17	453	0.19	0.03	1.1	139.9	0.03	5.6	38.7	<0.5	<0.05	11	<2
KUJ11	HW	1.15	48.2	15	1.06	1.34	414	1.07	1.26	3.7	52.3	0.04	2.3	42.6	<0.5	<0.05	8.4	<2
KUJ12	FW/OZ	0.52	14.2	8	0.35	1.7	1029	0.12	0.07	1.9	209.2	0.02	<2	28.9	<0.5	<0.05	20.6	<2
KUJ13	FW	0.91	62.7	24	0.63	1.33	396	7.67	3.36	1.2	80.9	0.03	2.5	52.8	0.7	<0.05	13.9	<2
KUJ14	HW/OZ	2.24	236.3	30	0.27	3.57	315	0.95	3.89	0.8	58.4	0.03	<2	123.1	1.3	<0.05	32	<2
KUJ15	OZ	0.16	7	10	0.03	0.48	389	0.27	0.05	0.6	183.6	0.04	<2	9.1	<0.5	<0.05	7.7	<2
KUJ16	OZ	0.16	13.4	3	0.48	1.23	664	0.17	0.05	1.3	191.2	0.16	8.3	6.2	<0.5	<0.05	2.4	<2
KUJ17	OZ	0.21	211.5	4	1.41	0.37	538	0.16	0.03	1.2	189.6	1.85	3.7	10.2	<0.5	<0.05	<0.5	<2
KUJ18	FW	0.54	27	4	0.22	0.16	264	1.09	3.05	1.8	102.3	0.22	<2	11	<0.5	<0.05	<0.5	<2
KUJ19	FW	0.09	28.4	3	0.26	0.39	518	0.17	0.03	1	208.8	0.31	<2	4.5	<0.5	<0.05	<0.5	<2
KUJ20	OZ	0.16	7.5	12	0.06	0.43	433	0.1	0.01	0.3	178.1	0.03	<2	9.2	<0.5	<0.05	11.8	<2
KUJ21	OZ	0.26	4	5	0.08	0.43	788	0.33	0.05	2.4	222.4	0.01	5.6	16.4	<0.5	0.34	2.1	<2
KUJ22	FW	1.61	21.6	7	0.4	0.94	422	2.2	2.71	2.3	65.3	0.03	2.4	32.2	<0.5	<0.05	10.9	<2
PG23	HW/OZ	<0.01	2496	<1	0.23	0.01	43	3.44	<0.01	0.9	2.9	0.06	2.2	0.5	0.6	<0.05	<0.5	<2
PG24	OZ	0.54	404.1	2	1.57	0.25	623	5.26	0.03	1.6	72.1	3.34	3.3	14	<0.5	0.12	1.7	2.6
PG25	OZ	2.02	381.8	11	1.52	1.04	711	1.21	0.91	0.7	41.8	3.69	2.3	46.4	<0.5	<0.05	1.5	3
PG26	OZ	0.54	955.4	7	4.23	0.46	229	0.63	0.07	0.4	62.6	8.24	6.2	12	<0.5	<0.05	<0.5	3.6
PG27	OZ	0.1	161.6	<1	0.47	0.03	568	1.57	<0.01	1.1	207.5	1.47	4.6	2.2	<0.5	<0.05	<0.5	<2
PG28	OZ	0.31	395.3	2	1.65	0.05	260	1.21	0.02	1.7	313.3	5.15	2.6	6.4	<0.5	<0.05	2.9	3.6
PG29	FW	4.09	86.4	26	0.59	1.71	729	0.97	0.28	4.4	32.8	0.4	2.5	97	<0.5	<0.05	9.5	<2
PG30	OZ	0.26	219.1	2	0.41	0.33	745	21.8	0.68	6.5	187	0.73	6.4	7.4	<0.5	1.42	1.2	<2
PG31	OZ	0.7	48.5	7	0.12	0.82	229	4.08	0.19	2.5	218.3	0.23	2	29.1	<0.5	0.82	-0.5	<2
PG32	OZ	0.28	98.5	4	0.33	0.27	198	0.2	0.02	1.5	194.1	0.75	6.4	7.4	<0.5	0.55	6.7	<2
PG33	OZ	0.5	592.8	2	1.88	0.16	228	2.39	0.05	1.6	82.7	5.86	4.1	18.2	<0.5	1.57	-0.5	<2
PG34	OZ	2.98	306.7	5	1.09	0.31	531	1.82	0.15	2.4	53.5	2.22	10.6	81.9	<0.5	1.3	0.6	<2

Table 8.4 Trace element composition determined by ICP-MS (Sn-Zr).

	Location	Sn	Sr	Ta	Tb	Te	Th	Ti	Tl	U	V	W	Y	Yb	Zn	Zr
		PPM	PPM	PPM	PPM	PPM	PPM	%	PPM	PPM	PPM	PPM	PPM	PPM	PPM	PPM
D.Limit		3	0.5	0.05	0.05	0.05	0.2	0.02	0.02	0.1	1	0.1	0.5	0.1	0.5	0.5
Upper Limit		1000	10000	10000	10000	500	10000	15	10000	10000	10000	10000	10000	1000	10000	10000
KUJ1	HW	6.1	34.6	1.88	0.63	0.2	2.9	0.26	0.08	2.4	497	60.2	25.9	3.3	44.7	49.3
KUJ2	HW	5.6	24.7	0.92	0.89	0.12	1.3	0.6	0.06	2	589	24.6	34.9	4.8	58.7	18.3
KUJ3	FW	3.6	12.3	1.55	0.65	0.06	2.8	0.64	0.04	1.2	655	68.8	24.3	3	27.1	25.4
KUJ4	FW	4.5	54.9	1.21	0.87	<0.05	4.9	0.72	0.08	2.5	254	36.3	33.7	3.9	24.6	109.1
KUJ5	OZ	3.8	2.5	0.85	0.33	<0.05	4.9	0.64	0.02	0.5	1273	15.5	12.6	1.4	77.2	9.3
KUJ6	FW	3.6	58.5	3.62	1.43	0.05	6.7	0.85	0.06	4	76	150	48.6	5.1	29.5	240.9
KUJ7	OZ	<3	10.1	0.68	0.12	<0.05	1.5	0.26	0.06	0.5	984	15.3	4.7	0.7	46.3	13.3
KUJ8	HW	<3	15.5	1.93	0.26	0.06	1.1	0.3	0.12	1.3	594	75.2	10.6	1.4	35.9	36.4
KUJ9	OZ	<3	4.2	1.54	0.12	<0.05	1	0.04	0.03	2.8	669	44.2	4.8	0.7	32.7	3
KUJ10	OZ	<3	8.8	2.08	0.14	<0.05	81.2	0.11	0.09	4.7	693	69.6	5.1	0.5	39.4	24.6
KUJ11	HW	5.8	37.6	1.92	1.74	<0.05	4	0.49	0.11	3.2	455	78.8	61.9	7.3	31.1	66.5
KUJ12	FW/OZ	6.8	5.2	1.26	0.57	<0.05	2.8	0.65	0.06	0.6	1226	34.5	20.3	2.3	32.5	15.6
KUJ13	FW	4.8	61.5	1.25	0.97	<0.05	4.6	0.61	0.1	4.7	424	54.9	34.8	3.9	29.6	128.9
KUJ14	HW/OZ	<3	83.3	2.83	0.25	<0.05	5	0.07	0.26	4.9	87	154.3	5.3	1	27.4	132.5
KUJ15	OZ	<3	7.4	2.39	<0.05	<0.05	2.9	0.01	0.03	0.2	771	90.9	1.7	0.2	35.3	4.3
KUJ16	OZ	3.5	5.4	0.69	0.99	<0.05	46.3	0.4	0.03	1.6	1119	21.1	33.7	3.3	38.7	5.6
KUJ17	OZ	<3	35.1	1	4.51	<0.05	7.5	0.03	0.04	0.5	589	35.3	141.6	10.6	44.9	2
KUJ18	FW	3.2	38	1.39	0.47	<0.05	1	0.31	0.03	1.1	594	74	17	1.6	21.2	17.7
KUJ19	FW	<3	13.2	1.35	0.73	<0.05	1.1	0.08	<0.02	0.2	775	65.6	25.7	1.9	37.1	3
KUJ20	OZ	<3	15	1.11	<0.05	<0.05	1.2	0.02	0.03	3.5	949	50.8	1.7	0.3	35.2	3.8
KUJ21	OZ	3.3	8.6	3.46	0.15	<0.05	5.1	0.17	0.03	0.5	1343	142.4	5.1	0.5	73.5	3.1
KUJ22	FW	<3	24.9	1.2	0.58	<0.05	2.4	0.6	0.06	1.5	400	52.4	21.4	2.5	28.1	86.4
PG23	HW/OZ	<3	1692	2.08	6.36	<0.05	1.4	0.02	<0.02	2.2	6	131.3	43	1.7	13	3.5
PG24	OZ	<3	95.7	0.69	7.95	<0.05	8.6	0.09	0.05	4	425	32.9	182.8	11.8	10.7	3.6
PG25	OZ	<3	95.8	1.01	6.97	<0.05	12.8	0.19	0.08	1.7	188	55	166.2	11.4	10.9	69
PG26	OZ	<3	206	0.53	16.7	<0.05	29.2	0.15	0.03	2.2	2.37	23.2	448.1	31.1	12	30.1
PG27	OZ	<3	37.5	1.91	2.81	<0.05	9.6	0.06	<0.02	2.5	263	101.3	57.3	3.6	12	2.7
PG28	OZ	<3	140.2	0.73	8.92	<0.05	10.6	0.04	<0.02	3.4	319	33.9	215.2	13.5	13.1	5.3
PG29	FW	<3	27.2	3.92	1.17	<0.05	7.6	0.12	0.16	2.6	49	223.3	27.7	3.2	20.1	231.8
PG30	OZ	<3	40.6	0.51	1.6	<0.05	18.3	0.04	0.05	8.2	245	17.8	35.5	2.6	13	31.9
PG31	OZ	<3	12.5	0.78	0.48	<0.05	1.9	0.03	0.09	5	480	35.2	11.5	0.7	19	37.1
PG32	OZ	<3	16.2	0.4	1.54	<0.05	56.4	0.04	0.04	3.4	954	15	37	2.6	29	20.1
PG33	OZ	<3	196.5	0.54	9.96	<0.05	17.3	0.09	0.06	3.8	208	25.1	233.9	13.8	11	42.2
PG34	OZ	<3	108.9	1.92	4.95	<0.05	26.1	0.11	0.11	4.4	123	127.9	110.1	8.1	11	137.7

8.3.2 Results determined by EMPA

Major, minor and trace element composition of apatite and magnetite grains was measured by EMPA. A total of 52 points in 18 apatite crystals from Kiirunavaara, 45 points in 20 apatite crystals from Per Geijer, such as 42 points in 20 magnetite crystals from Kiirunavaara and 20 points in 11 magnetite crystals from Per Geijer were measured. The crystals were analyzed from core to rim in order to assess any possible chemical zonation.

8.3.2.1 Apatite Composition

The complete apatite composition determined by EMPA is listed in the appendix. A summary providing mean, min and max values for core and rim position of every measured sample is presented in table 8.5. Calcium composition in apatites from Per Geijer and Kiirunavaara is heterogeneous but quite similar with values ranging from 53.9 wt% to 56.9 wt% (figure 8.46E). P_2O_5 content is slightly higher in PG (figure 8.46D) with mean values of 41.5 wt% and 41.9 wt%, respectively. All apatite crystals from Per Geijer and Kiirunavaara are without any exception fluorapatites (F apatites) (figure 8.48) with F values ranging from 3.288 wt% to 4.496 wt% in Kiirunavaara and from 3.288 wt% to 4.633 wt% in Per Geijer. Chlorine is generally low with values ranging from 0.0036 wt% to 0.1620 wt% in Kiirunavaara and from 0.0036 wt% to 0.1870 wt% in Per Geijer. Chlorine concentrations in apatite are slightly higher in PG with a mean value of 0.0807 wt% compared to a mean of 0.0553 wt% in KUJ. The PG apatites show however a larger range between Cl minimum and maximum resulting in a lower median value (figure 8.47A). A minor difference in halogen concentration is also recognizable between host rock and ore zone apatite and within each apatite grain. In Kiirunavaara the lowest Cl and highest F values occur in the host rock zone, where apatite is associated with disseminated ore (KUJ4-100, KUJ-13-123 (figure 8.48). The highest Cl values and lower F values are found in ore zone sample KUJ17-221. Cl values tend to increase with decreasing F values. A weak chemical zonation was observed in sample KUJ1-100 (HR), KUJ17-221 (OZ) and KUJ19-221 (HR). The apatite crystals have increasing Cl values

and decreasing F values from core to rim up to a 0.5% difference in F and to 0.051 wt% in Cl. OH values were calculated using the method after Piccoli & Candela (2002). The halogen distribution of Per Geijer and Kiirunavaara apatites is shown in the ternary diagram in figure 8.49. The Z-site of Kiirunvaara apatites is mainly occupied by F. The majority of the apatites have a >97% F composition. A few outliers show OH values of 5 wt% to 12 wt%, they occur in ore zone sample KUJ17-221, such as HR sample KUJ19-221.

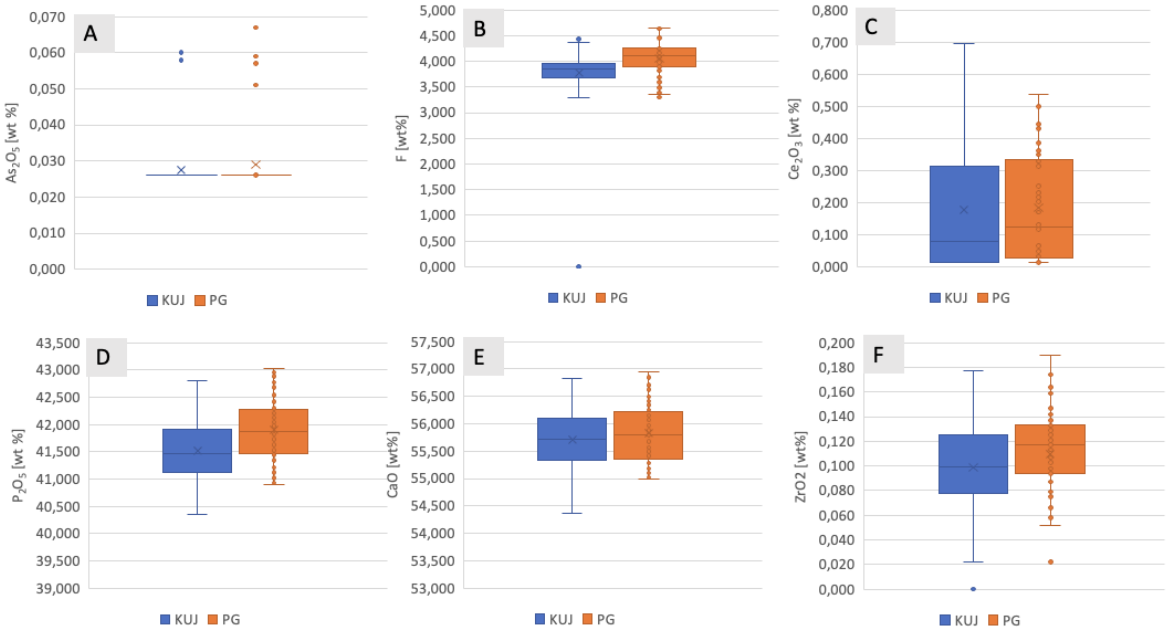

Figure 8.46 As_2O_5 (A), F (B), Ce_2O_3 (C), P_2O_5 (D), CaO (E) and ZrO_2 (F) composition of apatites from Kiirunavaara and Per Geijer. As_2O_5 measurements were mainly below detection limit. F values are slightly higher in PG but do not differ greatly. A similar statement can be made for Ce_2O_3, P_2O_5, CaO and ZrO_2.

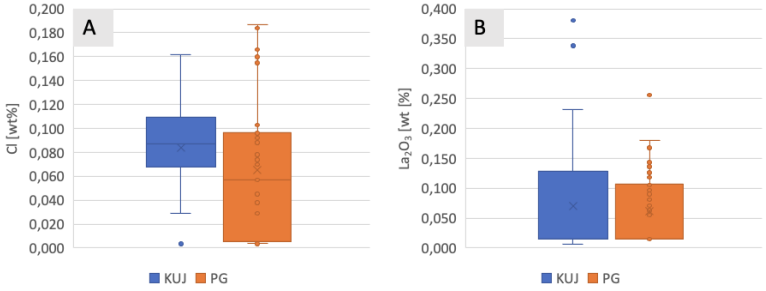

Figure 8.47 Cl (A) and La_2O_3 (B) composition of apatites from Kiirunavaara and Per Geijer. Cl content is higher in PG but more widely distributed. Cl distribution in KUJ is less distributed. Median is therefore higher in KUJ, whereas the mean in higher in PG. La_2O_3 composition in KUJ and PG is about similar.

In Per Geijer the highest Cl concentrations and the lowest F concentrations occur in PG31-617. Low Cl values and a wide range of F values are found in PG28-165 and PG33-163. In Per Geijer Cl values tend to increase with depth. The majority of the crystals show as well as the Kiirunavaara apatites a trend of decreasing F values and increasing Cl values from core to rim. The halogen site of PG apatites is similarly occupied as in KUJ (figure 8.49) with the majority of apatite showing a >97% F composition. The highest OH composition is found in PG31-617 from the deep part of Henry.

Trace element signature in apatites from Kiirunavaara and Per Geijer does not vary significantly. Per Geijer apatite shows a slightly higher concentration in all elements except for La_2O_3. Most measurements of As_2O_5 were below detection limit.

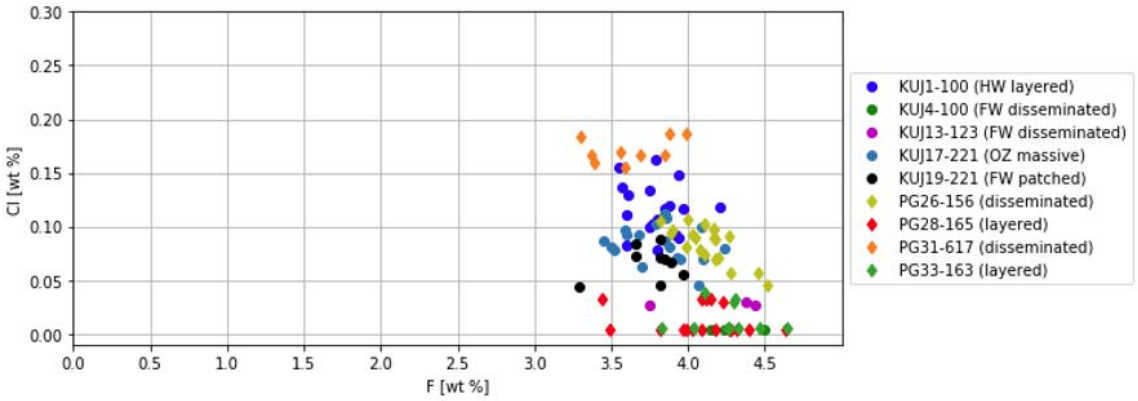

Figure 8.48 Plot of F and Cl concentrations (wt%) in apatites from KUJ and PG measured by EMPA. Apatites from PG31-617 show the highest Cl concentrations, KUJ4-100, PG28-165 and PG33-163 show the lowest Cl concentrations.

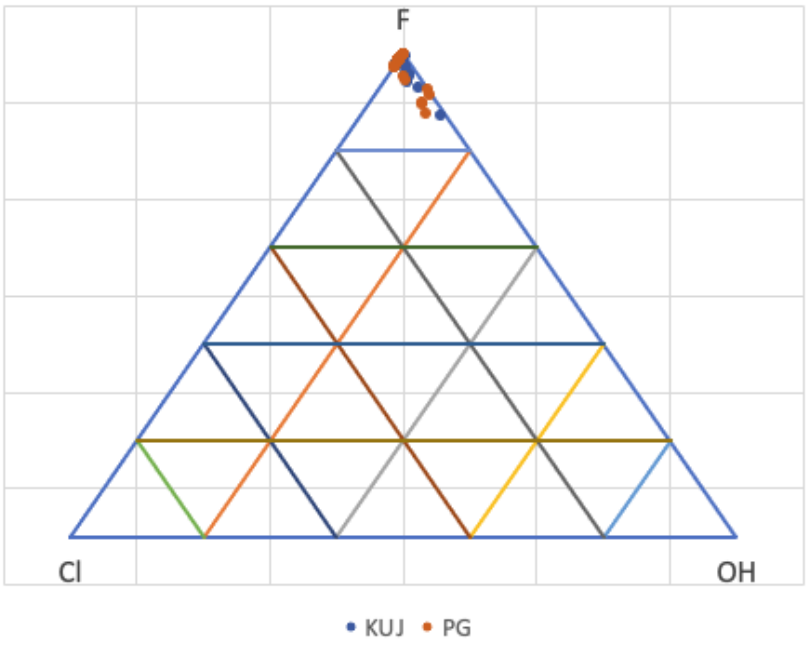

Figure 8.49 Ternary diagram the halogen content in apatite regarding the F-Cl-OH atomic proportions from KUJ and PG. OH was calculated using the method after Piccoli & Candela (2002). Apatites from Kiirunavaara and Per Geijer are all fluoarapatites with very little amounts of Cl and little amounts of OH. Note that many points overlap at 100 wt% F. A total of 97 measurements are plotted in the diagram.

8.3.2.2 Magnetite Composition

The complete magnetite composition determined by EMPA can be found in the appendix. A summary providing mean, min and max values for core and rim position of every sample is presented in table 8.6. The trace element composition of every sample is visualized with boxplots in figure 8.52 and figure 8.53. Since all measurements of SnO_2, Y_2O_3, Cr_2O_3, Nb_2O_5, NiO, MoO_3 and WO_3 were below detection limit they are not included in the chart. Magnetite crystals from Kiirunavraa are relatively high in V and Co and low in Al and Ti. Cobalt contents are about similar in every sample, V is variable with the highest content of 0.178 wt% V_2O3 in HR sample KUJ13-123 (figure 8.52). Magnesium, Si, Ca and Mn contents are as well variable (figure 8.53). Ore zone sample KUJ17-221 has the highest values for those elements, especially Mn values are comparatively high with a max value of 0.1 wt% MnO. A weak chemical zonation was observed in the Kiirunavaara samples. Core values tend to be higher in SiO_2 and lower in MgO compared to the rim (figure 8.50). However, ore zone sample KUJ17-221 shows an opposite trend. The measured magnetite grains were as well studied with a coupled SEM, but no zonation was observed.

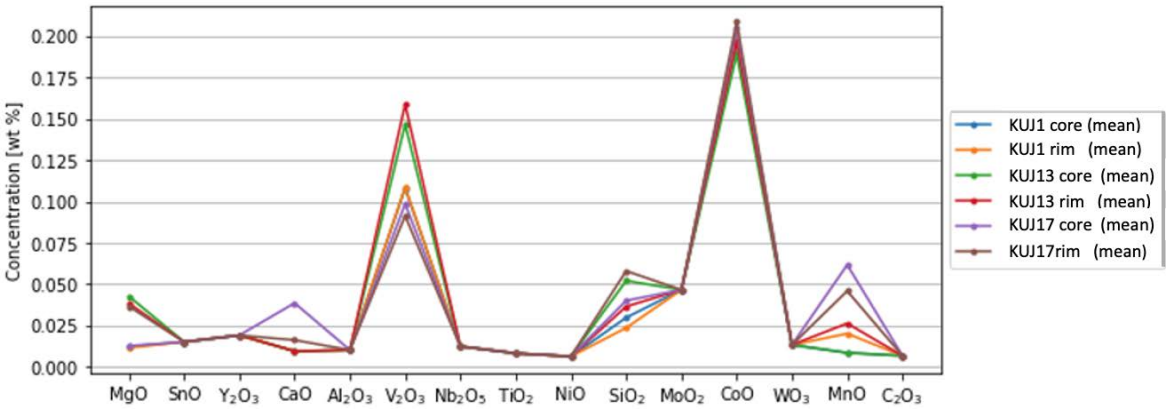

Figure 8.50 Mean of trace element composition for core and rim values of all measures KUJ samples. Core values are mainly higher in SiO_2. No zonation for other elements were observed.

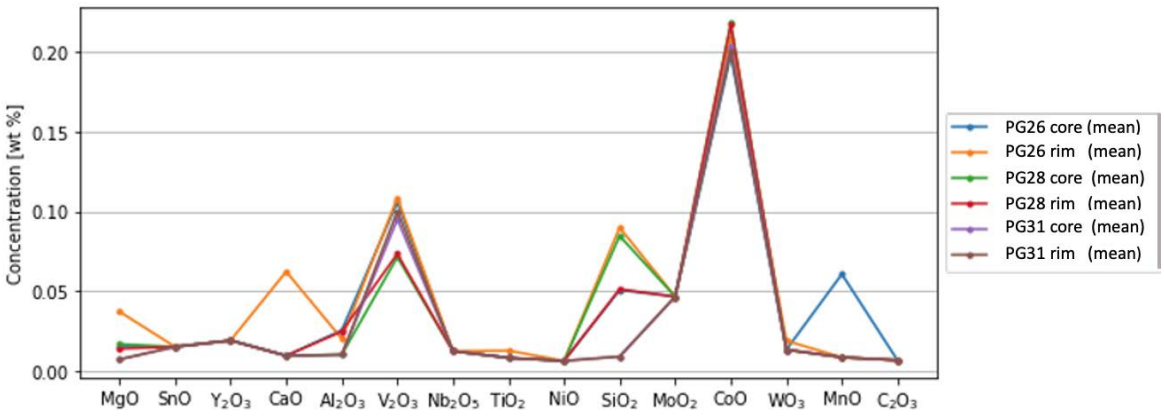

Figure 8.51 Mean of trace element composition for core and rim values of all measures PG samples. As in the KUJ samples core values are higher in SiO_2 than the rim.

Magnetite crystals from Per Geijer are also relatively high in V and Co, but slightly lower in V and slightly higher in Co than the KUJ samples. Cobalt values are about similar among the PG samples, V contents differ however greatly with values ranging from 0.068 wt% to 0.1160 wt%. Aluminium and Mn contents are very low. Silicon is extremely variable with values ranging from 0.0089 wt% to 0.268 wt%. The PG samples are generally higher in Si than KUJ samples (figure 8.53). Sample PG26-156 can be considered as an outlier since its the only sample showing >detection limit values for Ti, Ca and Al. As well as in Kiirunavaara the samples show decreasing Si values from core to rim, except for ore zone sample PG26-156 that has higher rim values for most elements (figure 8.51). All in all the trace element composition between Kiirunavaara and Per Geijer does not differ significantly.

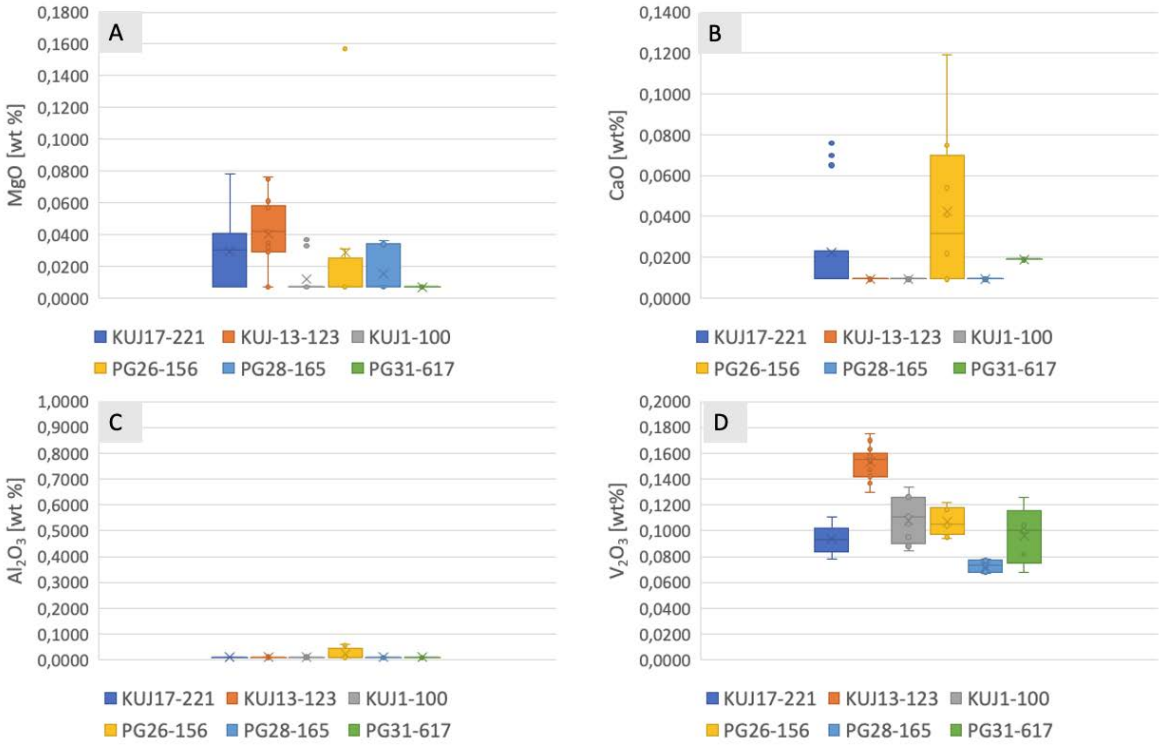

Figure 8.52 MgO (A), CaO (B), Al_2O_3 (C) and V_2O_3 (D) content of all Mt grains. MgO and V_2O_3 contents are variable and slightly higher in Kiirunavaara. Al_2O_3 and CaO doesn't excced D.L. except for sample PG26-156 and KUJ17-221.

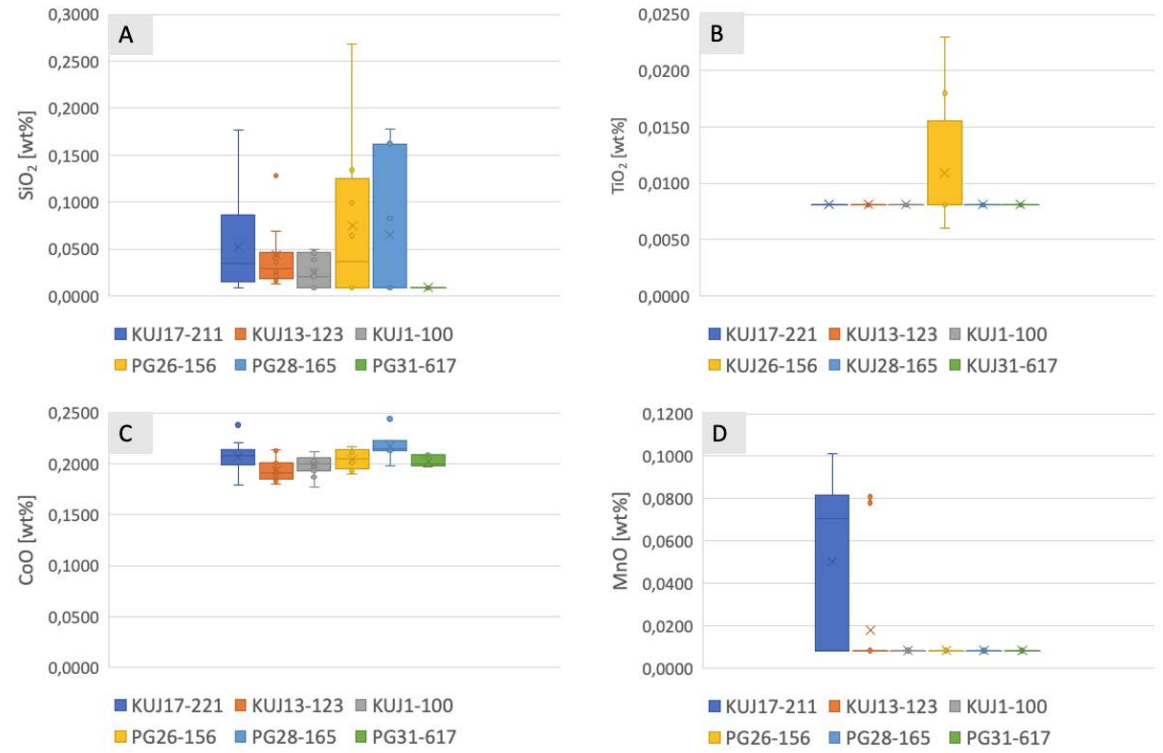

Figure 8.53 SiO_2 (A), TiO_2 (B), CoO (C) and MnO (D) composition of all measured magnetite grains within the differet samples. CoO content is high and quite constant in all samples. Except for KUJ26-156 and KUJ17-221 no sample exceeded D.L for TiO_2 and MnO.

Table 8.5 Summary of apatite composition.

KUJ		As_2O_5 [%]	F [%]	P_2O_2 [%]	CaO [%]	Ce_2O_3 [%]	ZrO_2 [%]	Cl [%]	La_2O_3 [%]
KUJ1	Mean	0.026	3.8974	41.5711	55.9009	0.1184	0.0829	0.1174	0.0446
Core	Min	0.026	3.546	40.362	55.262	0.014	0.022	0.09	0.015
	Max	0.026	4.209	42.796	56.428	0.506	0.173	0.155	0.163
KUJ1	Mean	0.026	3.7269	41.8805	55.8792	0.0681	0.0987	0.1189	0.0349
Rim	Min	0.026	3.568	41.304	54.673	0.014	0.059	0.078	0.015
	Max	0.026	3.883	42.799	56.456	0.241	0.138	0.162	0.19
KUJ13	Mean	0.058	4.372	41.617	55.902	0.014	0.118	0.029	0.015
Core	Min	0.058	4.372	41.617	55.902	0.014	0.118	0.029	0.015
	Max	0.058	4.372	41.617	55.902	0.014	0.118	0.029	0.015
KUJ13	Mean	0.026	4.0915	41.076	56.056	0.0405	0.123	0.0036	0.015
Rim	Min	0.026	3.746	41.038	56.001	0.014	0.118	0.0036	0.015
	Max	0.026	4.437	41.114	56.111	0.067	0.128	0.0036	0.015
KUJ17	Mean	0.026	4.0468	41.2158	55.4937	0.1533	0.1193	0.0795	0.0423
Core	Min	0.026	3.499	40.359	54.361	0.058	0.067	0.046	0.007
	Max	0.026	4.238	41.709	56.346	0.528	0.175	0.113	0.126
KUJ17	Mean	0.0294	3.6995	41.1569	55.452	0.1596	0.1106	0.0851	0.0512
Rim	Min	0.026	3.45	40.314	53.96	0.044	0.052	0.062	0.015
	Max	0.06	3.926	41.633	56.051	0.408	0.177	0.103	0.152
KUJ4	Mean	0.026	4.145	40.985	55.13	0.694	0.092	0.0057	0.338
Core	Min	0.026	4.145	40.985	55.13	0.694	0.092	0.0057	0.338
	Max	0.026	4.145	40.985	55.13	0.694	0.092	0.0057	0.338
KUJ4	Mean	0.026	4.3665	40.8255	55.379	0.576	0.0955	0.0057	0.3065
Rim	Min	0.026	4.237	40.536	55.316	0.509	0.095	0.0057	0.232
	Max	0.026	4.496	41.115	55.442	0.643	0.096	0.0057	0.381
KUJ19	Mean	0.026	3.825	42.0135	56.1598	0.2125	0.0785	0.064	0.0805
Core	Min	0.026	3.659	41.515	55.263	0.014	0.022	0.046	0.015
	Max	0.026	3.972	42.677	56.833	0.354	0.115	0.084	0.161
KUJ19	Mean	0.026	3.695	41.8508	55.5922	0.2734	0.1044	0.0686	0.1146
Rim	Min	0.026	3.288	41.456	55.3	0.038	0.06	0.044	0.015
	Max	0.026	3.887	42.179	55.968	0.436	0.16	0.088	0.159
PG26	Mean	0.026	3.9733	41.4671	55.5921	0.404	0.0919	0.0401	0.1946
Core	Min	0.026	3.288	40.536	55.13	0.014	0.022	0.0057	0.015
	Max	0.026	4.496	42.677	56.833	0.694	0.16	0.088	0.381
PG26	Mean	0.026	3.9739	41.4535	55.6132	0.4167	0.0918	0.0388	0.2046
Rim	Min	0.026	3.288	40.536	55.13	0.014	0.022	0.0057	0.015
	Max	0.026	4.496	42.677	56.833	0.694	0.16	0.088	0.381
PG28	Mean	0.0293	4.1431	41.9456	56.0226	0.1814	0.1053	0.0121	0.0688
Core	Min	0.026	3.442	40.932	55.286	0.014	0.051	0.0036	0.015
	Max	0.059	4.633	42.681	56.706	0.431	0.174	0.032	0.18
PG28	Mean	0.026	4.0399	42.0264	56.2806	0.0933	0.1101	0.0133	0.046
Rim	Min	0.026	3.488	41.48	55.509	0.014	0.022	0.0036	0.015
	Max	0.026	4.314	42.578	56.946	0.337	0.149	0.032	0.142
PG31	Mean	0.026	3.6606	42.3898	56.3492	0.014	0.1468	0.1718	0.015
Core	Min	0.026	3.303	41.989	56.126	0.014	0.099	0.155	0.015
	Max	0.026	3.874	42.954	56.497	0.014	0.19	0.187	0.015
PG31	Mean	0.026	3.5755	42.5075	56.032	0.0353	0.0893	0.1708	0.015
Rim	Min	0.026	3.366	42.124	55.674	0.014	0.022	0.16	0.015
	Max	0.026	3.988	42.998	56.414	0.064	0.131	0.187	0.015
PG33	Mean	0.026	3.7343	42.3385	56.2031	0.0666	0.1066	0.1197	0.0326
Core	Min	0.026	3.303	41.48	55.509	0.014	0.022	0.0036	0.015
	Max	0.026	4.314	42.998	56.946	0.337	0.19	0.187	0.142
PG	Mean	0.026	4.1867	41.223	55.8183	0.0503	0.1007	0.0057	0.015
Rim	Min	0.026	4.038	41.019	55.159	0.032	0.075	0.0057	0.015
	Max	0.026	4.269	41.441	56.203	0.072	0.133	0.0057	0.015

Table 8.6 Summary of magnetite composition.

		MgO [%]	SnO_2 [%]	Y_2O_3 [%]	CaO [%]	Fe_2O_2 [%]	Al_2O_2 [%]	V_2O_2 [%]	Nb_2O_2 [%]	TiO_2 [%]	NiO [%]	SiO_2 [%]	MoO_2 [%]	CoO [%]	Wo_2 [%]	MnO [%]	Cr_2O3 [%]
KUJ1	Mean	0.0121	0.015	0.019	0.0094	102.2213	0.0101	0.108	0.0123	0.0081	0.0062	0.0297	0.0465	0.1965	0.0132	0.0084	0.0066
Core	Min	0.0071	0.015	0.019	0.0094	101.973	0.0101	0.084	0.0123	0.0081	0.0062	0.0089	0.0465	0.177	0.0132	0.0084	0.0066
	Max	0.037	0.015	0.019	0.0094	102.59	0.0101	0.127	0.0123	0.0081	0.0062	0.05	0.0465	0.212	0.0132	0.0084	0.0066
KUJ1	Mean	0.0114	0.015	0.019	0.0094	102.4845	0.0101	0.1085	0.0123	0.0081	0.0062	0.0235	0.0465	0.202	0.0132	0.02	0.0066
Rim	Min	0.0071	0.015	0.019	0.0094	102.059	0.0101	0.09	0.0123	0.0081	0.0062	0.0089	0.0465	0.193	0.0132	0.0084	0.0066
	Max	0.033	0.015	0.019	0.0094	102.799	0.0101	0.134	0.0123	0.0081	0.0062	0.047	0.0465	0.207	0.0132	0.078	0.0066
KUJ13	Mean	0.0426	0.015	0.019	0.0094	101.8014	0.0101	0.1466	0.0123	0.0081	0.0062	0.052	0.0465	0.1891	0.0132	0.0084	0.0066
Core	Min	0.0071	0.015	0.019	0.0094	101.348	0.0101	0.13	0.0123	0.0081	0.0062	0.013	0.0465	0.18	0.0132	0.0084	0.0066
	Max	0.076	0.015	0.019	0.0094	102.097	0.0101	0.16	0.0123	0.0081	0.0062	0.13	0.0465	0.201	0.0132	0.0084	0.0066
KUJ13	Mean	0.0383	0.015	0.019	0.0094	102.0289	0.0101	0.1588	0.0123	0.0081	0.0062	0.0364	0.0465	0.197	0.0132	0.0262	0.0066
Rim	Min	0.0071	0.015	0.019	0.0094	101.53	0.0101	0.14	0.0123	0.0081	0.0062	0.018	0.0465	0.183	0.0132	0.0084	0.0066
	Max	0.061	0.015	0.019	0.0094	102.578	0.0101	0.175	0.0123	0.0081	0.0062	0.069	0.0465	0.214	0.0132	0.081	0.0066
KUJ17	Mean	0.0126	0.015	0.019	0.0385	102.3778	0.0101	0.0985	0.0123	0.0081	0.0062	0.04	0.0465	0.2048	0.0132	0.0616	0.0066
Core	Min	0.0071	0.015	0.019	0.0094	102.133	0.0101	0.084	0.0123	0.0081	0.0062	0.019	0.0465	0.179	0.0132	0.0084	0.0066
	Max	0.029	0.015	0.019	0.07	102.624	0.0101	0.111	0.0123	0.0081	0.0062	0.056	0.0465	0.221	0.0132	0.087	0.0066
KUJ17	Mean	0.0365	0.015	0.019	0.0161	102.2373	0.0101	0.0913	0.0123	0.0081	0.0062	0.0579	0.0465	0.2086	0.0132	0.0458	0.0066
Rim	Min	0.0071	0.015	0.019	0.0094	101.629	0.0101	0.078	0.0123	0.0081	0.0062	0.0089	0.0465	0.194	0.0132	0.0084	0.0066
	Max	0.078	0.015	0.019	0.076	102.75	0.0101	0.102	0.0123	0.0081	0.0062	0.177	0.0465	0.238	0.0132	0.101	0.0066
PG26	Mean	0.0377	0.0150	0.0190	0.0429	102.3101	0.0101	0.0956	0.0123	0.0081	0.0062	0.0749	0.0465	0.2154	0.0132	0.0606	0.0066
Core	Min	0.0071	0.0150	0.0190	0.0094	101.6290	0.0101	0.0780	0.0123	0.0081	0.0062	0.0089	0.0465	0.1940	0.0132	0.0084	0.0066
	Max	0.0780	0.0150	0.0190	0.0760	102.7500	0.0101	0.1110	0.0123	0.0081	0.0062	0.1770	0.0465	0.2380	0.0132	0.1010	0.0066
PG26	Mean	0.0391	0.0150	0.0190	0.0428	102.2756	0.0101	0.0953	0.0123	0.0081	0.0062	0.0801	0.0465	0.2156	0.0132	0.0589	0.0066
Rim	Min	0.0071	0.0150	0.0190	0.0094	101.6290	0.0101	0.0780	0.0123	0.0081	0.0062	0.0089	0.0465	0.1940	0.0132	0.0084	0.0066
	Max	0.0780	0.0150	0.0190	0.0760	102.7500	0.0101	0.1110	0.0123	0.0081	0.0062	0.1770	0.0465	0.2380	0.0132	0.1010	0.0066
PG28	Mean	0.0167	0.015	0.019	0.0094	102.4043	0.0101	0.0713	0.0123	0.0081	0.0062	0.0846	0.0465	0.218	0.0132	0.0084	0.0066
Core	Min	0.0071	0.015	0.019	0.0094	102.116	0.0101	0.067	0.0123	0.0081	0.0062	0.0089	0.0465	0.215	0.0132	0.0084	0.0066
	Max	0.036	0.015	0.019	0.0094	102.64	0.0101	0.074	0.0123	0.0081	0.0062	0.162	0.0465	0.223	0.0132	0.0084	0.0066
PG28	Mean	0.0307	0.015	0.019	0.0261	102.3025	0.0101	0.0828	0.0123	0.0081	0.0062	0.0869	0.0465	0.2173	0.0132	0.0322	0.0066
Rim	Min	0.0071	0.015	0.019	0.0094	101.629	0.0101	0.067	0.0123	0.0081	0.0062	0.0089	0.0465	0.194	0.0132	0.0084	0.0066
	Max	0.078	0.015	0.019	0.076	102.75	0.0101	0.111	0.0123	0.0081	0.0062	0.177	0.0465	0.238	0.0132	0.101	0.0066
PG31	Mean	0.0293	0.0150	0.0190	0.0233	102.3070	0.0101	0.0789	0.0123	0.0081	0.0062	0.0881	0.0465	0.2175	0.0132	0.0278	0.0066
Core	Min	0.0071	0.0150	0.0190	0.0094	101.6290	0.0101	0.0670	0.0123	0.0081	0.0062	0.0089	0.0465	0.1940	0.0132	0.0084	0.0066
	Max	0.0780	0.0150	0.0190	0.0760	102.7500	0.0101	0.1110	0.0123	0.0081	0.0062	0.1770	0.0465	0.2380	0.0132	0.1010	0.0066
PG31	Mean	0.0071	0.015	0.019	0.0094	102.363	0.0101	0.1	0.0123	0.0081	0.0062	0.0089	0.0465	0.2	0.0132	0.0084	0.0066
Rim	Min	0.0071	0.015	0.019	0.0094	102.363	0.0101	0.1	0.0123	0.0081	0.0062	0.0089	0.0465	0.2	0.0132	0.0084	0.0066
	Max	0.0071	0.015	0.019	0.0094	102.363	0.0101	0.1	0.0123	0.0081	0.0062	0.0089	0.0465	0.2	0.0132	0.0084	0.0066

9 Discussion

9.1 Origin of Magnetite Ore from Kiirunavaara and Per Geijer

Trace element composition of magnetite from IOA's was already intensely investigated by several authors (e.g., Dare et al., 2014a, 2014b; Huang et al., 2013; Knipping et al., 2015; Müller et al., 2003). The results report signatures typical of hydrothermal and magmatic magnetite. In this study a modified version of the discrimination diagram proposed by Dare et al. (2014a) is chosen to identify the origin of Kiirunavaara and Per Geijer magnetite (figure 9.1). The plot shows the mean of the trace element data obtained by EMPA, normalised to the composition of the bulk continental crust. The elements are ordered from decreasing to increasing compatibility into magnetite.

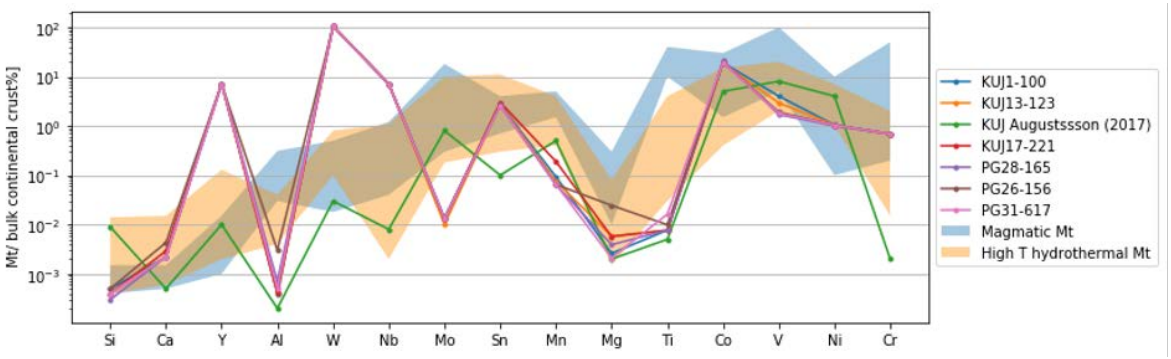

Figure 9.1 Modified version of the multi-element discrimination diagram that distinguishes between magmatic and high-T hydrothermal magnetite (Dare et al. 2014a). The plot shows the normalized data of KUJ1-100, KUJ13-123, KUJ17-221, PG26-156, PG28-165, PG31-617 and data from Augustsson (2017) for comparison. The plot was created with Python.

The elements Si, Ca, Co, Mg, V, Al, Mn, Ti plot either in or near the hydrothermal field or where the magmatic and hydrothermal fields overlap. The trace element signature of Kiirunavaara and Per Geijer thus shows magmatic and high-T hydrothermal features. It must be noted that elements with analysis below the lower analytical detection limit (D.L.; Y, W, Sn, Nb, Mo, Cr throughout < D.L. ; Ca, Al, Ti, Mn: some values < D.L.) were set on half D.L. in this plot. The informative value of these elements is therefore low. Trace element data of magnetite from Kiirunavaara, obtained by laser ablation inductively coupled plasma (LA-ICP-MS) by Augustsson (2017) was used for comparison and completion if EMPA detection limits were too high. Most of Augustsson's (2017) data plots in the overlapping fields of magmatic and hydrothermal magnetite. Thus, both data sets are in accordance with one another (for values where reasonable EMPA measurements are obtained). The only real difference is the higher Al and the higher Mg content of PG26-156. However, LA-ICP-MS has the advantage of lower detection compared to EMPA so that more information is available. Tungsten, Y, Nb, Mo, Sn, Ni and Cr show magmatic and hydrothermal signals as well.

The trace element signature of magnetite from Kiirunavara and Per Geijer is therefore in accordance with findings from many other IOA deposits reporting magmatic and hydrothermal features. The high V and Co contents were mostly interpreted as a sign of magmatic origin since V and Co are highly compatible during fractionation (Dare et al., 2014a). However, the V content of magnetite investigated in this study is not particularly high, as magnetite plots in the hydrothermal field rather than the magmatic field. Yet, the V data measured by EMPA must be interpreted with caution, since V overlap correction had to be implemented. LA-ICP-MS data plots in the overlapping field close to the magmatic-only field. This seems more reasonable, also with regards to the ICP-MS data of bulk rock where V levels are high (figure 8.45). Generally, interpreting the Co and V content can be ambiguous since magnetite derived from high-temperature hydrothermal fluids (∼500–700 °C) associated with a magmatic-hydrothermal source (e.g., IOCG) are also enriched in V and Co with almost the same concentrations as magnetite from evolved intermediate magmas. Another feature pointing towards a magmatic

origin is reported by Müller et al. (2003), who detected high Mn (compatible during magmatic fractionation) values around 2% in magnetite grains from Kiirunavaara. This could not be confirmed in this study, where Mn contents are quite low. Mn is however measured with little cps, consequently a certain analytical error has to be assumed. Yet, Augustsson (2017) reports similar low Mn values. Signs for a hydrothermal origin are low values of Ti, Ni and Cr, as well elements which are considered as compatible during magmatic fractionation, but immobile in hydrothermal systems. The ratio of Ni/Cr is according to Dare et al. (2014a) a useful tool to differentiate between hydrothermal and magmatic magnetite. In silicate magmas, their behavior is coupled, resulting in Ni/Cr ratios <1, as both behave compatible during fractionation of intermediate and felsic melts. In hydrothermal environments, in contrast, their behavior is decoupled and the Ni/Cr ratio of magnetite is typically higher 1, according to Dare et al. (2014a) due to a higher solubility of Ni compared to Cr in hydrothermal fluids. Nickel and Cr contents in the magnetites measured by EMPA are very low and do not exceed D.L., so the Ni/Cr ratio can only be calculated using the Cr and Ni values measured by ICP-MS on the pulp samples. Due to very low Cr and quite high Ni contents the ratio ranges from 2.5 to 37 in Kiirunavaara and from 0.5 to 62 indicating a hydrothermal origin. Trace elements give thus ambiguous signals.

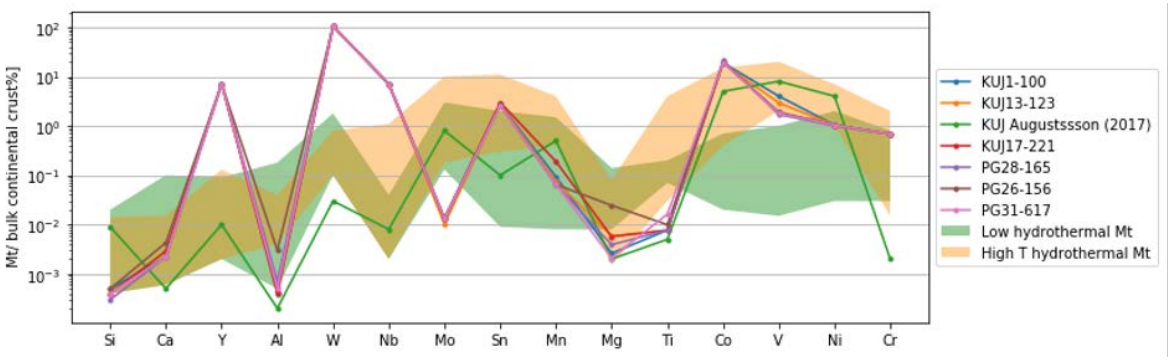

Figure 9.2 Modified version of the multi-element discrimination diagram that distinguished between low-T and high-T hydrothermal magnetite (Dare et al. 2014a). The plot shows the normalzed data of KUJ1-100, KUJ13-123, KUJ17-221, PG26-156, PG28-165, PG31-617 and data from Augustsson (2017) for comparison.

But not just a magmatic or magmatic-hydrothermal (high-T) source is proposed for the origin of IOA deposits. An exhalative-sedimentary hydrothermal origin was invoked by Parák, (1975a) and is subsequently supported by other authors including Loberg & Horndahl (1983). Therefore, an involvement of low-T hydrothermal (<500°C) fluids in ore generation needs to be investigated. In order to do so, the EMPA data of Kiirunavaara and Per Geijer normalized to bulk continental crust is plotted in the high-T/low-T hydrothermal discrimination diagram proposed by Dare et al. (2014a). Most of the data from Kiirunavaara and Per Geijer (for which reasonable results are obtained) plot in the high-T hydrothermal field or the overlapping field (figure 9.2). Augustsson's (2017) data is in accordance with this findings except for Sn. Magnetite that forms from fluids of lower temperature is not expected to have high contents of Co and V (Nadoll et al., 2014). A low-T hydrothermal origin therefore seems unlikely and a magmatic and/ or high-T hydrothermal origin can be assumed.

A theory that aims to explain the magmatic and high-T hydrothermal signatures within the magnetites from IOA deposits is proposed by Knipping et al. (2015). This theory involves the crystallization of magnetite microlites from magma, bubble nucleation on these magnetite microlites and subsequent ascend of the microlite-bubble pairs via efficient floatation by buoyancy within a Cl-rich fluid and deposition in local faults. In these hydrothermal fluids, the magnetite crystals continue to grow, resulting in two different stages of formation. The core of the magnetites consequently displays magmatic signatures, whereas the rim has hydrothermal features. This model is accepted by many authors that investigated magnetite and apatite from the Chilean iron ore belt (Palma et al., 2019; Palma et al., 2020; La Cruz, 2020). Apatite results from Kiirunavaara and Per Geijer are discussed in the next section.

9.2 Hints from Volatile Geochemistry in Apatites regarding Ore-forming Processes

Generally the apatites from the Kiirunavaara and the Per Geijer deposits are fluorapatites with very little amounts of Cl and OH. In the measured apatites the Z site is predominantly (>97%) occupied by F, suggesting primary apatite formed during igneous conditions (Piccoli & Candela, 2002). A composition of 3.77 wt% F is considered as the end member composition of fluorapatites (Webster & Piccoli, 2015). However, several apatites from Kiirunavaara and Per Geijer exceed a F composition of 3.77 wt% (figure 8.48). This might imply analytical problems, but fluorapatites exceeding end

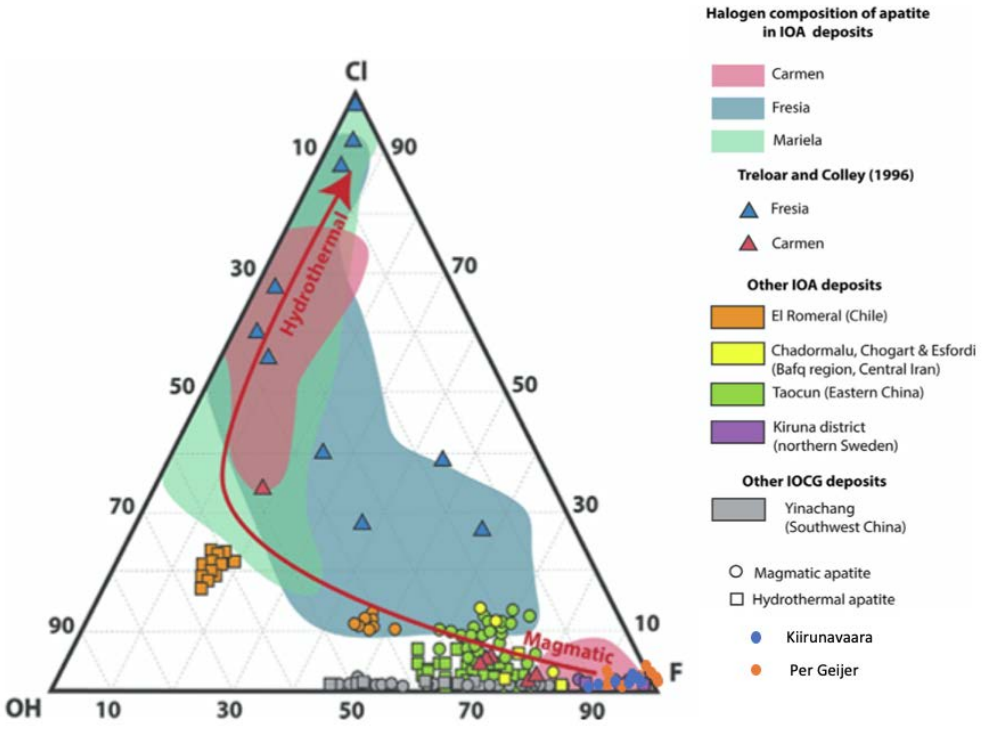

Figure 9.3 Ternary diagram of the halogen content in apatite regarding the F-Cl-OH atomic proportions from Palma et al. (2019). The diagram shows apatite composition of Kiirunavaara and Per Geijer in the lower right corner of the diagram within the magamtic field. Data from other IOA deposits are shown as comparison. Data includes: Carmen, Fresia, Marielea (Palma et al., 2019); El Romeral, Chile (Rojas et al., 2018b); deposits of the Bafq region, Central Iran (Taghipour et al., 2015); Kiruna district, northern Sweden (Harlov et al., 2002); Yinachang, Southern China (Li and Zhou, 2015), Taocun (Zeng et al., 2016) and data from Carmen and Fresia (triangles) reported by Treloar and Colley (1996).

composition are reported from several IOA deposits including Kiirunavaara and therefore seems to be a common feature in IOA deposits (Harlov et al., 2002; La Cruz et al., 2020; Webster & Piccoli, 2015).

The ternary diagram for halogen composition by Palma et al. (2019; figure 9.3), used to distinguish between magmatic and hydrothermal apatite, indicates a magmatic origin for all measured apatites from Kiirunavaara and Per Geijer as well. These results are in accordance with data from the Kiruna area by Harlov et al. (2002) and with some of the apatite data from the Bafq region (Taghipour et al., 2015). The majority of the halogen data from other IOA deposits, however, deviates from data of this study. Especially apatites from the Chilean iron ore belt, including the deposits Carmen, Fresia and Mariela, show significantly higher Cl and OH contents. Carmen is mainly composed of F and chlorapatites (Cl apatites), whereas Fresia and Mariela are dominated by hydroxyapatites (OH apatites) and Cl apatites (Palma et al., 2019; Treloar and Colley 1996). El Romeral shows a tendency to OH apatites (Rojas et al., 2018b).

The floatation model by Knipping et al. (2015) that was already introduced in the last section is invoked to explain the formation of the Chilean iron ore belt. The fluorapatites from Carmen are considered as primary according to this model. Some of the Carmen apatites only show a primary composition in the core and secondary Cl-OH composition along fractures and in the crystal rim. This suggests restricted alteration/ replacement with low fluid interaction. Alteration in Mariela and Fresia, in contrast, was more pervasive with higher fluid-apatite interaction where the primary F apatite was partially to completely replaced by Cl-OH (Palma et al., 2019). An increase in Cl content from core to rim is observed in some of the apatites from Per Geijer and Kiirunavaara as well. The difference, however, is minor and Cl and OH concentration remain low. This phenomenon can therefore hardly be compared to the metasomatic alteration observed in the Chilean apatites.

Due to the lack of Cl apatites in Kiirunavaara and Per Geijer, this model could only fit when assuming a lack of alteration overprint for the IOA deposits in Norrbotten,

where only fluorapatites are present. However, the composition of apatites from Carmen that are considered as primary are different from the primary apatites measured in this study. The composition of Carmen apatites ranges from 3.0-3.6 wt% F and 0.01-0.5 wt% Cl. Apatites from Kiirunvaara and Per Geijer are richer in F and lower in Cl with half of the apatites showing F end member composition (>3.77 wt%).

A study from Peters et al. (2019) based on triple O isotope data ($^{17}O/^{16}O$ and $^{18}O/^{16}O$ ratios) of magnetite from the IOA deposits of the Yazd and Sirjan areas in central Iran invokes a magmatic origin of Iranian IOA's with magmatic fluid interaction with evaporite and carbonate host rocks. Lehmann et al. (pers. comm.) investigate the triple O isotope data ($^{17}O/^{16}O$ and $^{18}O/^{16}O$ ratios) of magnetite from Kiirunavaara and come to similar findings pointing towards a magmatic origin with evaporite-carbonate fluid interaction. This model, in contrast to the flotation model by Knipping et al. (2015) is not just able to explain hydrothermal and magmatic signals of the magnetite, but also the high F content in the apatites. Piccoli & Candela (2002) report that F tends to overfill the Z site in carbonatic systems when significant CO_3^{2-} is present in the magma. Magma interacting with evaporites and carbonates would have to be extremely rich in volatiles, which are widely accepted to play a key role in ore formation since they are highly efficient - especially chlorine - to form complexes with metals (Auippa et al., 2009). Hou et al. (2018) showed that intermediate magmas develop liquid immiscibility at 100 MPa and 1000–1040°C. Some of the immiscible melts generated in the experiments are highly enriched in iron, phosphorous ± calcium, and strongly depleted in silicon. These Si-poor melts are in equilibrium with a rhyolitic conjugate and are formed under oxidized conditions, high water activity and within a fluorine-bearing systems. Thus, their results show that increasing water activity and increasing oxidizing conditions allow the Fe–Ca–P melt to separate from host silicic magma generating iron oxide apatite ores. Fluorine is proven to play an important role during this process since it is complexing with Mg in the melt and therein decreasing the activity of MgO, which increases the activity of FeO resulting in liquid immiscibility. In addition, carbonates and evaporites are as well attributed to be of great importance by significantly

oxidizing magmas (Hou et al., 2018). The experiments show also that the melts, which generate liquid immiscibility are of similar composition as the natural felsic rocks that typically host Kiruna-type IOA deposits including the KUJ and PG drillcores that are examined in this study (figure 9.4). After melt separation, the volatiles can concentrate in the residual melt and may separate from it resulting in a decrease in p-T conditions or increasing crystallisation (Roedder, 1992). This phenomena could account for the hydrothermal signals within the ore. Additionally, Cl and F act as fluidizers by breaking the silicate tetraheder within the melt (Dolejs & Zajacz, 2018), which can as well contribute to the ore showing hydrothermal signals.

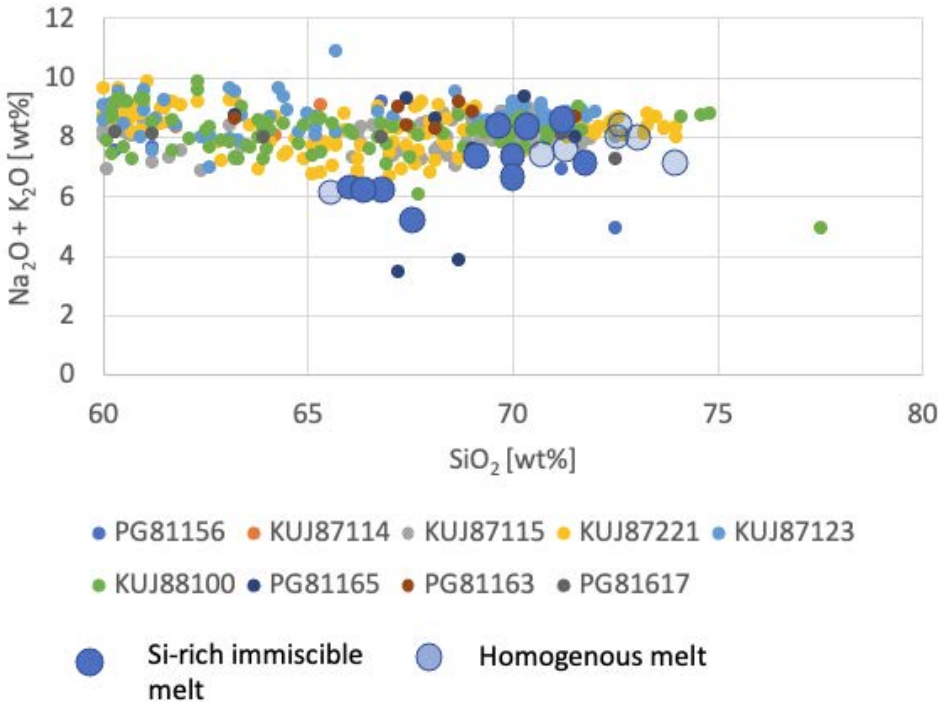

Figure 9.4 Experimental Si-rich melts by Hou et at. (2018). Many of these immiscible Si-rich melts are similar to the natural felsic rocks in Kiirunavaara and Per Geijer. The ICP-OES data of the drillholes was used for the plot.

Considering these findings the model of formation suggested in this study is as follows:

- A magma of probably intermediate composition is injected into the crust.
- Interaction with evaporite and carbonate host rocks changes the initial composition of the magma.

- Separation of an Fe-P-volatile rich melt from the silicic magma due to liquid immiscibility induced by oxidizing conditions and high water activity.

- Volatiles concentrate in the residual melt and may separate and ascend, resulting in lower pressure and temperature conditions or increasing crystallisation.

Fluid inclusions investigated by Smith et al. (2013) state a NaCl content of 31.4-36.6 wt% in Kiirunavaara and 33.3-37.9 wt% NaCl in Henry, which confirms a high Cl content during formation. The regional occurrence of scapolite that is reported by several authors (e.g., Frietsch et al., 1997; Martinsson et al., 2016) and was as well observed during core logging and in sample PG29-165, can be seen as evidence that evaporites have been mobilized.

9.3 Hints from Apatite Textures and Trace elements

Apatites from Kiirunavaara and Per Geijer are zoned, showing a lighter grey in the core and a darker grey towards the rim in backscattered-electron (BSE) images. This zonation cannot be attributed to the increase of Cl from core to rim that is reported in this study, since Cl differences are minor. Palma et al. (2019) report altered apatites with leached outer rims and fracture zones, where the initial halogen composition is replaced by Cl and OH. These apatites show a significantly lighter grey around the crystal rim and darker grey towards the core. Harlov et al. (2002) and Darling & Florence (1995) found the same inverse zonation of apatites with lighter core and darker rim in samples from Kiirunavaara, that was observed in this study. They attribute this to changes in LREE, Si, Na, and S content. The brighter internal areas of the apatite show significantly higher contents of these elements. A decrease in Ce and La from core to rim is as well observed in half of the measured apatites in this study. It must, however, be noted that Ce and La were measured with little cps and therefore the analytical uncertainty is large. Silicium, Na, S and other LREE are not measured.

Monazite inclusions are observed in Kiirunavaara and Per Geijer (figure 8.39, figure 8.38). Harlov et al. (2002) explains the existence of monazite by fluid-rock interaction at high temperature (∼800 °C) in late-stage magmatic phases shortly after the emplacement and crystallisation of the ore bodies. Thus, Na and Si have been leached by high salinity fluids that transported ore metals as well as other cations such as Si, Na, K, Mg, Ca, and (Y + REE) and a subsequent precipitation of the monazite inclusions occurred (Harlov et al., 2002). This theory is supported by experiments performed by Harlov & Förster (2003) that involve fluorapatite and a variety of fluids including H_2O, CO_2 – H_2O mixtures, and KCl brines. These fluids resulted in interaction with the apatites in the formation of monazite as inclusions in the fluorapatite at T >850 °C. Monazite formation is subsequently coupled with an associated depletion in Y + REE + Na + Si in the apatite. These inclusions can therefore be seen as another evidence for a magmatic origin of the ore. Monazite inclusions are as well reported in

apatites from other IOA deposits including the Bafq district (Bonyadi et al., 2010) and Carmen, Isabela and Fresia from the Chilean iron ore belt (Palma et al., 2019).

9.4 Hints from Element Geochemistry in Bulk Rock

The minor and trace element signature within the bulk rock samples does not strongly differ between the Kiirunavaara and the Per Geijer samples. Therefore, a similar mode of formation seems likely. Elemental correlations (correlation matrices can be found in the appendix) are however very different. This can on one hand be explained by the different mineralogy of the samples, but especially in the PG samples, element correlations occur that do not fit in the mineralogical assemblages (e.g, Al-Hf, As-Mg, Rb-Al). These element pairs can be explained by hydrothermal alteration/replacement by fluid rock interaction. Low to moderate concentrations of K confirm that the sampled areas from Kiirunavaara exhibit an overall low degree of alteration, whereas the sampled areas from Per Geijer show an overall moderate or even strong degree of alteration. The aim to take samples that reflect primary conditions was thus not entirely successful. Both of the deposits are considerably old ($\sim$ 1.9 Ga). During greenshist facies the rocks were altered by fluids of probably 300–400 °C (Harlov et al., 2002), sampling primary conditions is consequently not possible. However, the samples, especially the ones from Kiirunavaara are not strongly altered and almost reflect primary conditions. Younger IOA deposits e.g., Los Colorados from the Chilean iron ore belt show higher amounts of trace elements and alteration overprint is reported to be minimal so that these deposits of $\sim$100 Ma age reflect rather primary conditions than the ones in Norrbotten.

Another hint that hydrothermal overprint occurred is the presence of hematite in Per Geijer. The existence of ubiquitous relict magnetite within the hematite and the presence of martitization proofs that hematite is a secondary oxidation product. Hydrothermal overprinting at lower temperatures is as well expressed by the presence of secondary minerals including chlorite, calcite and sulfides, which is especially the case for PG samples and to a lesser extend for KUJ samples.

9.5 Mining Potential of the Per Geijer, Henry Deposit

The samples from the Per Geijer Henry deposits show a high iron grade (average 20% Fe) and are also enriched in P (average 2.7 % P), REE and several other critical elements including As, Ba, Co, V and W. However, the high W content may also be due to contamination by the tungsten-carbide swing mill that was used for milling the samples.

An important factor in the reassessment campaign of the resource potential of PG is also the characterisation of trace elements in the iron ore, as they might influence the final products (iron ore pellets) in regards to steel making processes. Currently, there are limited studies that investigate the influence of trace elements in iron oxides on final products, but an inhouse project of LKAB (Niiranen 2015; Töyrä et al. 2017; Niiranen et al. 2018; Niiranen and Rutanen 2019) recently pointed out that especially Ti content might be problematic and Ti distribution requires further investigation.

Due to product regulations on the market, vanadium, Cr, Co and Ni require as well examination. Chromium and Ni contents in magnetite in this study never exceed D.L. and V and Co show about the same concentrations as the magnetite from Kiirunavaara. These elements can therefore be categorized as not problematic with regards to the production of iron ore pellets. Titanium contents are as well below D.L. except for sample PG26-156. However, TiO_2 content here is low, ranging from 0.0081% to 0.023%, which is in accordance with product regulations (Kroplop et al., 2019).

In Per Geijer, iron is unlike to Kiirunavaara, present as hematite and magnetite. This means that LKAB would have to enlarge their product portfolio in the form of an hematite concentrate and research needs to be shifted from a magnetite-only focus to a hematite-magnetite focus. Trace element investigation of hematite grains was not conducted in the scope of this study, but a first characterisation was carried out by Kroplop et al. (2019). Kroplop reported Per Geijer hematite to be not problematic with regards to V, Cr, Co and Ni but some areas within Per Geijer are elevated in Ti with a content up to 2%, requiring further investigation.

10 Conclusion

In order to put new constraints on the formation of IOA's in Norrbotten, samples from Kiirunavaara and Per Geijer are investigated regarding their trace element signature. The chemical composition of magnetite and apatite was analyzed by EMPA and bulk rock was analyzed by ICP-MS. Many important trace elements including Cr and Ni do not exceed detection limits in EMPA measurements of magnetite so that the applied discrimination diagrams have a limited informative value. It can be concluded that LA-ICP-MS is a more appropriate tool for trace element spot analysis than EMPA. It can, however, be determined that magnetites from Kiirunavaara and Per Geijer record both magmatic (high Co and V contents) and hydrothermal features (low Cr, Ni, Ti contents).

Apatites from Kiirunavaara and Per Geijer are all fluorapatites, formed during igneous conditions. Several apatites from both deposits show F end member composition (>3.77 wt% F) pointing towards magma interaction with evaporates and carbonates. The regional occurrence of scapolite in the Norrbotten area can be seen as evidence for a former evaporate bed within the stratigraphy. This theory is supported by Peters et al. (2019) and Lehmann (pers. comm.) who investigate triple O isotope data ($^{17}O/^{16}O$ and $^{18}O/^{16}O$ ratios) of magnetite from Yazs and Siran (Iran) and the Kiruna area. Experiments conducted by Hou et al. (2018) confirm that fluorine can significantly oxidize magmas, which aids a Fe-P rich melt to separate from a silicic melt generating IOA's. Monazite inclusions within the apatite that are supposed to crystallize at temperatures around 800°C are another evidence for a magmatic origin.

The mode of formation this study invokes includes 1) injection of an intermediate magma into the upper crust, 2) magma interaction with evaporitic and carbonatic host rocks, 3) liquid immiscibility causing the silicic and the Fe-P-volatile rich magma to separate, and 4) concentration of volatiles within the residual melt leading to a drop in pressure and temperature shifting the conditions towards a hydrothermal environment.

A little distinct minor and trace element signature in both the magnetite grains and in the whole rock samples such as a similar apatite geochemistry point towards a similar mode of formation for the Kiirunavaara and the Per Geijer deposits.

11 Outlook

Since EMPA measurements did not deliver reliable results for all trace elements of interest it is suggested to as well conduct a trace element analysis with LA-ICP-MS. In order to make an appropriate decision on remining the Per Geijer deposits, trace element analysis should target hematite as well as magnetite.

Most of the trace element studies carried out so far only focus on the nature of origin. Since mining companies face challenges with varying ore qualities, research could as well investigate the influence of trace elements on the final product, especially with regards to the steel making process.

12 Bibliography

Aiuppa, A., Giudice, G., Guerrieri, S., Liuzzo, M., Burton, M., Caltabiano, T., McGonigle, A.J.S., Salerno, G., Shinohara, H., Valenza, M. (2008) The total volatile flux from Mount Etna and implications for the geochemical monitoring of basaltic volcanoes. Geophys. Res. Lett. 35, L24302 doi:10.1029/2008GL035871.

Augustsson, C. (2017) Trace element geochemistry of magnetite from the Kiirunavaara Iron-Apatite ore, as determined by LA-ICP-MS. Geovetarcentrum Göteborg University.

Barton, M. D. (2014) Iron oxide(–Cu–Au–REE–P–Ag–U–Co) systems. In Treatise of Geochemistry (eds. H. Holland and K. Turekian) v. 13, pp. 515–536.

Bea F., Pereira M. D. and Stroh A. (1994) Mineral/leucosome trace-element partitioning in a peraluminous migmatite (a laser ablation-ICPMS study). Chem. Geol. 117, 291–312.

Belousova E. A. (2000) Trace elements in zircon and apatite: application to petrogenesis and mineral exploration PhD thesis. Macquare University, Australia.

Belousova E. A., Walters S., Griffin W. L. and O'Reilly S. Y. (2001) Trace element signatures of apatites from granitoids of Mount Isa Inlier, north-west Queensland Australia. Aust. J. Earth Sci. 48, 603–619.

Dare SAS, Barnes S-J, Beaudoin G. (2012) Variation in trace element content of magnetite crystallized from a fractionating sulfide liquid, Sudbury, Canada: implications for provenance discrimination. Geochim Cosmochim Acta 88:27–50.

Dare, S. A. S., Barnes, S-J., Beaudoin, G., Méric, J., Boutroy, E., / Potvin-Doucet, C. (2014a) Trace elements in magnetite as petrogenetic indicators. Mineralium Deposita.

Dare, S. A. S., Barnes, S-J., Beaudoin, G. (2014b) Did the massive magnetite "lava flows" of El Laco (Chile) form by magmatic or hydrothermal processes? New constraints from magnetite composition by LA-ICP-MS. Mineralium Deposita.

Darling, R.S., Florence, F.P., (1995) Apatite light rare earth element chemistry of the Port Leyden nelsonite, Adirondack Highlands, New York: implications for the origin of nelsonite in anorthosite suite rocks. Econ. Geol. 90, 964–968.

Dolejš, D., Zajacz, Z. (2018) Halogens in silicic magmas and their hydrothermal systems. In The role of halogens in terrestrial and extraterrestrial geochemical processes (pp. 431-543). Springer, Cham.

Frietsch, R. (1978) On the magmatic origin of iron ores of the Kiruna type. Econ. Geol. 73, 478-485.

Frietsch, R., Tuisku, P., Martinsson, O., Perdahl J.-A. (1997) Cu-(Au) and Fe ore deposits associated with Na-Cl metasomatism in early Proterozoic rocks of northern Fennoscandia: a new metallogenic province. Ore Geol. Rev. 12, 1–34.

Geijer, P. (1910) Igneous rocks and iron ores of Kiirunavaara, Luossavaara and Tuolluvaara. Econ. Geol. 5, 697– 718.

Geijer, P. (1930) Geology of the Gällivare ore field. Geol. Surv. Sweden Ca 22 (115 pp).

Geijer, P. (1931) Berggrunden inom malmtrakten Kiruna-Gällivare-Pajala. Geol. Surv. Sweden C 366 (225 pp).

Goldschmidt, V.M. (1954) Geochemistry Oxford University Press, Oxford.

Groves, D.I., Bierlein, F.P., Meinert, L.D., Hitzman, M.W., 2010. Iron oxide copper-gold (IOCG) deposits through Earth history: Implications for origin, lithospheric setting, and distinction from other epigenetic iron oxide deposits. Econ. Geol. 105, 641–654.

Harlov, D. E., Andersson, U. B., Förster, H. J., Nyström, J. O., Dulski, P., Broman, C. (2002) Apatite–monazite relations in the Kiirunavaara magnetite–apatite ore, northern Sweden. Chemical Geology, 191(1-3), 47-72.

Harlov, D.E., Förster, H.-J., Nijland, T.G., (2002) Fluid induced nucleation of (Y + REE) – phosphate minerals in apatite: nature and experiment. Part I. Chlorapatite. Am. Mineral. 87, 245–261.

Hitzman, M.W., Oreskes, N., Einaudi, M.T. (1992) Geological characteristics and tectonic setting of Proterozoic iron oxide (Cu-U-Au-REE) deposits. Precambrian Res. 58, 241-287.

Huang, X. W., Sappin, A. A., Boutroy, É., Beaudoin, G., Makvandi, S. (2019) Trace Element Composition of Igneous and Hydrothermal Magnetite from Porphyry Deposits: Relationship to Deposit Subtypes and Magmatic Affinity. Economic Geology, 114(5), 917-952.

Hou, T., Charlier, B., Holtz, F., Veksler, I., Zhang, Z., Thomas, R., Namur, O. (2018). Immiscible hydrous Fe–Ca–P melt and the origin of iron oxide-apatite ore deposits. Nature communications, 9(1), 1-8.

Knipping, J. L., Bilenker, L. D., Simon, A. C., Reich, M., Barra, F., Deditius, A. P. & Munizaga, R. (2015). Trace elements in magnetite from massive iron oxide-apatite deposits indicate a combined formation by igneous and magmatic-hydrothermal processes. Geochimica et Cosmochimica Acta, 171, 15-38.

Krolop, P., Jantschke, A., Gilbricht, S., Niiranen, K., Seifert, T. (2019) Mineralogical Imaging for Characterization of the Per Geijer Apatite Iron Ores in the Kiruna District, Northern Sweden:

A Comparative Study of Mineral Liberation Analysis and Raman Imaging. Minerals 2019, 9, 544.

Kroplop, P. Richter, A., Niiranen, K., Gilbricht, S., Schulz, B., Oelze, M., Seifert, T. (2019) Trace element composition of iron oxides in the Per Geijer deposits in Kiruna, Northern Sweden. ISO 690

La Cruz, N.L., Ovalle, J.T., Simon, A.C., Konecke, B.A., Barra, F., Leisen, M., Reich, M., Childress, T.M. (2020) The geochemistry of magnetite and apatite from the El Laco iron oxide-apatite deposit, Chile: Implications for ore genesis: Econ. Geol. https://doi. org/10.5382/econgeo.4753.

Li X. and Zhou M.-F. (2015) Multiple stages of hydrothermal REE remobilization recorded in fluorapatite in the Paleoproterozoic Yinachang Fe-Cu-(REE) deposit, Southwest China. Geochim. Cosmochim. Acta 166, 53–73.

Lindsley, D.H., (1976b) Experimental studies of oxide minerals. In: Rumble III, D. (Ed.), Oxide Minerals. Rev. Mineral. Mineral. Soc. Am. , pp. L61–L88.

LKAB (2019) Technical Report Per Geijer. LKAB, Luleå (138 pp).

Loberg, B. E. H., Horndahl, A-K. (1983) Ferride geochemistry of Swedish Precambrian iron ores. Mineralium Deposita, 18(3), 487-504.

Martinsson, O., (1997) Paleoproterozoic greenstones at Kiruna in northern Sweden: a product of continental rifting and associated mafic-ultramafic volcanism. In Martinsson, O.: Tectonic setting and metallogeny of the Kiruna Greenstones. Ph.D. Thesis (1997) Luleå Univ. of Technology, Sweden, Paper I (49 pp).

Martinsson, O., (2004a) Geology and metallogeny of the northern Norrbotten Fe-Cu-Au province. In R.L Allen,

Martinsson O. and Weihed P. (eds.), 2004. "Svecofennian Ore-Forming Environments: Volcanic - associated Zn- Cu-Au-Ag, intrusion associated Cu-Au, sediment-hosted Pb-Zn, and magnetite-apatite deposits in northern Sweden". Soc. Econ. Geol., Guidebooks Series 33, 131-148.

Martinsson, O., Wanhainen, C., 2013. "Fe oxide and Cu-Au deposits in the Northern Norrbotten ore district". Geol. Surv. Sweden, Excursion Guidebook SWE5 (70 pp).

Martinsson, O. (2015) "Genesis of the Per Geijer apatite iron ores, Kiruna area, Northern Sweden. The 13th Biennial Meeting of The SGA, Nancy August 23-27, 2015, Abstract.

Martinsson, O., K. Billström, C. Broman, P. Weihed, C. Wanhainen (2016). Metallogeny of the Northern Norrbotten Ore Province, northern Fennoscandian Shield with emphasis on IOCG and apatite-iron ore deposits, Ore Geology Reviews, Volume 78, 2016, 447-492.

Müller, B., Axelsson, M.D. & Öhlander, B. (2003) Trace elements in magnetite from Kiruna, northern Sweden, as determined by LA-ICP-MS. GFF, Vol. 125 (Pt. 1, March), pp. 1–5. Stockholm. ISSN 1103-5897.

Nadoll P., Angerer T., Mauk JL., French D., Walshe J. (2014) The chemistry of hydrothermal magnetite: a review. Ore Geol Rev 61:1–32

Naslund H. R., Henriquez F., Nyström J. O., Vivallo W., Dobbs F. M. (2002) Magmatic iron ores and associated mineralisation: examples from the Chilean high Andes and coastal Cordillera. In Hydrothermal Iron Oxide-Copper-Gold A Global Perspec- tive, 2 (Ed. T. M. Porter). PGC Publishing, Adelaide, Australia, pp. 207–226.

Niiranen, K, (2015). Characterization of the Kiirunavaara iron ore deposit for mineral processing with the focus on the high silica ore type B2. PhD Thesis, Montanuniversitaet Leoben, Austria, 195 p. 456

Niiranen K., Töyrä V., and Krolop P. (2018). Reverse cationic flotation – a possibility to reduce silicate content in magnetite concentrate in LKAB's beneficiation plants in Kiruna. IMPC 2018 29th International Mineral Processing Congress. pp. 1136-1147

Niiranen, K., and Rutanen, H., (2019). Gangue mineralogy of titanium (Ti) in the Kiirunavaara iron ore deposit, northern Sweden. Proceedings Iron Ore 2019. 491-499.

Nold J. L., Dudley M. A. and Davidson P. (2014) The Southeast Missouri (USA) Proterozoic iron metallogenic province—Types of deposits and genetic relationships to magnetite–apatite and iron oxide–copper–gold deposits. Ore Geol. Rev. 57, 154–171.

Nyström, J.-O., Henriquez F. (1994) Magmatic features of iron ores of the Kiruna type in Chile and Sweden: ore textures and magnetite geochemistry: Econ. Geol. 89, 820-839.

Nyström, J.O., Billström, K., Henriquez, F., Fallick, A.E., Naslund, H.R. (2008) Oxygen isotope composition of magnetite in iron ores of the Kiruna-type in Chile and Sweden. Geol. Foren. Stock. For. 130, 177-188. Olesik, J. W. (1991) Elemental analysis using ICP-OES and ICP/MS. Analytical Chemistry, 63(1), 12A-21A.

Öhlander (2003) Trace elements in magnetite from Kiruna, northern Sweden, as determined by LA-ICP-MS. In:GFF125.1, pp. 1–5.

Palma, G., Barra, F., Reich, M., Valencia, V., Simon, A.C., Vervoort, J., Leisen, M., and Romero, R. (2019) Halogens (F, Cl, OH), trace element contents, and Sr-Nd isotopes in apatite from iron oxide-apatite (IOA) deposits in the Chilean iron belt: Evidence for magmatic and hydrothermal stages of mineralization: Geochimica et Cosmochimica Acta, v. 246, p. 515–540.

Pan Y. and Fleet M. (2002) Compositions of the apatite-group minerals: substitution mechanisms and controlling factors. Rev. Mineral. Geochem. 48, 13–50.

Parák, T. (1975a) The origin of the Kiruna iron ores (ser. C, no. 709). Stockholm: Sveriges Geologiska Undersökning. ISBN 91-7158-069-7

Peters, S. T., Alibabaie, N., Pack, A., McKibbin, S. J., Raeisi, D., Nayebi, N. and Lehmann, B. (2020) Triple oxygen isotope variations in magnetite from iron-oxide deposits, central Iran, record

magmatic fluid interaction with evaporite and carbonate host rocks. Geology, 48(3), 211-215.

Piccoli, P.M., and Candela, P.A. (2002) Apatite in igneous system: Reviews in Mineralogy and Geochemistry, v. 48, p. 255–292.

Pollard, J.P. (2006) An intrusion-related origin for Cu-Au mineralization in iron oxide-copper-gold (IOCG) provinces. Miner. Deposita 41, 179-187.

Porter, T.M. (2010) Current Understanding of Iron Oxide Associated-Alkali Altered Mineralised Systems; Part 1 - An Overview; Part 2 - A Review. In Porter, T.M. (ed.), 2010 - Hydrothermal Iron Oxide Copper-Gold and Related Deposits: A Global Perspective, volume 4, Advances in the Understanding of IOCG Deposits, PGC Publishing, Adelaide. Pp 5-106.

Ramdohr, P. (1926) Beobachtungen an Magnetit, Ilmenit, Eisenglanz, und Uberlegungen über das System FeO–Fe2O3–TiO2. Neues Jahrb. Mineral. 54A, 320–379.

Roser, B. P., Korsch, R. J. (1988) Provenance signatures of sandstone-mudstone suites determined using discriminant function analysis of major-element data. Chemical geology, 67(1-2), 119-139.

Rudnick, R. L., Gao, S. (2003) Composition of the Continental Crust. Treatise Geochem 3:1-64. Treatise on Geochemistry. 3. 1-64. 10.1016/B0-08-043751-6/03016-4.

Roedder, E., (1992) Fluid inclusion evidence for immiscibility in magmatic differentiation. Geochim. Cosmochim. Acta 56, 5 – 20.

Rojas, P., Barra, F., Deditius, A., Reich, M., Simon, A., Roberts, M., Rojo, M. (2018b) New contributions to the understanding of Kiruna-type iron oxide-apatite deposits revealed by magnetite ore and gangue mineral geochemistry at the El Romeral deposit. Chile. Ore Geol. Rev. 93, 413–435

Schettler G., Gottschalk M. and Harlov D. E. (2011) A new semi- micro wet chemical method for apatite analysis and its application to the crystal chemistry of fluorapatite-chlorapatite solid solutions. Am. Mineral. 96, 138–152.

Sha L. K. and Chappell B. W. (1999) Apatite chemical composi- tion, determined by electron microprobe and laser-ablation inductively coupled plasma mass spectrometry, as a probe into granite petrogenesis. Geochim. Cosmochim. Acta 63, 3861–3881.

Simon, A.C., Kniping, J., Reich, M., Barra, F., Deditius, A.P., Bilenker, L., Childress, T., (2018) Kiruna -Type Iron Oxide-Apatite (IOA) and Iron Oxide Copper-Gold (IOCG) Deposits form by a combination of ignous and magmatic-hydrothermal processes: evidence from the Chilean Iron Belt. SEG Sp. Pub. 21, 89–114.

Sillitoe, R.H., and Burrows, D.R. (2002) New field evidence bearing on the origin of the El Laco magnetite deposit, northern Chile: Economic Geology, v. 97, p. 1101–1109.

Smith, M.P., Gleeson, S.A., Yardley, B.W.D. (2013) Hydrothermal fluid evolution and metal transport in the Kiruna district, Sweden: Contrasting metal behaviour in aqueous and aqueous-carbonic

brines. Geochim. Cosmochim. Acta. 102, 89-112.

Schober, P., Boer, C., & Schwarte, L. A. (2018) Correlation coefficients: appropriate use and interpretation. Anesthesia Analgesia, 126(5), 1763-1768.

Smith, M.P., Storey, C.D., Jeffries, T.E., Ryan, C. (2009) In situ U-Pb and trace element analysis of accessory minerals in the Kiruna District, Norrbotten, Sweden: New constraints on the timing and origin of mineralization. J. Petrol. 50, 2063-2094.

Smith, M. P., Gleeson, S. A., Yardley, B. W. D. (2013) Hydrothermal fluid evolution and metal transport in the Kiruna District, Sweden: Contrasting metal behaviour in aqueous and aqueous –carbonic brines. Geochimica et cosmochimica acta, 102, 89-112.

Storey, C. D., Smith, M. P. (2017) Metal source and tectonic setting of iron oxide-copper-gold (IOCG) deposits: Evidence from an in situ Nd isotope study of titanite from Norrbotten, Sweden. Ore Geology Reviews, 81, 1287-1302.

Taghipour S., Kananian A., Harlov D. and Oberha nsli R. (2015) Kiruna-type iron oxide-apatite deposits, Bafq district, Central Iran: fluid-aided genesis of fluorapatite-monazite-xenotime assemblages. Can. Mineral. 00, 1–17

Toplis M. J. and Dingwell D. B. (1996) The variable influence of P2O5 on the viscosity of melts of differing alkali/aluminium ratio: Implications for the structural role of phosphorus in silicate melts. Geochim. Cosmochim. Acta 60, 4107–4121.

Töyrä, V., Niiranen, K., Niva, E. Rosendal, O. (2017). Increasing Silicate Content in the Kiruna Ore - a Challenge for Mineral Processing. Mineral Engineering 2017 Conference. Luleå University of Technology, Preprints, pp.149-159.

Treloar P. J. and Colley H. (1996) Variations in F and Cl concentrations in apatites from magnetite-apatite ores in northern Chile, and their ore-genetic implications. Mineral. Mag. 60, 285–301.

Velasco F., Tornos F. and Hanchar J. M. (2016) Immiscible iron- and silica-rich melts and magnetite geochemistry at the El Laco volcano (northern Chile): evidence for a magmatic origin for the magnetite deposits. Ore Geolg. Rev. 79, 346–366.

Waychunas, G.A. (1991) Crystal chemistry of oxides and oxyhydroxides. In: Lindsley, D.H. (Ed.), Oxide Minerals: Petrologic and Magnetic Significance. Mineralogical Society of America, pp. 11–61.

Webster, J.D., and Piccoli, P.M. (2015) Magmatic apatite: A powerful, yet deceptive, mineral: Elements, v. 11, p. 177–182.

Wechsler, B.A., Lindsley, D.H., Prewitt, C.T. (1984) Crystal structure and cation distribution in titanomagnetites (Fe3 xTixO4). Am. Mineral. 69, 754–770.

White, W. M. (2013) Geochemistry. John Wiley & Sons, chapter 77, pp. 258-265.

Williams P. J., Barton M. D., Johnson D. A., Fontbote L., de Haller A., Mark G., Oliver N. H. S.

and Marschik R. (2005) Iron oxide copper-gold deposits: geology, space-time distribution, and possible modes of origin. In Econ. Geol., 100th Anniversary Volume, (eds. J. W. Hedenquist, J. F. H. Thompson, R. J. Goldfarb, J. P. Richards). pp. 371– 405.

Williams, P.J., Kendrick, M.A., Xavier, R.P., 2010. Sources of ore fluid components in IOCG deposits. In Porter, T.M. (ed.), 2010 - Hydrothermal Iron Oxide Copper-Gold and Related Deposits: A Global Perspective, volume 3, Advances in the Understanding of IOCG Deposits, PGC Publishing, Adelaide, pp. 107-116.

Zeng L., Zhao X., Li X., Hu H. and McFarlane C. (2016) In situ elemental and isotopic analysis of fluorapatite from the Taocun magnetite-apatite deposit, Eastern China: constraints on fluid metasomatism. Am. Min. 101, 2468–2483.

Zhang, C., Vervoort, J., Barra, F., Palma, G., 2017. ICPMS Lu-Hf Geochronology of Apatite from Iron- Oxide Apatite (IOA) Deposits, Northern Chilean Iron Belt. Volcanology, Geochemistry, and Petrology General contributionsAGU Fall Meeting (Abstract 236799).

13 Appendix

13.1 Samples

This section contains pictures and a description of all 34 sample pieces. Note that only minerals that could have been identified in the hand specimen are listed here.

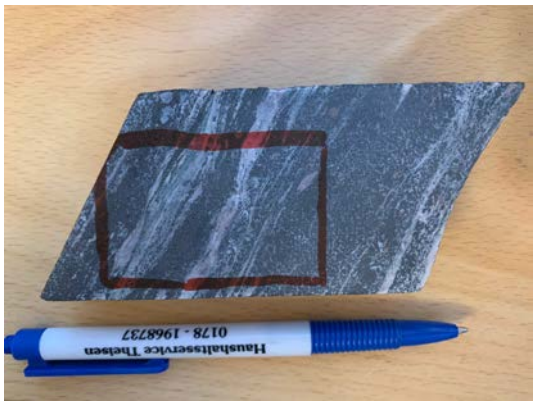

Figure 13.1 Sample piece KUJ1-100.

Figure 13.2 Sample piece KUJ2-100.

Sample KUJ1-100 was taken at 479.78 m depth of drillcore KUJ-88100 in the HW close to ore contact. The sample piece contains magnetite, apatite, K-feldspar and actinolite and is shown in figure 13.1. The rock is fine grained and layered.

Sample piece KUJ2-100 was taken at 475.70 m in the HW of KUJ-88100 and is shown in figure 13.2. Its composed of magnetite, actinolite, titanite and apatite. The rock is fine grained, mostly dark grey in colour with green actinolite patches. Close to the actinolite patches schlieren of pinkish K-feldspar occur.

Figure 13.3 Sample piece KUJ3-100.

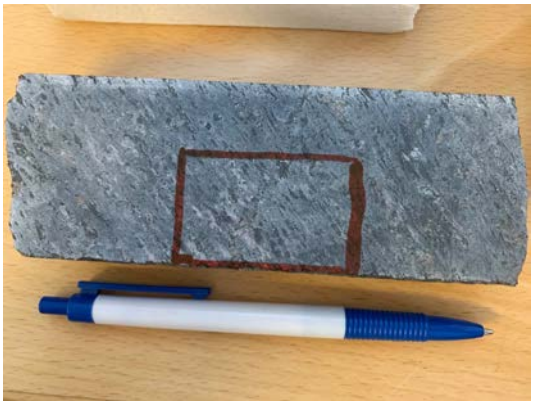

Figure 13.4 Sample piece KUJ4-100.

KUJ3-100 is shown in figure 13.3 was taken directly at the FW ore contact at 517.70 m in drillcore KUJ-88100. The sample contains magnetite, actinolite, apatite and titanite. The rock is fine grained and mainly dark grey in colour. Some whitish to greenish schlieren of gangue minerals occur.

KUJ4-100 can be seen in figure 13.4. The sample was taken at 530.50 m in the FW of KUJ-88100. Its composed of magnetite, apatite, actinolite and titanite. The sample consists of mostly gangue. The ore occurs dissiminated and vein like.

Figure 13.5 Sample piece KUJ5-115.

Figure 13.6 Sample piece KUJ6-115.

KUJ5-115 is shown in figure 13.5 and was taken at 390.80 m in ore zone of drillcore KUJ-87115. The sample contains mainly massive magnetite and little actinolite and is fine grained and dark grey in colour.

KUJ6-115 is presented in figure 13.6 and was taken at 404.52 m in the FW of drillcore KUJ-87115. It has a light grey colour and contains mainly magnetite, actinolite and little chlorite, which implies at least a certain degree of alteration overprint.

KUJ7-115 can be seen in figure 13.7 and was taken at 308.45 m at HW/ ore contact of drillcore KUJ-87115. The sample consists of mostly massive magnetite with spots of greenish actinolite and white schlieren of apatite.

KUJ8-115 is presented in figure 13.8 and was taken at 304.12 m in HW of core KUJ-87115. The sample piece was taken in an ore patch and consists of semi massive magnetite with a considerable amount of patches of green actinolite and reddish K-feldspar.

Figure 13.7 Sample piece KUJ7-115.

Figure 13.8 Sample piece KUJ8-115.

KUJ9-123 is shown in figure 13.9 and was taken at 148.78 m in the ore zone of drillcore KUJ-87123. The sample is dark grey with some white/greyish spots and contains mostly fine grained massive magnetite and needles of actinolite.

Figure 13.9 Sample piece KUJ9-123.

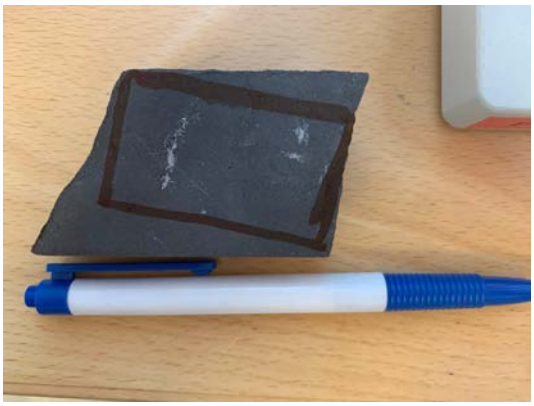

Figure 13.10 Sample piece KUJ10-123.

KUJ10-123 can be seen in figure 13.10. The sample was taken at 148.08 m very close to HW/ ore contact of KUJ-87123. It is dark grey in colour, shows a few white spots and consists of dark grey, fine grained massive magnetite and some whitish apatite sprinkles.

Figure 13.11 Sample piece KUJ11-123.

Figure 13.12 Sample piece KUJ12-123.

KUJ11-123 is illustrated is figure 13.11. It was taken at 145.85 m in the HW of KUJ-87123. The sample is fine grained, dark grey and party greenish/ reddish in colour. It contains a magnetite patch, K-feldspar sprinkles, biotite, actinolite and apatite.

KUJ12-123, shown in figure 13.12, was taken at 242.09 m at FW/ ore contact of KUJ-87123. The sample is fine grained, dark grey and composed of massive magnetite apatite and biotite.

Figure 13.13 Sample piece KUJ13-87123.

Figure 13.14 Sample piece KUJ14-221.

KUJ13-123 is shown in figure 13.13. The sample was taken at 259.99 m in the FW of drillcore KUJ-87123. The sample is fine grained and irregular in colour with dark grey to medium grey and beige spots. It contains disseminated magnetite, such as titanite, K-feldspar and actinolite.

KUJ14-221 can be seen in figure 13.14 and was taken at 209.15 m at HW/ ore contact of core KUJ-87221. The sample contains magnetite veining, K-feldspar, apatite and biotite and is therefore variable in colour from dark grey to greenish and reddish. The minerals are fine grained, only the K-feldspar shows some coarser grained crystals.

Figure 13.15 Sample piece KUJ15-221.

Figure 13.16 Sample piece KUJ16-221.

KUJ15-221, presented in figure 13.15 and was taken at 220 m in the ore zone of drillcore KUJ-87221. The sample piece is dark grey in colour, fine grained and contains massive magnetite with some randomly oriented actinolite.

KUJ16-221, which is shown in figure 13.16, was taken at 324.72 m in the ore zone, close to FW contact of drillcore KUJ-87221. The sample is fine grained and dark grey in colour with green spots. It contains massive magnetite and spots of actinolite.

KUJ17-221 can be seen in figure 13.17. The sample piece was taken at 317.45 m at FW/ore contact of drillcore KUJ-87221. Its fine grained and dark grey in colour. Its composed of massive magnetite, randomly oriented actinolite and some sprinkels of apatite.

Figure 13.17 Sample piece KUJ17-221.

Figure 13.18 Sample piece KUJ18-221.

KUJ18-221, presented in figure 13.18 was taken 439.50 m in the FW of drillcore KUJ-87221. The sample piece has a fine grain size and a flow texture of mainly dark grey magnetite and reddish K-feldspar with spots of grey apatite.

KUJ19-221 is shown in figure 13.19. The sample was taken at 426.70 m in the FW of drillcore KUJ-87221. This core has besides the main ore zone, a small ore zone within the FW. The sample was taken above the small ore zone. The sample is fine grained with a dark grey colour and consists of massive magnetite and patches of green actinolite.

KUJ20-114 can be seen figure 13.20 and was taken at 199.34 m in the ore zone of drillcore KUJ-87114. Since the HW of this core was missing in the archives no HW sample could be taken. The sample consists of dark grey and finely grained massive magnetite, some randomly oriented, needle like, green actinolite and fine white lines of apatite.

Figure 13.19 Sample piece KUJ19-221.

Figure 13.20 Sample piece KUJ20-114.

KUJ21-114 is shown in figure 13.21. The sample piece was take in the ore zone of drillcore KUJ-87114 at 294.53 m. It is composed of fine grained, massive, dark grey magnetite and fine schlieren of white apatite.

KUJ22-114 is shown in figure 13.22 was taken in the FW of drillcore KUJ-87114 at 294.53 m. The sample consists of a dark grey and fine grained magnetite patch such as K-feldspar, biotite and apatite.

Figure 13.21 Sample piece KUJ21-114.

Figure 13.22 Sample piece KUJ22-114.

PG23-156 was taken at 260.03 m in the ore zone close to the HW contact of PG-81156 and can be seen in figure 13.23. The sample piece consists of massive, fine to medium grained hematite and two layers of reddish apatite.

PG24-156, shown in figure 13.24, was taken at 292.08 m in the ore zone of core PG-81156. The sample piece is composed of fine to medium grained hematite and some patches of red apatite and white calcite.

Figure 13.23 Sample piece PG23-156.

Figure 13.24 Sample piece PG24-156.

PG25-156 is shown in figure 13.25 and was taken at 297.45 m within the ore zone of drillcore PG81156. The sample piece is composed of veined magnetite and clasts of red apatite. The apatite clasts contain disseminated magnetite and some drop like white calcite.

Figure 13.25 Sample piece PG25-156.

Figure 13.26 Sample piece PG26-156.

PG26-156 can be seen in figure 13.26 and was taken at 331.85 m within the ore zone of drillcore PG-81156. The sample contains massive magnetite, veins of reddish apatite and disseminated actinolite and biotite.

PG27-165 was taken at 309.59 m within the ore zone of drillcore PG-81165 an is shown in figure 13.27. The sample contains massive magnetite and hematite in patches such as fine veins of apatite and K-feldspar.

Figure 13.27 Sample piece PG27-81165.

Figure 13.28 Sample piece PG28-81165.

PG28-165, shown in figure 13.28, was taken at 314.50 m within the ore zone of drillcore PG-81165. The sample is mainly composed of massive magnetite and hematite with fine veining of white/ reddish apatite.

PG29-165 is shown in figure 13.29 and was taken in the FW of drillcore PG-81165 close to the ore contact. The contact ore zone/ FW is heavily altered. The sample piece contains disseminated magnetite and limonite.

PG30-617 was taken in the ore zone at 913.40 m of drillcore PG-81617. The sample is

shown in figure 13.30 and contains irregular iron oxide fragments in a magnetite and hematite matrix with whitish (calcite) to brick-red (apatite) fillings.

Figure 13.29 Sample piece PG29-165.

Figure 13.30 Sample piece PG30-617.

PG31-617 is shown in figure 13.31 and was taken within the ore zone at 926.10 m of core PG-81617. The sample piece is mainly composed of a dark grey magnetite and hematite groundmass with irregular light grey iron oxide fragments and whitish-blueish phenocrysts (feldspar) and whitish-greenish schlieren of mainly quartz, apatite and chlorite.

Figure 13.31 Sample piece PG31-617.

Figure 13.32 Sample piece PG32-617.

PG32-167 was taken at 1093.96 m within the ore zone of drillcore PG-81617 and is shown in figure 13.32. The sample contains massive magentite, which is layered at the right side and without textural orientation on the left side of the sample. The blueish-greyish phenocrysts are mainly composed of quartz and some biotite.

Figure 13.33 shows sample PG33-165, which was taken at 187.60 m within the ore zone of drillcore PG81163. The sample consists of massive, fine grained, dark grey hematite, which is irregularly layered with whitish apatite.

Figure 13.33 Sample piece PG33-163.

Figure 13.34 Sample piece PG34-163.

Sample PG34-163 was taken at 189.90 m in the ore zone of drillcore PG81163 and can be seen in figure 13.34. The sample consists of hematite with clasts of red feldspar and apatite such as white calcite fillings.

13.2 Thin sections

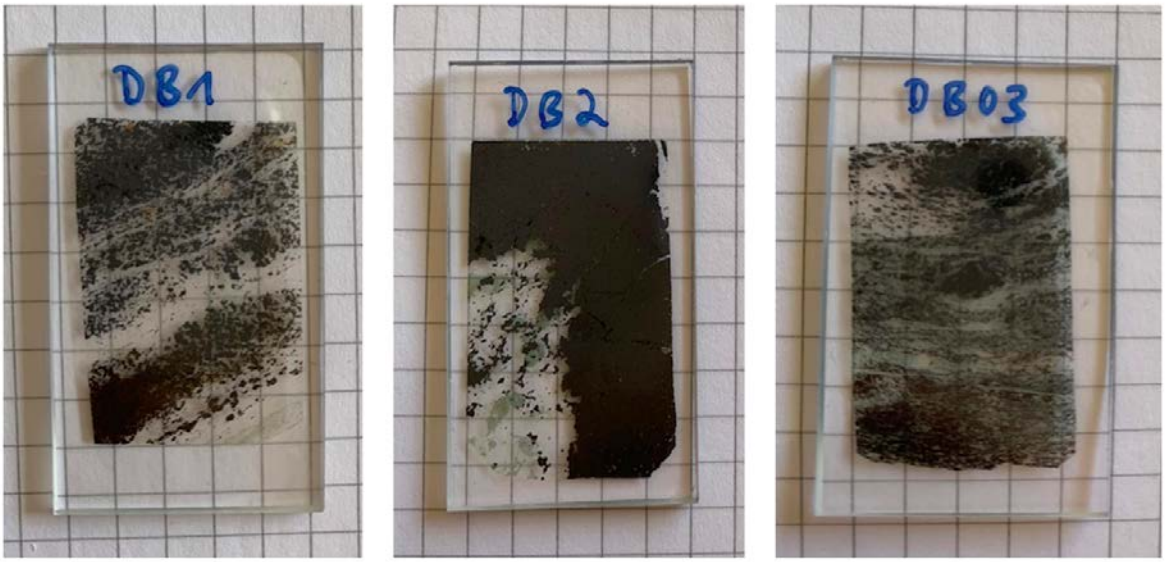

Figure 13.35 Thin sections KUJ1-KUJ3.

Figure 13.36 Thin sections KUJ4-KUJ6.

Figure 13.37 Thin sections KUJ7-KUJ9.

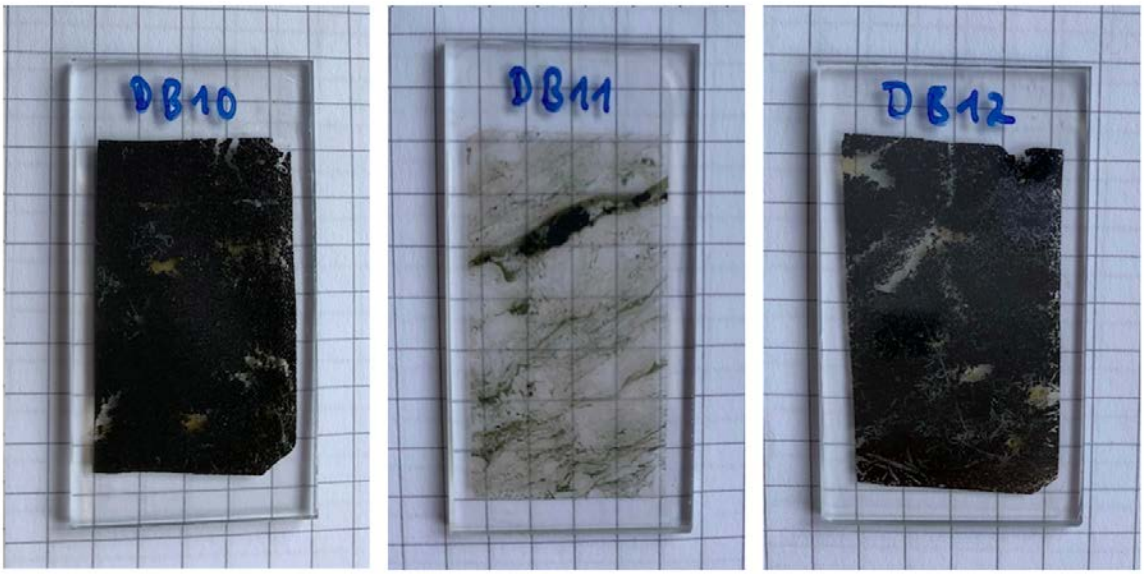

Figure 13.38 Thin sections KUJ10-KUJ12.

Figure 13.39 Thin sections KUJ13-KUJ15.

Figure 13.40 Thin sections KUJ16-KUJ18.

Figure 13.41 Thin sections KUJ19-KUJ21.

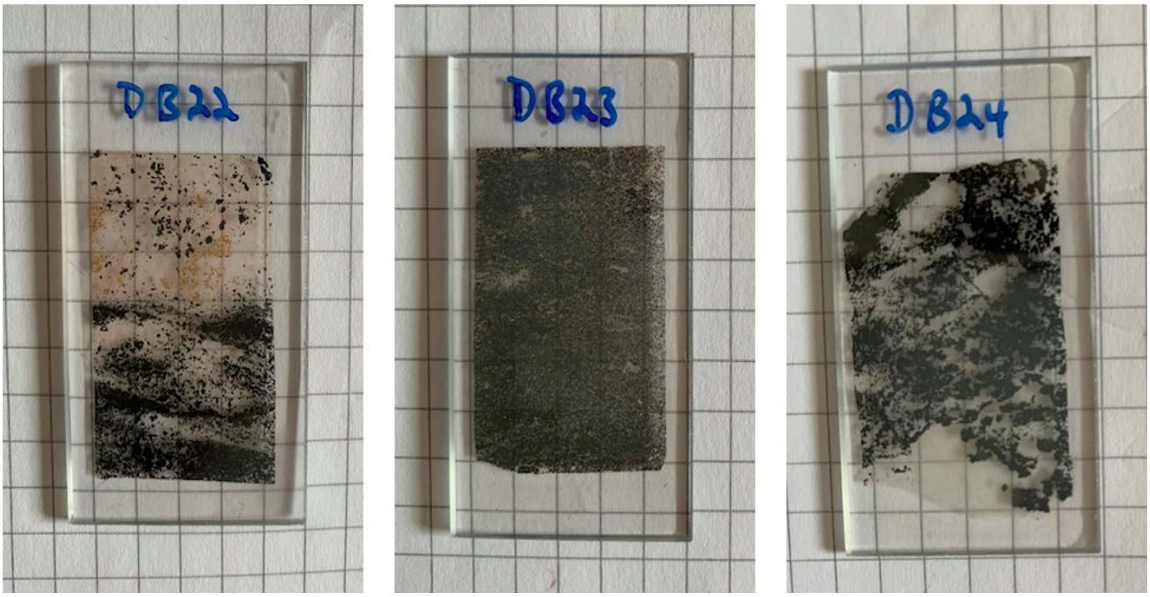

Figure 13.42 Thin sections KUJ22-PG24.

Figure 13.43 Thin sections PG25-PG27.

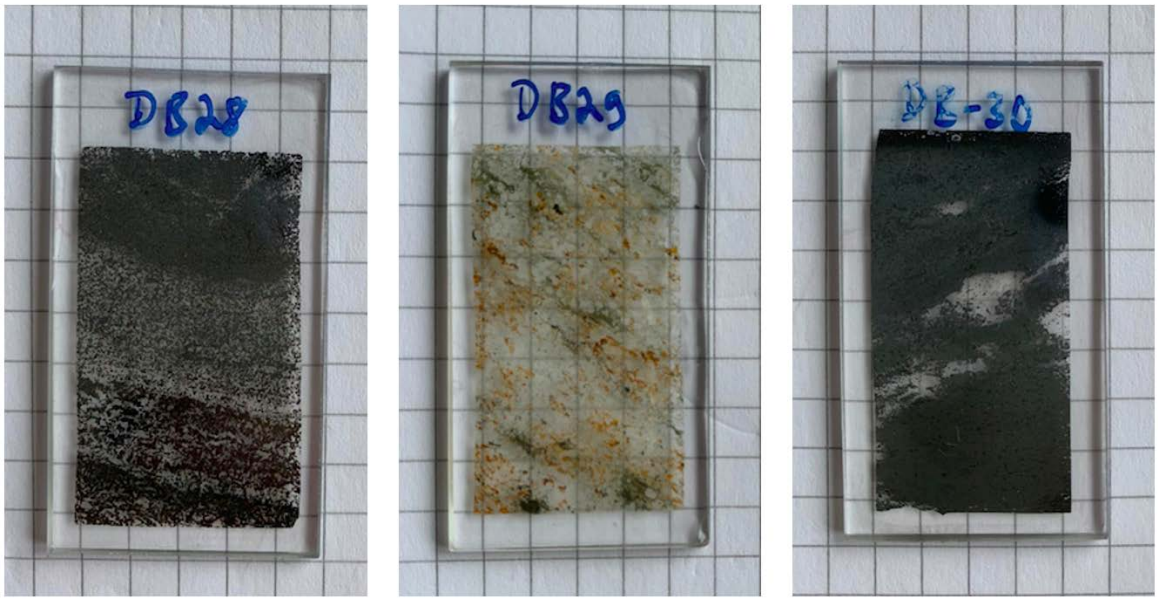

Figure 13.44 Thin sections PG28-PG617.

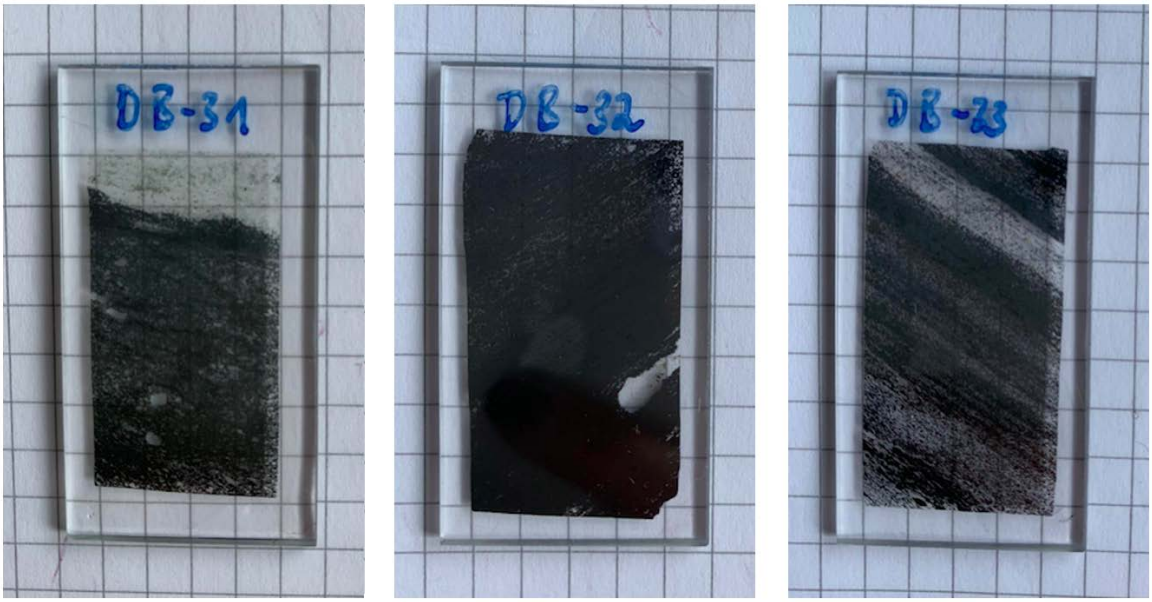

Figure 13.45 Thin sections PG31-PG33.

Figure 13.46 Thin sections PG34.

13.3 Electron probe microanalysis (EMPA)

Table 13.1 Apatite composition determined by EMPA for Kiirunavaara samples.

Sample	Crystal	Pos.	As_2O_5	F	P_2O_5	CaO	Ce_2O_3	ZrO_2	Cl	La_2O_3	Total
KUJ1	0101	Core	B.D.L.	4.209	42.200	56.301	B.D.L	B.D.L	0.118	B.D.L	101.09
KUJ1	0101	Rim	B.D.L	3.883	41.968	56.352	0.121	0.103	0.120	0.059	100.96
KUJ1	0101	Rim	B.D.L	3.753	41.304	54.673	B.D.L	0.116	0.099	B.D.L	98.37
KUJ1	0102	Core	B.D.L	3.766	42.796	56.428	B.D.L	0.120	0.103	B.D.L	101.62
KUJ1	0102	Rim	B.D.L	3.753	42.797	56.456	B.D.L	0.095	0.134	B.D.L	101.68
KUJ1	0102	Rim	B.D.L	3.568	41.361	55.009	0.238	0.107	0.136	0.190	99.08
KUJ1	0103	Core	B.D.L	3.546	40.882	55.334	0.253	0.173	0.155	0.074	98.889
KUJ1	0103	Rim	B.D.L	3.802	42.150	55.836	B.D.L	0.138	0.106	B.D.L	100.46
KUJ1	0103	Rim	B.D.L	3.786	42.799	55.711	0.241	0.066	0.162	B.D.L	101.18
KUJ1	0104	Rim	B.D.L	3.847	41.677	55.824	0.051	0.079	0.116	B.D.L	99.98
KUJ1	0104	Core	B.D.L	3.936	40.362	55.262	0.506	0.050	0.148	0.163	98.77
KUJ1	0104	Core	B.D.L	3.966	41.855	55.948	B.D.L	B.D.L	0.116	B.D.L	100.28
KUJ1	0104	Rim	B.D.L	3.800	41.568	55.990	B.D.L	0.104	0.078	B.D.L	99.94
KUJ1	0105	Rim	B.D.L	3.599	41.591	56.455	B.D.L	0.123	0.083	B.D.L	100.34
KUJ1	0105	Core	B.D.L	3.936	41.202	55.779	B.D.L	0.127	0.090	B.D.L	99.49
KUJ1	0105	Rim	B.D.L	3.606	41.449	56.288	B.D.L	0.096	0.130	B.D.L	100.06
KUJ1	0106	Rim	B.D.L	3.599	42.021	56.077	B.D.L	0.059	0.111	B.D.L	100.35
KUJ1	0106	Core	B.D.L	3.923	41.701	56.254	B.D.L	0.066	0.092	B.D.L	100.39
KUJ13	1307	Rim	0.058	4.372	41.617	55.902	B.D.L	0.118	0.029	B.D.L	100.25
KUJ13	1307	Core	B.D.L	4.437	41.038	56.001	B.D.L	0.118	B.D.L	B.D.L	99.78
KUJ13	1307	Core	B.D.L	3.746	41.114	56.111	0.067	0.128	B.D.L	B.D.L	99.62
KUJ17	1708	Core	B.D.L	3.855	40.677	54.361	0.528	0.111	0.108	0.126	98.12
KUJ17	1708	Rim	B.D.L	3.847	41.421	55.711	0.078	0.077	0.087	B.D.L	99.65
KUJ17	1708	Core	B.D.L	3.499	41.023	55.243	0.301	0.067	0.081	0.074	98.8
KUJ17	1709	Core	B.D.L	4.098	41.709	56.346	0.058	0.092	0.069	0.076	100.73
KUJ17	1709	Rim	B.D.L	3.926	41.610	55.668	0.177	0.052	0.071	B.D.L	99.85
KUJ17	1709	Core	B.D.L	4.064	41.329	55.757	0.085	0.175	0.046	B.D.L	99.75
KUJ17	1709	Rim	B.D.L	3.522	41.633	56.051	0.044	0.103	0.078	B.D.L	99.93
KUJ17	1710	Rim	0.060	3.703	41.329	56.001	0.044	0.148	0.062	B.D.L	99.77
KUJ17	1710	Rim	B.D.L	3.601	41.275	55.608	0.045	0.177	0.093	B.D.L	99.29
KUJ17	1710	Rim	B.D.L	3.881	41.290	55.513	0.047	0.108	0.081	B.D.L	99.31
KUJ17	1710	Core	B.D.L	3.846	40.359	54.649	0.484	0.128	0.113	0.126	98.09
KUJ17	1711	Core	B.D.L	4.084	41.456	55.245	0.161	0.099	0.099	B.D.L	99.45
KUJ17	1711	Rim	B.D.L	3.790	41.119	55.345	0.337	0.116	0.103	0.152	99.34
KUJ17	1711	Rim	B.D.L	3.592	41.090	55.332	0.408	0.132	0.096	0.144	99.26
KUJ17	1711	Rim	B.D.L	3.450	40.314	53.960	0.304	0.082	0.087	0.080	96.82
KUJ17	1712	Core	B.D.L	4.238	41.602	56.084	0.069	0.130	0.080	B.D.L	100.40
KUJ17	1712	Core	B.D.L	3.951	40.840	54.881	0.063	0.092	0.070	0.007	98.22
KUJ17	1712	Rim	B.D.L	3.683	40.488	55.331	0.112	0.167	0.093	0.046	98.35
KUJ4	0413	Core	B.D.L	4.145	40.985	55.130	0.694	0.092	B.D.L	0.338	99.65
KUJ4	0413	Rim	B.D.L	4.237	40.536	55.442	0.643	0.096	B.D.L	0.381	99.59
KUJ4	0413	Rim	B.D.L	4.496	41.115	55.316	0.509	0.095	B.D.L	0.232	99.89
KUJ19	1915	Rim	B.D.L	3.288	42.047	55.688	0.038	0.160	0.044	B.D.L	99.87
KUJ19	1915	Core	B.D.L	3.659	41.515	55.263	0.354	0.079	0.084	0.161	99.55
KUJ19	1916	Core	B.D.L	3.819	42.677	56.833	B.D.L	0.115	0.046	B.D.L	101.881
KUJ19	1916	Rim	B.D.L	3.820	42.092	55.968	0.326	0.129	0.071	0.133	100.93
KUJ19	1917	Core	B.D.L	3.850	41.836	56.129	0.278	B.D.L	0.070	0.131	100.71
KUJ19	1917	Rim	B.D.L	3.659	42.179	55.300	0.200	0.093	0.073	0.116	100.06
KUJ19	1918	Core	B.D.L	3.972	42.026	56.414	0.204	0.098	0.056	B.D.L	101.16
KUJ19	1918	Rim	B.D.L	3.821	41.456	55.514	0.436	0.060	0.088	0.150	99.89
KUJ19	1918	Rim	B.D.L	3.887	41.480	55.491	0.367	0.080	0.067	0.159	99.88

Table 13.2 Apatite composition determined by EMPA for Per Geijer samples.

Sample	Crystal	Pos.	As_2O_5	F	P_2O_5	CaO	Ce_2O_3	ZrO_2	Cl	La_2O_3	Total
PG28	2819	Rim	B.D.L	3.488	41.684	56.420	B.D.L	0.094	B.D.L	B.D.L	100.27
PG28	2819	Core	B.D.L	4.120	41.875	55.937	0.311	0.104	0.032	0.13	100.789
PG28	2820	Core	B.D.L	4.401	42.148	56.089	0.264	0.092	B.D.L	0.062	101.24
PG28	2820	Rim	B.D.L	4.024	42.423	56.842	B.D.L	B.D.L	B.D.L	B.D.L	101.697
PG28	2821	Rim	B.D.L	3.820	42.204	56.946	0.037	0.123	B.D.L	B.D.L	101.56
PG28	2821	Core	B.D.L	3.966	42.340	56.583	0.043	0.051	B.D.L	0.051	101.41
PG28	2821	Core	0.059	3.992	42.681	55.603	0.116	0.103	B.D.L	B.D.L	100.9
PG28	2822	Rim	B.D.L	4.087	41.829	56.149	0.056	0.122	B.D.L	B.D.L	100.53
PG28	2822	Core	B.D.L	4.273	42.542	56.706	B.D.L	0.099	B.D.L	B.D.L	101.86
PG28	2822	Rim	B.D.L	4.314	41.823	56.123	B.D.L	0.107	B.D.L	B.D.L	100.6
PG28	2823	Core	B.D.L	4.151	41.090	55.799	0.230	0.174	0.032	0.105	99.84
PG28	2823	Rim	B.D.L	4.085	41.480	55.509	0.337	0.135	0.032	0.142	100.01
PG28	2824	Core	B.D.L	4.280	42.328	56.510	B.D.L	0.121	B.D.L	B.D.L	101.517
PG28	2824	Core	B.D.L	4.633	41.734	56.251	0.057	0.076	B.D.L	B.D.L	100.82
PG28	2824	Rim	B.D.L	4.271	42.190	56.072	0.057	0.129	B.D.L	B.D.L	100.94
PG28	2824	Core	B.D.L	4.173	40.932	55.286	0.334	0.127	B.D.L	0.099	99.21
PG28	2825	Core	B.D.L	3.442	41.786	55.462	0.431	0.106	0.032	0.180	99.98
PG28	2825	Rim	B.D.L	4.230	42.578	56.184	0.217	0.149	0.029	0.136	101.753
PG28	2825	Rim	B.D.L	4.079	42.640	56.540	0.113	0.159	B.D.L	B.D.L	101.7
PG33	3326	Core	B.D.L	4.230	42.637	56.652	0.075	0.090	B.D.L	B.D.L	101.97
PG33	3326	Rim	B.D.L	4.482	42.333	56.391	0.047	0.130	0.028	B.D.L	101.55
PG33	3327	Rim	B.D.L	4.269	41.019	56.093	0.047	0.075	B.D.L	B.D.L	99.75
PG33	3327	Core	B.D.L	4.303	41.803	56.535	0.047	0.147	0.032	B.D.L	101.067
PG33	3327	Rim	B.D.L	4.038	41.209	56.203	0.072	0.133	B.D.L	B.D.L	100.01
PG33	3328	Core	B.D.L	4.295	42.273	55.952	0.202	0.159	0.030	B.D.L	101.12
PG33	3329	Core	B.D.L	4.103	41.531	55.565	0.355	0.113	0.038	0.120	100.08
PG33	3330	Core	B.D.L	4.458	41.885	56.621	0.048	0.137	B.D.L	B.D.L	101.28
PG33	3330	Rim	B.D.L	4.253	41.441	55.159	0.032	0.094	B.D.L	B.D.L	99.24
PG33	3331	Core	B.D.L	3.829	41.975	55.580	0.131	0.125	B.D.L	0.063	100.11
PG33	3331	Rim	0.067	4.643	41.349	55.723	0.071	B.D.L	B.D.L	B.D.L	99.99
PG33	3332	Core	B.D.L	4.325	41.574	55.099	0.040	0.094	B.D.L	B.D.L	99.38
PG26	2633	Core	B.D.L	4.027	42.262	55.020	0.328	0.096	0.092	0.055	100.21
PG26	2634	Rim	B.D.L	4.167	41.269	55.285	0.349	0.096	0.096	0.111	99.59
PG26	2634	Rim	B.D.L	4.275	41.645	55.222	0.334	0.118	0.057	0.097	99.93
PG26	2635	Rim	B.D.L	4.112	41.873	55.352	0.362	0.164	0.074	0.068	100.30
PG26	2635	Core	B.D.L	4.458	43.025	56.036	B.D.L	0.119	0.057	B.D.L	101.81
PG26	2635	Rim	0.060	4.175	41.276	55.468	0.313	0.122	0.070	0.140	99.85
PG26	2636	Core	B.D.L	4.077	41.631	55.971	0.236	0.078	0.078	0.060	100.41
PG26	2636	Rim	B.D.L	3.889	41.134	54.998	0.397	0.079	0.094	0.111	99.06
PG26	2636	Rim	0.057	4.173	41.047	55.073	0.538	0.119	0.088	0.168	99.48
PG26	2637	Core	B.D.L	4.168	41.491	55.349	0.313	0.110	0.090	0.106	99.87
PG26	2637	Rim	B.D.L	4.166	41.394	55.795	0.385	0.123	0.098	0.056	100.24
PG26	2637	Rim	B.D.L	4.266	42.008	55.432	0.336	0.052	0.091	0.118	100.48
PG26	2638	Core	B.D.L	3.815	41.495	55.490	0.325	0.104	0.105	0.081	99.78
PG26	2638	Core	B.D.L	4.044	41.972	55.183	0.444	0.066	0.090	0.139	100.25
PG26	2638	Rim	B.D.L	3.894	42.017	55.476	0.430	B.D.L	0.096	0.256	100.53
PG26	2638	Rim	B.D.L	4.106	42.293	55.238	0.320	0.098	0.103	0.143	100.55
PG26	2639	Core	B.D.L	4.201	42.880	55.217	0.250	0.161	0.071	0.090	101.10
PG26	2640	Rim	0.051	4.511	42.700	55.979	0.170	0.137	0.045	0.071	101.75
PG26	2641	Core	B.D.L	3.985	41.118	55.304	0.393	0.132	0.081	0.126	99.44
PG26	2641	Rim	B.D.L	3.994	40.903	55.412	0.499	0.058	0.106	0.096	99.36
PG31	3142	Core	B.D.L	3.688	42.047	56.126	B.D.L	0.099	0.166	B.D.L	100.56
PG31	3143	Core	B.D.L	3.303	42.775	56.313	B.D.L	0.190	0.184	B.D.L	101.39
PG31	3143	Core	B.D.L	3.587	42.184	56.471	B.D.L	0.139	0.155	B.D.L	101
PG31	3143	Rim	B.D.L	3.366	42.725	55.674	B.D.L	0.117	0.167	B.D.L	100.62
PG31	3143	Rim	B.D.L	3.386	42.998	56.157	0.049	0.131	0.160	B.D.L	101.44
PG31	3144	Core	B.D.L	3.851	42.954	56.339	B.D.L	0.164	0.167	B.D.L	101.88
PG31	3144	Rim	B.D.L	3.562	42.183	55.883	B.D.L	0.087	0.169	B.D.L	100.37
PG31	3145	Core	B.D.L	3.874	41.989	56.497	B.D.L	0.142	0.187	B.D.L	101.01
PG31	3145	Rim	B.D.L	3.988	42.124	56.414	0.064	B.D.L	0.187	B.D.L	101.09

Table 13.3 Magnetite composition determined by EMPA for Kiirunavaara samples.

S. Nr.	Crystal	Pos.	MgO	SnO_2	Y_2O_3	CaO	Fe_2O_3	Al_2O_3	V_2O_3	Nb_2O_5	TiO_2	NiO	SiO_2	MoO_3	CoO	WO_3	MnO	Cr_2O_3	Tot.
KUJ1	0101	Core	B.D.L	B.D.L	B.D.L	B.D.L	102.17	B.D.L	0.112	B.D.L	B.D.L	B.D.L	0.050	B.D.L	0.177	B.D.L	B.D.L	B.D.L	102.70
KUJ1	0101	Rim	B.D.L	B.D.L	B.D.L	B.D.L	102.30	B.D.L	0.134	B.D.L	B.D.L	B.D.L	0.011	B.D.L	0.206	B.D.L	B.D.L	B.D.L	102.78
KUJ1	0101	Rim	0.033	B.D.L	B.D.L	B.D.L	102.57	B.D.L	0.105	B.D.L	B.D.L	B.D.L	B.D.L	B.D.L	0.199	B.D.L	B.D.L	B.D.L	103.03
KUJ1	0102	Core	B.D.L	B.D.L	B.D.L	B.D.L	102.13	B.D.L	0.127	B.D.L	B.D.L	B.D.L	B.D.L	B.D.L	0.205	B.D.L	B.D.L	B.D.L	102.58
KUJ1	0102	Rim	B.D.L	B.D.L	B.D.L	B.D.L	102.79	B.D.L	0.095	B.D.L	B.D.L	B.D.L	0.027	B.D.L	0.207	B.D.L	B.D.L	B.D.L	103.25
KUJ1	0103	Core	B.D.L	B.D.L	B.D.L	B.D.L	102.04	B.D.L	0.088	B.D.L	B.D.L	B.D.L	0.039	B.D.L	0.200	B.D.L	B.D.L	B.D.L	102.52
KUJ1	0104	Core	0.037	B.D.L	B.D.L	B.D.L	102.42	B.D.L	0.126	B.D.L	B.D.L	B.D.L	0.046	B.D.L	0.212	B.D.L	B.D.L	B.D.L	103.05
KUJ1	0105	Core	B.D.L	B.D.L	B.D.L	B.D.L	101.97	B.D.L	0.084	B.D.L	B.D.L	B.D.L	0.021	B.D.L	0.187	B.D.L	B.D.L	B.D.L	102.39
KUJ1	0105	Rim	B.D.L	B.D.L	B.D.L	B.D.L	102.06	B.D.L	0.090	B.D.L	B.D.L	B.D.L	B.D.L	B.D.L	0.193	B.D.L	B.D.L	B.D.L	102.45
KUJ1	0106	Core	B.D.L	B.D.L	B.D.L	B.D.L	102.59	B.D.L	0.111	B.D.L	B.D.L	B.D.L	0.013	B.D.L	0.198	B.D.L	B.D.L	B.D.L	103.03
KUJ1	0106	Rim	B.D.L	B.D.L	B.D.L	B.D.L	102.78	B.D.L	0.114	B.D.L	B.D.L	B.D.L	0.047	B.D.L	0.203	B.D.L	B.D.L	B.D.L	103.34
KUJ1	0107	Rim	B.D.L	B.D.L	B.D.L	B.D.L	102.39	B.D.L	0.113	B.D.L	B.D.L	B.D.L	0.038	B.D.L	0.204	B.D.L	0.078	B.D.L	102.96
KUJ1	0107	Rim	B.D.L	B.D.L	B.D.L	B.D.L	102.27	B.D.L	0.102	B.D.L	B.D.L	B.D.L	0.030	B.D.L	0.200	B.D.L	B.D.L	B.D.L	102.8
KUJ13	1308	Core	0.029	B.D.L	B.D.L	B.D.L	101.98	B.D.L	0.155	B.D.L	B.D.L	B.D.L	0.023	B.D.L	0.201	B.D.L	B.D.L	B.D.L	102.51
KUJ13	1308	Rim	0.057	B.D.L	B.D.L	B.D.L	101.53	B.D.L	0.140	B.D.L	B.D.L	B.D.L	0.046	B.D.L	0.214	B.D.L	B.D.L	B.D.L	102.10
KUJ13	1309	Rim	B.D.L	B.D.L	B.D.L	B.D.L	101.68	B.D.L	0.156	B.D.L	B.D.L	B.D.L	0.029	B.D.L	0.184	B.D.L	B.D.L	B.D.L	102.17
KUJ13	1309	Core	0.044	B.D.L	B.D.L	B.D.L	101.81	B.D.L	0.147	B.D.L	B.D.L	B.D.L	0.036	B.D.L	0.191	B.D.L	B.D.L	B.D.L	102.43
KUJ13	1310	Rim	0.061	B.D.L	B.D.L	B.D.L	101.69	B.D.L	0.158	B.D.L	B.D.L	B.D.L	0.026	B.D.L	0.188	B.D.L	B.D.L	B.D.L	102.30
KUJ13	1311	Core	0.032	B.D.L	B.D.L	B.D.L	102.09	B.D.L	0.155	B.D.L	B.D.L	B.D.L	0.016	B.D.L	0.185	B.D.L	B.D.L	B.D.L	102.60
KUJ13	1311	Rim	0.042	B.D.L	B.D.L	B.D.L	102.07	B.D.L	0.170	B.D.L	B.D.L	B.D.L	0.038	B.D.L	0.195	B.D.L	B.D.L	B.D.L	102.7
KUJ13	1311	Rim	B.D.L	B.D.L	B.D.L	B.D.L	102.15	B.D.L	0.175	B.D.L	B.D.L	B.D.L	0.044	B.D.L	0.195	B.D.L	0.078	B.D.L	102.76
KUJ13	1311	Rim	0.043	B.D.L	B.D.L	B.D.L	102.02	B.D.L	0.163	B.D.L	B.D.L	B.D.L	0.018	B.D.L	0.213	B.D.L	0.081	B.D.L	102.61
KUJ13	1312	Core	B.D.L	B.D.L	B.D.L	B.D.L	101.83	B.D.L	0.142	B.D.L	B.D.L	B.D.L	0.013	B.D.L	0.187	B.D.L	B.D.L	B.D.L	102.32
KUJ13	1312	Rim	0.031	B.D.L	B.D.L	B.D.L	102.58	B.D.L	0.154	B.D.L	B.D.L	B.D.L	0.021	B.D.L	0.183	B.D.L	B.D.L	B.D.L	103.18
KUJ13	1313	Core	0.075	B.D.L	B.D.L	B.D.L	101.48	B.D.L	0.130	B.D.L	B.D.L	B.D.L	0.128	B.D.L	0.188	B.D.L	B.D.L	B.D.L	102.21
KUJ13	1313	Core	0.076	B.D.L	B.D.L	B.D.L	101.35	B.D.L	0.137	B.D.L	B.D.L	B.D.L	0.130	B.D.L	0.192	B.D.L	B.D.L	B.D.L	101.96
KUJ13	1314	Core	0.035	B.D.L	B.D.L	B.D.L	102.06	B.D.L	0.160	B.D.L	B.D.L	B.D.L	0.018	B.D.L	0.180	B.D.L	B.D.L	B.D.L	102.60
KUJ13	1314	Rim	0.058	B.D.L	B.D.L	B.D.L	102.51	B.D.L	0.154	B.D.L	B.D.L	B.D.L	0.069	B.D.L	0.204	B.D.L	B.D.L	B.D.L	103.12
KUJ17	1715	Core	B.D.L	B.D.L	B.D.L	0.065	102.2	B.D.L	0.084	B.D.L	B.D.L	B.D.L	0.056	B.D.L	0.179	B.D.L	0.079	B.D.L	102.76
KUJ17	1715	Rim	0.037	B.D.L	B.D.L	0.076	102.23	B.D.L	0.080	B.D.L	B.D.L	B.D.L	0.100	B.D.L	0.199	B.D.L	0.101	B.D.L	102.93
KUJ17	1716	Core	B.D.L	B.D.L	B.D.L	B.D.L	102.13	B.D.L	0.097	B.D.L	B.D.L	B.D.L	0.049	B.D.L	0.214	B.D.L	0.072	B.D.L	102.71
KUJ17	1716	Rim	0.050	B.D.L	B.D.L	B.D.L	102.21	B.D.L	0.085	B.D.L	B.D.L	B.D.L	0.033	B.D.L	0.238	B.D.L	B.D.L	B.D.L	102.71
KUJ17	1716	Rim	0.030	B.D.L	B.D.L	B.D.L	101.63	B.D.L	0.094	B.D.L	B.D.L	B.D.L	B.D.L	B.D.L	0.211	B.D.L	0.076	B.D.L	102.09
KUJ17	1717	Rim	0.037	B.D.L	B.D.L	B.D.L	102.51	B.D.L	0.100	B.D.L	B.D.L	B.D.L	B.D.L	B.D.L	0.200	B.D.L	B.D.L	B.D.L	102.97
KUJ17	1717	Rim	B.D.L	B.D.L	B.D.L	B.D.L	102.53	B.D.L	0.078	B.D.L	B.D.L	B.D.L	B.D.L	B.D.L	0.215	B.D.L	B.D.L	B.D.L	102.97
KUJ17	1718	Core	0.029	B.D.L	B.D.L	0.070	102.55	B.D.L	0.102	B.D.L	B.D.L	B.D.L	0.036	B.D.L	0.221	B.D.L	0.087	B.D.L	103.14
KUJ17	1718	Rim	0.038	B.D.L	B.D.L	B.D.L	102.75	B.D.L	0.083	B.D.L	B.D.L	B.D.L	0.028	B.D.L	0.194	B.D.L	B.D.L	B.D.L	103.19
KUJ17	1719	Rim	0.050	B.D.L	B.D.L	B.D.L	102.37	B.D.L	0.102	B.D.L	B.D.L	B.D.L	0.081	B.D.L	0.214	B.D.L	0.090	B.D.L	102.93
KUJ17	1719	Rim	0.078	B.D.L	B.D.L	B.D.L	101.68	B.D.L	0.090	B.D.L	B.D.L	B.D.L	0.116	B.D.L	0.213	B.D.L	B.D.L	B.D.L	102.36
KUJ17	1720	Core	B.D.L	B.D.L	B.D.L	B.D.L	102.62	B.D.L	0.111	B.D.L	B.D.L	B.D.L	0.019	B.D.L	0.205	B.D.L	B.D.L	B.D.L	103.11
KUJ17	1720	Rim	0.111	B.D.L	B.D.L	B.D.L	102.07	B.D.L	0.092	B.D.L	B.D.L	B.D.L	0.177	B.D.L	0.204	B.D.L	0.080	B.D.L	102.77
KUJ17	1720	Rim	0.031	B.D.L	B.D.L	B.D.L	102.38	B.D.L	0.109	B.D.L	B.D.L	B.D.L	0.017	B.D.L	0.198	B.D.L	0.069	B.D.L	102.92

Table 13.4 Magnetite composition determined by EMPA for Per Geijer samples.

S. Nr.	Crystal	Pos.	MgO	SnO_2	Y_2O_3	CaO	Fe_2O_3	Al_2O_3	V_2O_3	Nb2O5	TiO_2	NiO	SiO_2	MoO_3	CoO	WO_3	MnO	Cr_2O_3	[%]
PG28	2821	Core	0.036		B.D.L	B.D.L	102.64	B.D.L	0.067	B.D.L	B.D.L	B.D.L	0.162	B.D.L	0.223	B.D.L	B.D.L	B.D.L	103.26
PG28	2821	Rim	B.D.L	B.D.L	B.D.L	B.D.L	100.617	0.068	0.077	B.D.L	B.D.L	B.D.L	0.178	B.D.L	0.213	B.D.L	B.D.L	B.D.L	101.28
PG28	2821	Rim	0.034	B.D.L	B.D.L	B.D.L	102.026	B.D.L	0.070	B.D.L	B.D.L	B.D.L	B.D.L	B.D.L	0.244	B.D.L	B.D.L	B.D.L	102.50
PG28	2822	Core	B.D.L	B.D.L	B.D.L	B.D.L	102.116	B.D.L	0.073	B.D.L	B.D.L	B.D.L	0.083	B.D.L	0.215	B.D.L	B.D.L	B.D.L	102.57
PG28	2822	Rim	B.D.L	B.D.L	B.D.L	B.D.L	102.075	B.D.L	B.D.L	B.D.L	B.D.L	B.D.L	B.D.L	B.D.L	0.198	B.D.L	B.D.L	B.D.L	102.45
PG28	2823	Core	B.D.L	B.D.L	B.D.L	B.D.L	102.457	B.D.L	0.074	B.D.L	B.D.L	B.D.L	B.D.L	B.D.L	0.216	B.D.L	B.D.L	B.D.L	102.84
PG28	2823	Rim	B.D.L	B.D.L	B.D.L	B.D.L	101.993	B.D.L	0.078	B.D.L	B.D.L	B.D.L	B.D.L	B.D.L	0.213	B.D.L	B.D.L	B.D.L	102.38
PG26	2624	Core	B.D.L	B.D.L	B.D.L	B.D.L	102.536	B.D.L	0.104	B.D.L	0.007	B.D.L	B.D.L	B.D.L	0.211	B.D.L	B.D.L	B.D.L	102.97
PG26	2624	Rim	B.D.L	B.D.L	B.D.L	0.041	102.122	B.D.L	0.094	B.D.L	0.018	B.D.L	0.064	B.D.L	0.205	B.D.L	B.D.L	B.D.L	102.60
PG26	2625	Core	0.031	B.D.L	B.D.L	B.D.L	101.564	0.056	0.118	B.D.L	B.D.L	B.D.L	0.134	B.D.L	0.190	B.D.L	B.D.L	B.D.L	102.21
PG26	2625	Rim	B.D.L	B.D.L	B.D.L	0.022	101.636	B.D.L	0.122	B.D.L	B.D.L	B.D.L	B.D.L	B.D.L	0.217	B.D.L	B.D.L	B.D.L	102.11
PG26	2625	Rim	0.157	B.D.L	B.D.L	0.119	100.339	0.060	0.104	B.D.L	B.D.L	B.D.L	0.268	B.D.L	0.215	0.041	B.D.L	B.D.L	101.37
PG26	2626	Rim	B.D.L	B.D.L	B.D.L	0.054	102.127	B.D.L	0.106	B.D.L	0.023	B.D.L	0.099	B.D.L	0.201	B.D.L	B.D.L	B.D.L	102.72
PG26	2627	Core	B.D.L	B.D.L	B.D.L	0.067	102.287	B.D.L	0.095	B.D.L	B.D.L	B.D.L	B.D.L	B.D.L	0.193	B.D.L	B.D.L	B.D.L	102.76
PG26	2627	Rim	B.D.L	B.D.L	B.D.L	0.075	102.371	B.D.L	0.116	B.D.L	0.006	B.D.L	B.D.L	B.D.L	0.205	B.D.L	B.D.L	B.D.L	102.82
PG31	3128	Core	B.D.L	B.D.L	B.D.L	B.D.L	101.916	B.D.L	0.104	B.D.L	B.D.L	B.D.L	B.D.L	B.D.L	0.209	B.D.L	B.D.L	B.D.L	102.37
PG31	3129	Core	B.D.L	B.D.L	B.D.L	B.D.L	101.987	B.D.L	0.126	B.D.L	B.D.L	B.D.L	B.D.L	B.D.L	0.209	B.D.L	B.D.L	B.D.L	102.46
PG31	3130	Core	B.D.L	B.D.L	B.D.L	B.D.L	101.368	B.D.L	0.068	B.D.L	B.D.L	B.D.L	B.D.L	B.D.L	0.197	B.D.L	B.D.L	B.D.L	101.74
PG31	3130	Rim	B.D.L	B.D.L	B.D.L	B.D.L	102.363	B.D.L	0.100	B.D.L	B.D.L	B.D.L	B.D.L	B.D.L	0.200	B.D.L	B.D.L	B.D.L	102.79
PG31	3131	Core	B.D.L	B.D.L	B.D.L	B.D.L	100.784	B.D.L	0.082	B.D.L	B.D.L	B.D.L	B.D.L.	B.D.L	0.199	B.D.L	B.D.L	B.D.L	101.13

Table 13.5 Complete EMPA measuring conditions for apatite.

EOS Condition	CAL Elements Condition
Acc = 15.0 kV Probe Dia. = 15 um Probe Scan OFF	No. of Elements 1
Probe Current = Auto 1.542e-08 A	Elem- 1
Correction Condition	Elements O
Material : Oxide	Mode Anion
Correctoion Method : ZAF	Valence Condition
Elements Condition	WDS: 8: As(5) F(-1) P(5) Ca(2) Ce(3)
Total 9 Elements	Zr(4) Cl(-1) La(3)
WDS: 8: As F P Ca Ce Zr Cl La	CAL: 1: O(-2)
CAL: 1: O	Standard Condition
WDS Elements Condition	Elem- 1 Elem- 2 Elem- 3
No. of Elements 8	Elements As F P
Elem- 1 Elem- 2 Elem- 3 Elem- 4 Elem- 5	Signal WDS WDS WDS
Elements As F P Ca Ce	Name NiAsD15 Ap70D15 Ap70D15
Name As F2T P Ca4P Ce5L	Elem- 4 Elem- 5 Elem- 6
X-ray Name La Ka Ka Ka La	Elements Ca Ce Zr
Order 1 1 1 1 1	Signal WDS WDS WDS
Channel 1 2 3 4 5	Name Ap70D15 M108D15 Zirk149D15
Crystal TAP TAP PETJ PETJ LIFH	Elem- 7 Elem- 8
Spc.Pos.(mm) 105.147 199.284 197.156 107.500 178.241	Elements Cl La
Back(+) (mm) 5.800 3.800 4.000 4.500 2.494	Signal WDS WDS
Back(-) (mm) 5.500 3.000 4.000 4.500 2.700	Name Tug34DIA M108D15
Peak Seek W. 1 1 1 1 1	Printout Condition
Time/Count Time Time Time Time Time	No: Measurement Condition
Mes.Time(sec) 10.0 60.0 20.0 10.0 30.0	No: Pi Chart Output
Bac.Time(sec) 5.0 30.0 10.0 5.0 15.0	No: Bar Graph Output
Mes.Count 10000 10000 10000 10000 10000	No: Measurement Result
Bac.Count 500 500 500 500 500	No. of Oxygen : 26.00
PHA gain 16 32 128 64 32	Element Order
High V.(V) 1742 1716 1720 1736 1760	As[W] F [W] P [W] Ca[W] Ce[W]
Base L.(V) 2.00 0.70 2.00 0.70 2.00	Zr[W] Cl[W] La[W]
Window (V) 4.90 9.20 4.10 9.30 3.80	Additional Function
Diff/Int Diff Diff Diff Diff Diff	Peak Search : none
Sequence 1 1 1 1 1	Background Measurement : allways
Elem- 6 Elem- 7 Elem- 8	Asyncronous Measurement
Elements Zr Cl La	Crystal PETJ PETJ LIFH
Name Zr Cl La	Spc.Pos.(mm) 194.411 151.457 185.443
X-ray Name La Ka La	Back(+) (mm) 5.000 5.000 4.000
Order 1 1 1	Back(-) (mm) 3.800 5.500 4.500
Channel 3 4 5	Peak Seek W. 1 1 1
	Time/Count Time Time Time
	Mes.Time(sec) 30.0 30.0 30.0
	Bac.Time(sec) 15.0 15.0 15.0
	Mes.Count 10000 10000 10000
	Bac.Count 500 500 500
	PHA gain 128 64 32
	High V.(V) 1724 1724 1742
	Base L.(V) 2.00 0.70 2.00
	Window (V) 4.00 9.30 4.00
	Diff/Int Diff Diff Diff
	Sequence 2 2 2

Table 13.6 Complete measuring conditions for EMPA magnetite.

———————— EOS Condition ————————	———————— CAL Elements Condition ————————-
Acc = 20.0 kV Probe Dia. = 0 um Probe Scan OFF	No. of Elements 1
Probe Current = Auto 2.554e-08 A	Elem- 1
————————- Correction Condition ————————	Elements O
Material : Oxide	Mode Anion
Correctoion Method : ZAF	———————— Valence Condition ————————
———————— Elements Condition ————————	WDS: 16: Mg(2) Sn(4) Y(3) Ca(2) Fe(3)
Total 17 Elements	Al(3) V(3) Nb(5) Ti(4) Ni(2)
WDS: 16: Mg Sn Y Ca Fe Al V Nb Ti Ni	Si(4) Mo(6) Co(2) W(6) Mn(2)
Si Mo Co W Mn Cr	Cr(3)
CAL: 1: O	CAL: 1: O(-2)
———————— WDS Elements Condition ————————-	———————— Standard Condition ————————
No. of Elements 16	Elem- 1 Elem- 2 Elem- 3
Elem- 1 Elem- 2 Elem- 3 Elem- 4 Elem- 5	Elements Mg Sn Y
Elements Mg Sn Y Ca Fe	Signal WDS WDS WDS
Name Mg1T Sn Y Ca4P Fe5LH	Name Cr542 Sn88O Y
X-ray Name Ka La La Ka Ka	Elem- 4 Elem- 5 Elem- 6
Order 1 1 1 1 1	Elements Ca Fe Al
Channel 1 2 3 4 5	Signal WDS WDS WDS
Crystal TAP PETJ PETJ PETJ LIFH	Name Sche81 Mag53 Cr542
Spc.Pos.(mm) 107.498 115.036 206.497 107.510 134.975	Elem- 7 Elem- 8 Elem- 9
Back(+) (mm) 3.200 5.500 3.500 4.500 5.000	Elements V Nb Ti
Back(-) (mm) 2.900 5.300 3.500 4.500 4.500	Signal WDS WDS WDS
Peak Seek W. 1 1 1 1 1	Name V28O Nb150 Ru83
Time/Count Time Time Time Time Time	Elem- 10 Elem- 11 Elem- 12
Mes.Time(sec) 20.0 10.0 20.0 10.0 10.0	Elements Ni Si Mo
Bac.Time(sec) 10.0 5.0 10.0 5.0 5.0	Signal WDS WDS WDS
Mes.Count 10000 10000 10000 10000 10000	Name NiO148O Pl642T Mo16O
Bac.Count 500 500 500 500 500	Elem- 13 Elem- 14 Elem- 15
PHA gain 16 8 128 64 32	Elements Co W Mn
High V.(V) 1726 1714 1724 1736 1712	Signal WDS WDS WDS
Base L.(V) 0.70 2.00 2.50 0.70 0.70	Name Co125Co Sche81 Mn133
Window (V) 9.30 4.50 4.00 9.30 9.30	Elem- 16
Diff/Int Diff Diff Diff Diff Diff	Elements Cr
Sequence 1 1 1 1 1	Signal WDS
Elem- 6 Elem- 7 Elem- 8 Elem- 9 Elem- 10	Name Cr542
Elements Al V Nb Ti Ni	———————— Printout Condition ————————-
Name Al1T V2P Nb3P Ti4P Ni5LH	No: Measurement Condition
X-ray Name Ka Ka La Ka Ka	No: Pi Chart Output
Order 1 1 1 1 1	No: Bar Graph Output
Channel 1 2 3 4 5	No: Measurement Result
Crystal TAP PETJ PETJ PETJ LIFH	No. of Oxygen : 24.00
Spc.Pos.(mm) 90.578 79.863 183.330 87.911 115.739	Element Order
Back(+) (mm) 5.800 5.000 4.000 4.600 5.400	Mg[W] Sn[W] Y [W] Ca[W] Fe[W]
Back(-) (mm) 6.000 5.000 4.000 5.350 5.100	Al[W] V [W] Nb[W] Ti[W] Ni[W]
Peak Seek W. 1 1 1 1 1	Si[W] Mo[W] Co[W] W [W] Mn[W]
Time/Count Time Time Time Time Time	Cr[W]
Mes.Time(sec) 10.0 30.0 10.0 30.0 30.0	———————— Additional Function ————————
Bac.Time(sec) 5.0 15.0 5.0 15.0 15.0	Peak Search : none
Mes.Count 10000 10000 10000 10000 10000	Background Measurement : allways
Bac.Count 500 500 500 500 500	Asyncronous Measurement
PHA gain 16 8 128 64 32	Overlap correction
High V.(V) 1724 1710 1722 1678 1722	V - Ti 0.08254
Base L.(V) 0.70 2.50 2.00 2.00 2.00	Crystal TAP PETJ LIFH TAP LIFH
Window (V) 9.00 4.50 4.50 4.00 4.00	Spc.Pos.(mm) 77.329 173.206 124.811 75.790 146.448
Diff/Int Diff Diff Diff Diff Diff	Back(+) (mm) 1.800 5.000 5.500 5.000 4.000
Sequence 2 2 2 2 2	Back(-) (mm) 6.000 6.500 4.500 4.700 4.500
Elem- 11 Elem- 12 Elem- 13 Elem- 14 Elem- 15	Peak Seek W. 1 1 1 1 1
Elements Si Mo Co W Mn	Time/Count Time Time Time Time Time
Name Si1T Mo CoL5 W Mn5H2	Mes.Time(sec) 20.0 10.0 30.0 10.0 10.0
X-ray Name Ka La Ka Ma Ka	Bac.Time(sec) 10.0 5.0 15.0 5.0 5.0
Order 1 1 1 1 1	Mes.Count 10000 10000 10000 10000 10000
Channel 1 3 5 1 5	Bac.Count 500 500 500 500 500
	PHA gain 16 128 32 16 32
	High V.(V) 1710 1716 1726 1702 1706
	Base L.(V) 0.70 2.00 1.50 2.00 2.00
	Window (V) 9.30 4.00 5.00 4.50 5.00
	Diff/Int Diff Diff Diff Diff Diff
	Sequence 3 3 3 4 4
	Elem- 16
	Elements Cr
	Name Cr5LH
	X-ray Name Ka
	Order 1
	Channel 5
	Crystal LIFH
	Spc.Pos.(mm) 159.455
	Back(+) (mm) 6.000
	Back(-) (mm) 5.500
	Peak Seek W. 1
	Time/Count Time
	Mes.Time(sec) 20.0
	Bac.Time(sec) 10.0
	Mes.Count 10000
	Bac.Count 500
	PHA gain 32
	High V.(V) 1750
	Base L.(V) 2.50
	Window (V) 4.40
	Diff/Int Diff
	Sequence 5

13.4 Correlation Matrices

This section icludes correlation matrices for Kiirunavaara and Per Geijer. The matrices can as well be found on the CD that comes attached with this work.

	AG	Al	AS	BA	BE	BI	Ca	CD	CE	CO	CR	CS	CU	Fe	GA	HF	IN	K	LA	LI	LU	Mg	MN	MO
Ag	1.00	-0.13	-0.15	-0.04	-0.21	-0.28	0.15	0.13	-0.05	0.43	-0.02	-0.26	-0.05	0.07	-0.16	0.01	-0.06	0.00	-0.07	-0.42	-0.01	-0.18	0.34	-0,23
Al	-0.13	1.00	-0.14	0.64	0.75	0.12	0.44	0.76	0.32	-0.77	0.24	0.44	0.16	-0.97	0.14	0.90	0.40	0.82	0.46	0.51	0.29	0.48	-0.51	0,59
As	-0.15	-0.14	1.00	0.12	-0.05	0.37	0.43	-0.14	0.81	0.24	-0.29	0.10	0.35	0.05	-0.24	-0.14	-0.02	-0.07	0.69	-0.11	0.58	0.00	-0.06	-0,21
BA	-0.04	0.64	0.12	1.00	0.56	0.16	0.53	0.63	0.30	-0.57	-0.15	0.42	0.67	-0.69	0.00	0.72	0.40	0.82	0.36	0.30	0.37	0.41	-0.35	0,06
BE	-0.21	0.75	-0.05	0.56	1.00	0.53	0.37	0.49	0.22	-0.71	0.05	0.45	0.19	-0.77	0.29	0.74	0.78	0.61	0.36	0.41	0.46	0.66	-0.23	0,44
BI	-0.28	0.12	0.37	0.16	0.53	1.00	0.19	-0.07	0.30	-0.22	0.13	0.06	0.25	-0.12	-0.11	0.09	0.37	-0.02	0.23	-0.01	0.44	0.09	-0.04	0,22
CA	0.15	0.44	0.43	0.53	0.37	0.19	1.00	0.71	0.73	-0.23	-0.13	-0.10	0.26	-0.55	0.00	0.60	0.29	0.55	0.64	-0.19	0.68	0.19	-0.01	-0,06
CD	0.13	0.76	-0.14	0.63	0.49	-0.07	0.71	1.00	0.33	-0.56	-0.12	0.08	0.23	-0.77	0.20	0.91	0.28	0.80	0.36	0.19	0.30	0.29	-0.24	0,31
CE	-0.05	0.32	0.81	0.30	0.22	0.30	0.73	0.33	1.00	-0.06	-0.15	0.16	0.23	-0.40	-0.12	0.33	0.12	0.31	0.90	0.05	0.75	0.13	-0.2	0,08
CO	0.43	-0.77	0.24	-0.57	-0.71	-0.22	-0.23	-0.56	-0.06	1.00	-0.18	-0.29	-0.12	0.75	-0.03	-0.70	-0.33	-0.59	-0.11	-0.53	-0.28	-0.29	0.66	-0,56
CR	-0.02	0.24	-0.29	-0.15	0.05	0.13	-0.13	-0.12	-0.15	-0.18	1.00	-0.18	-0.28	-0.19	-0.37	-0.03	-0.21	-0.10	-0.16	-0.18	-0.11	-0.28	-0.24	0,27
CS	-0.26	0.44	0.10	0.42	0.45	0.06	-0.10	0.08	0.16	-0.29	-0.18	1.00	0.34	-0.45	0.31	0.38	0.53	0.56	0.46	0.81	-0.05	0.79	-0.33	0,18
CU	-0.05	0.16	0.35	0.67	0.19	0.25	0.26	0.23	0.23	-0.12	-0.28	0.34	1.00	-0.23	-0.04	0.22	0.17	0.34	0.22	0.18	0.14	0.24	-0.12	-0,14
FE	0.07	-0.97	0.05	-0.69	-0.77	-0.12	-0.55	-0.77	-0.40	0.75	-0.19	-0.45	-0.23	1.00	-0.09	-0.90	-0.50	-0.83	-0.55	-0.46	-0.38	-0.54	0.49	-0,47
GA	-0.16	0.14	-0.24	0.00	0.29	-0.11	0.00	0.20	-0.12	-0.03	-0.37	0.31	-0.04	-0.09	1.00	0.26	0.41	0.24	-0.02	0.32	-0.04	0.60	0.46	0,17
HF	0.01	0.90	-0.14	0.72	0.74	0.09	0.60	0.91	0.33	-0.70	-0.03	0.38	0.22	-0.90	0.26	1.00	0.48	0.92	0.45	0.41	0.34	0.52	-0.36	0,43
IN	-0.06	0.40	-0.02	0.40	0.78	0.37	0.29	0.28	0.12	-0.33	-0.21	0.53	0.17	-0.50	0.41	0.48	1.00	0.47	0.37	0.29	0.23	0.83	0.11	-0,02
K	0.00	0.82	-0.07	0.82	0.61	-0.02	0.55	0.80	0.31	-0.59	-0.10	0.56	0.34	-0.83	0.24	0.92	0.47	1.00	0.50	0.48	0.21	0.61	-0.37	0,22
LA	-0.07	0.46	0.69	0.36	0.36	0.23	0.64	0.36	0.90	-0.11	-0.16	0.46	0.22	-0.55	-0.02	0.45	0.37	0.50	1.00	0.24	0.52	0.44	-0.27	0,03
LI	-0.42	0.51	-0.11	0.30	0.41	-0.01	-0.19	0.19	0.05	-0.53	-0.18	0.81	0.18	-0.46	0.32	0.41	0.29	0.48	0.24	1.00	-0.09	0.60	-0.5	0,53
LU	-0.01	0.29	0.58	0.37	0.46	0.44	0.68	0.30	0.75	-0.28	-0.11	-0.05	0.14	-0.38	-0.04	0.34	0.23	0.21	0.52	-0.09	1.00	0.06	-0.04	0,2
MG	-0.18	0.48	0.00	0.41	0.66	0.09	0.19	0.29	0.13	-0.29	-0.28	0.79	0.24	-0.54	0.60	0.52	0.83	0.61	0.44	0.60	0.06	1.00	0.03	0,1
MN	0.34	-0.51	-0.06	-0.35	-0.23	-0.04	-0.01	-0.24	-0.20	0.66	-0.24	-0.33	-0.12	0.49	0.46	-0.36	0.11	-0.37	-0.27	-0.50	-0.04	0.03	1.00	-0,33
MO	-0.23	0.59	-0.21	0.06	0.44	0.22	-0.06	0.31	0.08	-0.56	0.27	0.18	-0.14	-0.47	0.17	0.43	-0.02	0.22	0.03	0.53	0.20	0.10	-0.33	1.00
NA	-0.14	0.99	-0.15	0.58	0.74	0.15	0.43	0.73	0.30	-0.76	0.32	0.36	0.11	-0.95	0.10	0.87	0.35	0.75	0.43	0.45	0.29	0.41	-0.51	0,63
NB	0.20	0.62	-0.20	0.59	0.38	-0.07	0.61	0.78	0.20	-0.46	-0.01	-0.12	0.09	-0.60	0.15	0.71	0.07	0.65	0.12	0.06	0.36	0.12	-0.06	0,37
NI	0.27	-0.88	0.09	-0.75	-0.83	-0.28	-0.38	-0.62	-0.24	0.92	-0.13	-0.44	-0.25	0.87	-0.05	-0.82	-0.45	-0.77	-0.33	-0.53	-0.42	-0.43	0.63	-0,49
P	0.01	-0.15	0.87	0.00	-0.22	0.27	0.54	-0.04	0.84	0.27	-0.04	-0.21	0.17	0.06	-0.37	-0.14	-0.27	-0.13	0.60	-0.31	0.62	-0.30	-0.03	-0,15
PB	0.42	-0.21	0.14	-0.05	-0.15	-0.05	0.13	0.00	0.04	0.25	-0.18	-0.12	-0.02	0.18	-0.12	-0.08	-0.13	-0.04	-0.06	-0.13	0.11	-0.09	0.13	-0,17
RB	-0.15	0.64	0.03	0.54	0.56	0.01	0.16	0.40	0.27	-0.38	-0.17	0.93	0.30	-0.65	0.36	0.64	0.60	0.78	0.59	0.74	0.01	0.83	-0.35	0,19
S	-0.14	0.60	0.11	0.22	0.48	-0.03	0.12	0.33	0.34	-0.26	-0.11	0.76	0.07	-0.61	0.28	0.51	0.55	0.53	0.67	0.62	-0.02	0.73	-0.32	0,26
SB	-0.11	-0.01	0.01	0.18	0.45	0.77	-0.08	-0.14	-0.16	-0.16	0.05	-0.06	0.26	0.03	-0.07	-0.05	0.41	-0.14	-0.19	-0.11	0.16	0.04	0.16	0,1
SC	-0.38	0.39	-0.20	0.11	0.51	0.09	0.01	0.19	-0.03	-0.41	-0.18	0.51	0.01	-0.40	0.60	0.33	0.57	0.34	0.16	0.68	-0.04	0.73	-0.02	0,34
SE	-0.66	0.18	0.12	0.13	0.25	0.04	0.18	0.10	0.14	-0.46	0.10	0.12	-0.01	-0.22	0.14	0.16	0.15	0.14	0.14	0.19	0.22	0.22	-0.28	0,11
SN	0.11	0.29	-0.28	0.05	0.52	0.24	0.08	0.13	-0.09	-0.25	0.21	-0.09	-0.23	-0.23	0.47	0.26	0.32	0.06	-0.17	-0.08	0.42	0.17	0.35	0,39
SR	-0.12	0.91	0.16	0.58	0.69	0.16	0.51	0.67	0.59	-0.62	0.10	0.52	0.16	-0.92	0.06	0.83	0.43	0.76	0.73	0.49	0.44	0.48	-0.54	0,48
TA	0.42	0.37	-0.15	0.47	0.21	-0.06	0.26	0.47	0.05	-0.11	-0.13	0.21	0.27	-0.35	-0.07	0.51	0.17	0.59	0.21	0.11	-0.11	0.19	-0.21	-0,15
TB	0.05	0.06	0.79	0.19	0.08	0.30	0.67	0.14	0.88	0.03	-0.12	-0.14	0.15	-0.16	-0.20	0.10	-0.07	0.04	0.61	-0.22	0.89	-0.14	-0.01	0,01
TE	-0.15	0.19	-0.07	0.11	0.57	0.83	0.01	-0.02	-0.08	-0.32	0.36	-0.04	0.11	-0.14	-0.03	0.16	0.30	0.00	-0.12	-0.05	0.22	0.04	-0.07	0,3
TH	0.02	-0.17	-0.01	-0.10	-0.15	-0.24	-0.07	-0.08	-0.10	0.13	-0.14	0.00	-0.17	0.21	0.04	-0.10	-0.16	0.00	-0.11	0.10	-0.12	0.04	0.01	-0,14
TI	0.03	0.44	-0.34	0.34	0.53	0.04	0.40	0.51	-0.04	-0.44	0.01	-0.08	0.00	-0.46	0.48	0.49	0.41	0.34	-0.12	0.05	0.39	0.32	0.31	0,35
TL	-0.23	0.60	0.14	0.53	0.62	0.14	0.10	0.26	0.28	-0.39	-0.17	0.94	0.31	-0.60	0.32	0.56	0.64	0.69	0.59	0.74	0.09	0.83	-0.37	0,19
U	-0.23	0.59	-0.14	0.42	0.53	-0.07	0.17	0.53	0.14	-0.56	-0.21	0.45	0.06	-0.55	0.31	0.65	0.35	0.62	0.31	0.54	0.10	0.45	-0.47	0,25
V	0.32	-0.81	-0.16	-0.67	-0.69	-0.25	-0.48	-0.62	-0.48	0.83	-0.07	-0.42	-0.29	0.84	0.11	-0.77	-0.36	-0.72	-0.57	-0.51	-0.44	-0.38	0.75	-0,4
W	0.40	0.45	-0.10	0.48	0.24	-0.11	0.28	0.47	0.14	-0.14	-0.06	0.32	0.25	-0.46	-0.15	0.53	0.25	0.62	0.36	0.16	-0.10	0.26	-0.33	-0,19
Y	0.04	0.08	0.76	0.20	0.12	0.32	0.66	0.15	0.85	-0.01	-0.11	-0.16	0.14	-0.17	-0.19	0.12	-0.06	0.04	0.57	-0.22	0.92	-0.15	-0.02	0,05
YB	0.01	0.20	0.64	0.31	0.32	0.38	0.66	0.23	0.77	-0.19	-0.11	-0.09	0.13	-0.29	-0.09	0.25	0.11	0.14	0.52	-0.14	0.99	-0.03	-0.03	0,15
ZN	0.25	-0.46	0.05	-0.27	-0.19	0.28	-0.14	-0.30	-0.15	0.61	-0.19	-0.28	-0.02	0.48	0.00	-0.36	0.01	-0.40	-0.23	-0.43	-0.09	-0.17	0.68	-0,2
ZR	0.04	0.88	-0.14	0.72	0.67	-0.01	0.64	0.95	0.34	-0.67	-0.09	0.34	0.24	-0.89	0.26	0.99	0.44	0.92	0.45	0.39	0.33	0.49	-0.35	0,38

	Na	NB	NI	P	PB	RB	S	SB	SC	SE	SN	SR	TA	TB	TE	TH	Ti	TL	U	V	W	Y	YB	ZN	ZR
AG	-0.14	0.2	0.27	0.01	0.42	-0.15	-0.14	-0.11	-0.38	-0.66	0.11	-0.12	0.42	0.05	-0.15	0.02	0.03	-0.23	-0.23	0.32	0.4	0.04	0.01	0.25	0.04
AL	0.99	0.62	-0.88	-0.15	-0.21	0.64	0.6	-0.01	0.39	0.18	0.29	0.91	0.37	0.06	0.19	-0.17	0.44	0.6	0.59	-0.81	0.45	0.08	0.2	-0.46	0.88
AS	-0.15	-0.2	0.09	0.87	0.14	0.03	0.11	0.01	-0.2	0.12	-0.28	0.16	-0.15	0.79	-0.07	-0.01	-0.34	0.14	-0.14	-0.16	-0.1	0.76	0.64	0.05	-0.14
BA	0.58	0.59	-0.75	0	-0.05	0.54	0.22	0.18	0.11	0.13	0.05	0.58	0.47	0.19	0.11	-0.1	0.34	0.53	0.42	-0.67	0.48	0.2	0.31	-0.27	0.72
BE	0.74	0.38	-0.83	-0.22	-0.15	0.56	0.48	0.45	0.51	0.25	0.52	0.69	0.21	0.08	0.57	-0.15	0.53	0.62	0.53	-0.69	0.24	0.12	0.32	-0.19	0.67
BI	0.15	-0.07	-0.28	0.27	-0.05	0.01	-0.03	0.77	0.09	0.04	0.24	0.16	-0.06	0.3	0.83	-0.24	0.04	0.14	-0.07	-0.25	-0.11	0.32	0.38	0.28	-0.01
CA	0.43	0.61	-0.38	0.54	0.13	0.16	0.12	-0.08	0.01	0.18	0.08	0.51	0.26	0.67	0.01	-0.07	0.4	0.1	0.17	-0.48	0.28	0.66	0.66	-0.14	0.64
CD	0.73	0.78	-0.62	-0.04	0	0.4	0.33	-0.14	0.19	0.1	0.13	0.67	0.47	0.14	-0.02	-0.08	0.51	0.26	0.53	-0.62	0.47	0.15	0.23	-0.3	0.95
CE	0.3	0.2	-0.24	0.84	0.04	0.27	0.34	-0.16	-0.03	0.14	-0.09	0.59	0.05	0.88	-0.08	-0.1	-0.04	0.28	0.14	-0.48	0.14	0.85	0.77	-0.15	0.34
CO	-0.76	-0.46	0.92	0.27	0.25	-0.38	-0.26	-0.16	-0.41	-0.46	-0.25	-0.62	-0.11	0.03	-0.32	0.13	-0.44	-0.39	-0.56	0.83	-0.14	-0.01	-0.19	0.61	-0.67
CR	0.32	-0.01	-0.13	-0.04	-0.18	-0.17	-0.11	0.05	-0.18	0.1	0.21	0.1	-0.13	-0.12	0.36	-0.14	0.01	-0.17	-0.21	-0.07	-0.06	-0.11	-0.11	-0.19	-0.09
CS	0.36	-0.12	-0.44	-0.21	-0.12	0.93	0.76	-0.06	0.51	0.12	-0.09	0.52	0.21	-0.14	-0.04	0	-0.08	0.94	0.45	-0.42	0.32	-0.16	-0.09	-0.28	0.34
CU	0.11	0.09	-0.25	0.17	-0.02	0.3	0.07	0.26	0.01	-0.01	-0.23	0.16	0.27	0.15	0.11	-0.17	0	0.31	0.06	-0.29	0.25	0.14	0.13	-0.02	0.24
FE	-0.95	-0.6	0.87	0.06	0.18	-0.65	-0.61	0.03	-0.4	-0.22	-0.23	-0.92	-0.35	-0.16	-0.14	0.21	-0.46	-0.6	-0.55	0.84	-0.46	-0.17	-0.29	0.48	-0.89
GA	0.1	0.15	-0.05	-0.37	-0.12	0.36	0.28	-0.07	0.6	0.14	0.47	0.06	-0.07	-0.2	-0.03	0.04	0.48	0.32	0.31	0.11	-0.15	-0.19	-0.09	0	0.26
HF	0.87	0.71	-0.82	-0.14	-0.08	0.64	0.51	-0.05	0.33	0.16	0.26	0.83	0.51	0.1	0.16	-0.1	0.49	0.56	0.65	-0.77	0.53	0.12	0.25	-0.36	0.99
IN	0.35	0.07	-0.45	-0.27	-0.13	0.6	0.55	0.41	0.57	0.15	0.32	0.43	0.17	-0.07	0.3	-0.16	0.41	0.64	0.35	-0.36	0.25	-0.06	0.11	0.01	0.44
K	0.75	0.65	-0.77	-0.13	-0.04	0.78	0.53	-0.14	0.34	0.14	0.06	0.76	0.59	0.04	0	0	0.34	0.69	0.62	-0.72	0.62	0.04	0.14	-0.4	0.92
LA	0.43	0.12	-0.33	0.6	-0.06	0.59	0.67	-0.19	0.16	0.14	-0.17	0.73	0.21	0.61	-0.12	-0.11	-0.12	0.59	0.31	-0.57	0.36	0.57	0.52	-0.23	0.45
LI	0.45	0.06	-0.53	-0.31	-0.13	0.74	0.62	-0.11	0.68	0.19	-0.08	0.49	0.11	-0.22	-0.05	0.1	0.05	0.74	0.54	-0.51	0.16	-0.22	-0.14	-0.43	0.39
LU	0.29	0.36	-0.42	0.62	0.11	0.01	-0.02	0.16	-0.04	0.22	0.42	0.44	-0.11	0.89	0.22	-0.12	0.39	0.09	0.1	-0.44	-0.1	0.92	0.99	-0.09	0.33
MG	0.41	0.12	-0.43	-0.3	-0.09	0.83	0.73	0.04	0.73	0.22	0.17	0.48	0.19	-0.14	0.04	0.04	0.32	0.83	0.45	-0.38	0.26	-0.15	-0.03	-0.17	0.49
MN	-0.51	-0.06	0.63	-0.03	0.13	-0.35	-0.32	0.16	-0.02	-0.28	0.35	-0.54	-0.21	-0.01	-0.07	0.01	0.31	-0.37	-0.47	0.75	-0.33	-0.02	-0.03	0.68	-0.35
MO	0.63	0.37	-0.49	-0.15	-0.17	0.19	0.26	0.1	0.34	0.11	0.39	0.48	-0.15	0.01	0.3	-0.14	0.35	0.19	0.25	-0.4	-0.19	0.05	0.15	-0.2	0.38
NA	1.00	0.6	-0.86	-0.13	-0.22	0.56	0.56	0.01	0.36	0.17	0.31	0.9	0.32	0.06	0.23	-0.2	0.44	0.52	0.54	-0.79	0.4	0.08	0.21	-0.45	0.84
NB	0.6	1.00	-0.54	-0.04	0.02	0.12	-0.04	-0.09	0.18	-0.02	0.31	0.43	0.38	0.19	0	-0.08	0.65	0.01	0.21	-0.43	0.29	0.22	0.32	-0.15	0.74
NI	-0.86	-0.54	1.00	0.17	0.15	-0.57	-0.39	-0.18	-0.36	-0.3	-0.3	-0.79	-0.32	-0.1	-0.34	0.09	-0.42	-0.59	-0.64	0.89	-0.37	-0.14	-0.32	0.53	-0.79
P	-0.13	-0.04	0.17	1.00	0.15	-0.2	-0.11	-0.14	-0.37	0.08	-0.24	0.12	-0.16	0.9	-0.09	-0.01	-0.26	-0.16	-0.24	-0.1	-0.12	0.87	0.7	0.03	-0.12
PB	-0.22	0.02	0.15	0.15	1.00	-0.1	-0.2	-0.08	-0.28	-0.36	-0.06	-0.2	0.14	0.19	-0.06	0.68	-0.01	-0.12	0.05	0.25	0.07	0.18	0.14	0.19	-0.05
RB	0.56	0.12	-0.57	-0.2	-0.1	1.00	0.85	-0.13	0.5	0.1	-0.05	0.71	0.41	-0.1	-0.06	0.02	0.04	0.96	0.62	-0.57	0.52	-0.12	-0.06	-0.33	0.62
S	0.56	-0.04	-0.39	-0.11	-0.2	0.85	1.00	-0.17	0.48	0.08	-0.09	0.74	0.22	-0.08	-0.14	-0.08	-0.06	0.83	0.54	-0.5	0.4	-0.11	-0.08	-0.28	0.49
SB	0.01	-0.09	-0.18	-0.14	-0.08	-0.13	-0.17	1.00	0	-0.1	0.33	-0.08	-0.08	-0.08	0.74	-0.18	0.17	0.02	-0.12	-0.01	-0.16	-0.05	0.08	0.44	-0.12
SC	0.36	0.18	-0.36	-0.37	-0.28	0.5	0.48	0	1.00	0.23	0.18	0.29	0	-0.24	0.04	-0.14	0.42	0.48	0.27	-0.3	0.04	-0.23	-0.13	-0.26	0.32
SE	0.17	-0.02	-0.3	0.08	-0.36	0.1	0.08	-0.1	0.23	1.00	-0.01	0.17	-0.49	0.14	0.09	0.05	0.15	0.15	0.22	-0.42	-0.43	0.16	0.2	-0.54	0.15
SN	0.31	0.31	-0.3	-0.24	-0.06	-0.05	-0.09	0.33	0.18	-0.01	1.00	0.15	-0.1	0.1	0.45	-0.17	0.71	0	0.04	0	-0.18	0.16	0.35	0.06	0.21
SR	0.9	0.43	-0.79	0.12	-0.2	0.71	0.74	-0.08	0.29	0.17	0.15	1.00	0.32	0.29	0.08	-0.2	0.23	0.69	0.62	-0.83	0.46	0.29	0.37	-0.44	0.81
TA	0.32	0.38	-0.32	-0.16	0.14	0.41	0.22	-0.08	0	-0.49	-0.1	0.32	1.00	-0.15	0.03	0.01	-0.07	0.33	0.3	-0.32	0.95	-0.16	-0.14	-0.03	0.51
TB	0.06	0.19	-0.1	0.9	0.19	-0.1	-0.08	-0.08	-0.24	0.14	0.1	0.29	-0.15	1.00	-0.01	-0.04	0.08	-0.06	-0.08	-0.26	-0.13	1	0.94	-0.04	0.12
TE	0.23	0	-0.34	-0.09	-0.06	-0.06	-0.14	0.74	0.04	0.09	0.45	0.08	0.03	-0.01	1.00	-0.15	0.13	0.06	0.04	-0.22	-0.06	0.02	0.14	0.16	0.05
TH	-0.2	-0.08	0.09	-0.01	0.68	0.02	-0.08	-0.18	-0.14	0.05	-0.17	-0.2	0.01	-0.04	-0.15	1.00	-0.13	0.04	0.33	0.11	-0.06	-0.05	-0.1	0.01	-0.08
TI	0.44	0.65	-0.42	-0.26	-0.01	0.04	-0.06	0.17	0.42	0.15	0.71	0.23	-0.07	0.08	0.13	-0.13	1.00	-0.02	0.09	-0.16	-0.12	0.13	0.31	-0.04	0.51
TL	0.52	0.01	-0.59	-0.16	-0.12	0.96	0.83	0.02	0.48	0.15	0	0.69	0.33	-0.06	0.06	0.04	-0.02	1.00	0.61	-0.58	0.44	-0.07	0.01	-0.3	0.51
U	0.54	0.21	-0.64	-0.24	0.05	0.62	0.54	-0.12	0.27	0.22	0.04	0.62	0.3	-0.08	0.04	0.33	0.09	0.61	1.00	-0.62	0.34	-0.08	0.03	-0.39	0.64
V	-0.79	-0.43	0.89	-0.1	0.25	-0.57	-0.5	-0.01	-0.3	-0.42	0	-0.83	-0.32	-0.26	-0.22	0.11	-0.16	-0.58	-0.62	1.00	-0.4	-0.28	-0.37	0.61	-0.74
W	0.4	0.29	-0.37	-0.12	0.07	0.52	0.4	-0.16	0.04	-0.43	-0.18	0.46	0.95	-0.13	-0.06	-0.06	-0.12	0.44	0.34	-0.4	1.00	-0.15	-0.14	-0.16	0.53
Y	0.08	0.22	-0.14	0.87	0.18	-0.12	-0.11	-0.05	-0.23	0.16	0.16	0.29	-0.16	1	0.02	-0.05	0.13	-0.07	-0.08	-0.28	-0.15	1.00	0.96	-0.05	0.13
YB	0.21	0.32	-0.32	0.7	0.14	-0.06	-0.08	0.08	-0.13	0.2	0.35	0.37	-0.14	0.94	0.14	-0.1	0.31	0.01	0.03	-0.37	-0.14	0.96	1.00	-0.08	0.25
ZN	-0.45	-0.15	0.53	0.03	0.19	-0.33	-0.28	0.44	-0.26	-0.54	0.06	-0.44	-0.03	-0.04	0.16	0.01	-0.04	-0.3	-0.39	0.61	-0.16	-0.05	-0.08	1.00	-0.39
ZR	0.84	0.74	-0.79	-0.12	-0.05	0.62	0.49	-0.12	0.32	0.15	0.21	0.81	0.51	0.12	0.05	-0.08	0.51	0.51	0.64	-0.74	0.53	0.13	0.25	-0.39	1.00

	AG	Al	AS	BA	BE	BI	Ca	CD	CE	CO	CR	CS	CU	Fe	GA	HF	IN	K	LA	LI	LU	Mg	MN	MO
AG	1.00	-0.21	0.49	-0.11	-0.28	0.36	0.06	-0.14	-0.01	-0.14	-0.08	0.04	-0.04	0.05	-0.18	-0.10	-0.32	-0.23	-0.02	-0.24	0.02	-0.23	-0.19	0.18
AL	-0.21	1.00	-0.03	-0.14	0.76	-0.23	0.01	0.41	-0.21	0.05	-0.33	0.43	0.38	-0.42	-0.04	0.60	0.80	0.75	-0.21	0.64	0.02	0.74	0.52	-0.15
AS	0.49	-0.03	1.00	-0.09	-0.08	0.36	0.81	-0.44	0.43	-0.45	0.21	-0.18	-0.33	-0.38	0.47	-0.14	-0.13	-0.14	0.27	-0.23	0.79	-0.30	-0.15	-0.14
BA	-0.11	-0.14	-0.09	1.00	-0.21	0.00	-0.24	-0.12	0.82	-0.27	-0.19	-0.16	-0.28	-0.26	0.44	-0.13	-0.18	-0.15	0.91	-0.16	-0.21	-0.22	-0.40	-0.06
BE	-0.28	0.76	-0.08	-0.21	1.00	-0.27	0.15	0.60	-0.23	0.16	-0.08	0.39	0.44	-0.39	0.08	0.82	0.97	0.85	-0.25	0.92	0.18	0.90	0.39	-0.28
BI	0.36	-0.23	0.36	0.00	-0.27	1.00	0.10	-0.31	0.13	-0.41	0.11	-0.32	0.38	-0.01	-0.01	-0.20	-0.26	-0.31	0.12	-0.33	0.11	-0.28	0.05	0.43
CA	0.06	0.01	0.81	-0.24	0.15	0.10	1.00	-0.31	0.35	-0.29	0.45	-0.14	-0.34	-0.35	0.53	-0.05	0.04	-0.04	0.16	0.00	0.99	-0.09	-0.10	-0.22
CD	-0.14	0.41	-0.44	-0.12	0.60	-0.31	-0.31	1.00	-0.38	0.04	-0.06	0.33	0.20	-0.25	-0.24	0.71	0.62	0.66	-0.32	0.55	-0.28	0.63	0.40	0.14
CE	-0.01	-0.21	0.43	0.82	-0.23	0.13	0.35	-0.38	1.00	-0.47	0.09	-0.30	-0.50	-0.40	0.72	-0.26	-0.26	-0.27	0.98	-0.28	0.37	-0.38	-0.48	-0.14
CO	-0.14	0.05	-0.45	-0.27	0.16	-0.41	-0.29	0.04	-0.47	1.00	-0.31	0.16	0.25	0.68	-0.19	0.09	0.11	0.11	-0.43	0.32	-0.31	0.23	-0.20	-0.30
CR	-0.08	-0.33	0.21	-0.19	-0.08	0.11	0.45	-0.06	0.09	-0.31	1.00	-0.01	-0.20	0.11	0.29	-0.28	-0.09	-0.29	0.01	-0.18	0.49	-0.07	-0.37	-0.18
CS	0.04	0.43	-0.18	-0.16	0.39	-0.32	-0.14	0.33	-0.30	0.16	-0.01	1.00	0.18	-0.18	-0.35	0.56	0.39	0.61	-0.28	0.59	-0.13	0.63	0.11	-0.19
CU	-0.04	0.38	-0.33	-0.28	0.44	0.38	-0.34	0.20	-0.50	0.25	-0.20	0.18	1.00	0.13	-0.44	0.34	0.46	0.30	-0.43	0.46	-0.34	0.57	0.39	0.26
FE	0.05	-0.42	-0.38	-0.26	-0.39	-0.01	-0.35	-0.25	-0.40	0.68	0.11	-0.18	0.13	1.00	-0.15	-0.45	-0.37	-0.46	-0.36	-0.26	-0.35	-0.26	-0.44	-0.14
GA	-0.18	-0.04	0.47	0.44	0.08	-0.01	0.53	-0.24	0.72	-0.19	0.29	-0.35	-0.44	-0.15	1.00	-0.08	0.06	-0.03	0.64	-0.09	0.58	-0.23	-0.57	-0.59
HF	-0.10	0.60	-0.14	-0.13	0.82	-0.20	-0.05	0.71	-0.26	0.09	-0.28	0.56	0.34	-0.45	-0.08	1.00	0.78	0.96	-0.25	0.84	-0.03	0.75	0.40	-0.16
IN	-0.32	0.80	-0.13	-0.18	0.97	-0.26	0.04	0.62	-0.26	0.11	-0.09	0.39	0.46	-0.37	0.06	0.78	1.00	0.84	-0.27	0.87	0.07	0.90	0.42	-0.29
K	-0.23	0.75	-0.14	-0.15	0.85	-0.31	-0.04	0.66	-0.27	0.11	-0.29	0.61	0.30	-0.46	-0.03	0.96	0.84	1.00	-0.27	0.84	-0.01	0.79	0.44	-0.26
LA	-0.02	-0.21	0.27	0.91	-0.25	0.12	0.16	-0.32	0.98	-0.43	0.01	-0.28	-0.43	-0.36	0.64	-0.25	-0.27	-0.27	1.00	-0.27	0.19	-0.35	-0.47	-0.08
LI	-0.24	0.64	-0.23	-0.16	0.92	-0.33	0.00	0.55	-0.28	0.32	-0.18	0.59	0.46	-0.26	-0.09	0.84	0.87	0.84	-0.27	1.00	0.02	0.93	0.32	-0.27
LU	0.02	0.02	0.79	-0.21	0.18	0.11	0.99	-0.28	0.37	-0.31	0.49	-0.13	-0.34	-0.35	0.58	-0.03	0.07	-0.01	0.19	0.02	1.00	-0.07	-0.12	-0.25
MG	-0.23	0.74	-0.30	-0.22	0.90	-0.28	-0.09	0.63	-0.38	0.23	-0.07	0.63	0.57	-0.26	-0.23	0.75	0.90	0.79	-0.35	0.93	-0.07	1.00	0.41	-0.13
MN	-0.19	0.52	-0.15	-0.40	0.39	0.05	-0.10	0.40	-0.48	-0.20	-0.37	0.11	0.39	-0.44	-0.57	0.40	0.42	0.44	-0.47	0.32	-0.12	0.41	1.00	0.53
MO	0.18	-0.15	-0.14	-0.06	-0.28	0.43	-0.22	0.14	-0.14	-0.30	-0.18	-0.19	0.26	-0.14	-0.59	-0.16	-0.29	-0.26	-0.08	-0.27	-0.25	-0.13	0.53	1.00
NA	-0.16	0.49	-0.27	-0.15	0.41	-0.04	-0.22	0.58	-0.31	-0.07	0.15	-0.06	0.41	-0.07	-0.09	0.18	0.49	0.23	-0.26	0.15	-0.19	0.43	0.29	0.17
NB	0.11	0.03	-0.32	-0.18	0.08	0.26	-0.34	0.49	-0.38	-0.07	-0.30	0.08	0.45	-0.20	-0.70	0.28	0.05	0.15	-0.31	0.13	-0.37	0.23	0.64	0.86
NI	0.07	-0.49	-0.26	-0.42	-0.50	-0.17	-0.17	-0.25	-0.46	0.54	-0.03	-0.15	-0.07	0.61	-0.50	-0.47	-0.56	-0.51	-0.45	-0.38	-0.23	-0.37	-0.08	0.24
P	0.20	-0.04	0.89	-0.25	0.03	0.10	0.97	-0.41	0.34	-0.24	0.36	-0.17	-0.40	-0.28	0.52	-0.14	-0.07	-0.12	0.15	-0.11	0.95	-0.21	-0.17	-0.27
PB	0.08	-0.19	0.07	-0.25	-0.25	0.35	0.09	0.04	-0.16	-0.14	-0.05	-0.13	-0.10	0.08	-0.05	0.10	-0.32	0.02	-0.19	-0.26	0.10	-0.35	0.17	0.29
RB	-0.16	0.70	-0.11	-0.15	0.77	-0.29	-0.05	0.63	-0.28	0.09	-0.28	0.70	0.26	-0.45	-0.08	0.95	0.77	0.99	-0.27	0.80	-0.03	0.74	0.40	-0.25
S	0.61	-0.30	-0.16	1.00	-0.42	0.26	-0.37	-0.22	0.85	-0.34	-0.22	-0.27	-0.35	-0.29	0.52	-0.26	-0.40	-0.33	0.93	-0.31	-0.34	-0.36	-0.65	0.36
SB	0.72	-0.21	0.18	-0.23	-0.37	0.51	-0.15	0.02	-0.25	-0.16	-0.17	0.13	0.15	0.06	-0.46	0.03	-0.40	-0.10	-0.22	-0.29	-0.18	-0.25	0.12	0.55
SC	-0.32	0.29	-0.51	-0.18	0.60	-0.20	-0.35	0.57	-0.44	0.55	-0.10	-0.05	0.51	0.33	0.01	0.43	0.63	0.42	-0.38	0.54	-0.31	0.54	0.08	-0.23
SE	-0.32	0.15	0.52	-0.17	0.13	-0.20	0.78	-0.37	0.28	0.01	0.25	-0.16	-0.31	-0.20	0.46	-0.21	0.09	-0.08	0.12	0.00	0.77	-0.04	-0.03	-0.24
SN	0.07	-0.17	-0.06	0.02	0.00	0.07	0.01	-0.24	0.04	0.17	0.15	-0.30	0.25	0.25	-0.11	-0.43	-0.01	-0.47	0.06	0.02	-0.02	0.09	-0.11	0.11
SR	-0.05	-0.20	0.06	0.99	-0.26	0.05	-0.10	-0.22	0.90	-0.33	-0.11	-0.23	-0.36	-0.28	0.53	-0.21	-0.25	-0.23	0.96	-0.24	-0.07	-0.31	-0.47	-0.08
TA	-0.34	0.37	-0.33	0.33	0.59	-0.40	-0.25	0.51	0.07	-0.01	-0.36	0.36	0.07	-0.51	0.02	0.74	0.57	0.72	0.14	0.66	-0.23	0.52	0.25	-0.26
TB	0.09	-0.09	0.86	0.08	-0.03	0.12	0.93	-0.45	0.63	-0.39	0.38	-0.24	-0.51	-0.39	0.70	-0.19	-0.11	-0.17	0.46	-0.17	0.93	-0.29	-0.28	-0.28
TE	0.00	0.00	0.00	0.00	0.00	0.00	0.00	0.00	0.00	0.00	0.00	0.00	0.00	0.00	0.00	0.00	0.00	0.00	0.00	0.00	0.00	0.00	0.00	0.00
TH	0.11	-0.25	0.00	-0.29	-0.19	0.29	0.06	-0.27	-0.21	0.44	-0.05	-0.24	0.11	0.67	0.11	-0.14	-0.25	-0.18	-0.24	-0.11	0.06	-0.26	-0.24	-0.11
TI	-0.21	0.49	-0.08	-0.17	0.53	-0.12	0.02	0.53	-0.20	-0.12	0.34	-0.04	0.24	-0.12	0.22	0.27	0.61	0.34	-0.20	0.24	0.06	0.43	0.11	-0.20
TL	-0.02	0.63	-0.12	-0.22	0.73	-0.11	-0.11	0.58	-0.37	0.07	-0.19	0.80	0.45	-0.39	-0.26	0.90	0.74	0.90	-0.35	0.81	-0.09	0.81	0.42	-0.13
U	0.32	-0.29	-0.12	-0.21	-0.39	0.36	-0.23	0.10	-0.28	-0.12	-0.19	-0.03	0.15	0.04	-0.67	-0.14	-0.42	-0.25	-0.24	-0.29	-0.27	-0.21	0.41	0.91
V	0.06	-0.29	-0.36	-0.33	-0.31	0.05	-0.40	-0.20	-0.50	0.63	0.02	-0.13	0.22	0.96	-0.21	-0.36	-0.24	-0.34	-0.46	-0.20	-0.39	-0.18	-0.28	-0.14
W	-0.32	0.36	-0.29	0.39	0.54	-0.38	-0.23	0.47	0.15	-0.05	-0.38	0.37	0.01	-0.54	0.08	0.73	0.53	0.72	0.21	0.62	-0.21	0.47	0.22	-0.28
Y	0.08	-0.05	0.84	-0.16	0.07	0.11	0.99	-0.38	0.42	-0.31	0.46	-0.18	-0.41	-0.32	0.60	-0.13	-0.03	-0.11	0.24	-0.09	0.99	-0.18	-0.19	-0.27
YB	0.01	0.01	0.80	-0.20	0.14	0.10	0.99	-0.32	0.38	-0.29	0.48	-0.15	-0.37	-0.33	0.59	-0.07	0.04	-0.04	0.19	-0.02	1.00	-0.11	-0.14	-0.26
ZN	-0.13	-0.05	-0.57	-0.14	0.18	-0.11	-0.46	0.24	-0.43	0.66	0.10	0.02	0.43	0.76	-0.03	0.07	0.21	0.05	-0.35	0.25	-0.43	0.26	-0.34	-0.31
ZR	-0.13	0.64	-0.19	-0.13	0.84	-0.22	-0.10	0.74	-0.30	0.12	-0.28	0.58	0.38	-0.43	-0.12	1.00	0.81	0.97	-0.27	0.86	-0.08	0.80	0.42	-0.15

	Na	NB	NI	P	PB	RB	S	SB	SC	SE	SN	SR	TA	TB	TE	TH	Ti	TL	U	V	W	Y	YB	ZN	ZR
AG	-0.16	0.11	0.07	0.20	0.08	-0.16	0.61	0.72	-0.32	-0.32	0.07	-0.05	-0.34	0.09	0.00	0.11	-0.21	-0.02	0.32	0.06	-0.32	0.08	0.01	-0.13	-0.13
AL	0.49	0.03	-0.49	-0.04	-0.19	0.70	-0.30	-0.21	0.29	0.15	-0.17	-0.20	0.37	-0.09	0.00	-0.25	0.49	0.63	-0.29	-0.29	0.36	-0.05	0.01	-0.05	0.64
AS	-0.27	-0.32	-0.26	0.89	0.07	-0.11	-0.16	0.18	-0.51	0.52	-0.06	0.06	-0.33	0.86	0.00	0.00	-0.08	-0.12	-0.12	-0.36	-0.29	0.84	0.80	-0.57	-0.19
BA	-0.15	-0.18	-0.42	-0.25	-0.25	-0.15	1.00	-0.23	-0.18	-0.17	0.02	0.99	0.33	0.08	0.00	-0.29	-0.17	-0.22	-0.21	-0.33	0.39	-0.16	-0.20	-0.14	-0.13
BE	0.41	0.08	-0.50	0.03	-0.25	0.77	-0.42	-0.37	0.60	0.13	0.00	-0.26	0.59	-0.03	0.00	-0.19	0.53	0.73	-0.39	-0.31	0.54	0.07	0.14	0.18	0.84
BI	-0.04	0.26	-0.17	0.10	0.35	-0.29	0.26	0.51	-0.20	-0.20	0.07	0.05	-0.40	0.12	0.00	0.29	-0.12	-0.11	0.36	0.05	-0.38	0.11	0.10	-0.11	-0.22
CA	-0.22	-0.34	-0.17	0.97	0.09	-0.05	-0.37	-0.15	-0.35	0.78	0.01	-0.10	-0.25	0.93	0.00	0.06	0.02	-0.11	-0.23	-0.40	-0.23	0.99	0.99	-0.46	-0.10
CD	0.58	0.49	-0.25	-0.41	0.04	0.63	-0.22	0.02	0.57	-0.37	-0.24	-0.22	0.51	-0.45	0.00	-0.27	0.53	0.58	0.10	-0.20	0.47	-0.38	-0.32	0.24	0.74
CE	-0.31	-0.38	-0.46	0.34	-0.16	-0.28	0.85	-0.25	-0.44	0.28	0.04	0.90	0.07	0.63	0.00	-0.21	-0.20	-0.37	-0.28	-0.50	0.15	0.42	0.38	-0.43	-0.30
CO	-0.07	-0.07	0.54	-0.24	-0.14	0.09	-0.34	-0.16	0.55	0.01	0.17	-0.33	-0.01	-0.39	0.00	0.44	-0.12	0.07	-0.12	0.63	-0.05	-0.31	-0.29	0.66	0.12
CR	0.15	-0.30	-0.03	0.36	-0.05	-0.28	-0.22	-0.17	-0.10	0.25	0.15	-0.11	-0.36	0.38	0.00	-0.05	0.34	-0.19	-0.19	0.02	-0.38	0.46	0.48	0.10	-0.28
CS	-0.06	0.08	-0.15	-0.17	-0.13	0.70	-0.27	0.13	-0.05	-0.16	-0.30	-0.23	0.36	-0.24	0.00	-0.24	-0.04	0.80	-0.03	-0.13	0.37	-0.18	-0.15	0.02	0.58
CU	0.41	0.45	-0.07	-0.40	-0.10	0.26	-0.35	0.15	0.51	-0.31	0.25	-0.36	0.07	-0.51	0.00	0.11	0.24	0.45	0.15	0.22	0.01	-0.41	-0.37	0.43	0.38
FE	-0.07	-0.20	0.61	-0.28	0.08	-0.45	-0.29	0.06	0.33	-0.20	0.25	-0.28	-0.51	-0.39	0.00	0.67	-0.12	-0.39	0.04	0.96	-0.54	-0.32	-0.33	0.76	-0.43
GA	-0.09	-0.70	-0.50	0.52	-0.05	-0.08	0.52	-0.46	0.01	0.46	-0.11	0.53	0.02	0.70	0.00	0.11	0.22	-0.26	-0.67	-0.21	0.08	0.60	0.59	-0.03	-0.12
HF	0.18	0.28	-0.47	-0.14	0.10	0.95	-0.26	0.03	0.43	-0.21	-0.43	-0.21	0.74	-0.19	0.00	-0.14	0.27	0.90	-0.14	-0.36	0.73	-0.13	-0.07	0.07	1.00
IN	0.49	0.05	-0.56	-0.07	-0.32	0.77	-0.40	-0.40	0.63	0.09	-0.01	-0.25	0.57	-0.11	0.00	-0.25	0.61	0.74	-0.42	-0.24	0.53	-0.03	0.04	0.21	0.81
K	0.23	0.15	-0.51	-0.12	0.02	0.99	-0.33	-0.10	0.42	-0.08	-0.47	-0.23	0.72	-0.17	0.00	-0.18	0.34	0.90	-0.25	-0.34	0.72	-0.11	-0.04	0.05	0.97
LA	-0.26	-0.31	-0.45	0.15	-0.19	-0.27	0.93	-0.22	-0.38	0.12	0.06	0.96	0.14	0.46	0.00	-0.24	-0.20	-0.35	-0.24	-0.46	0.21	0.24	0.19	-0.35	-0.27
LI	0.15	0.13	-0.38	-0.11	-0.26	0.80	-0.31	-0.29	0.54	0.00	0.02	-0.24	0.66	-0.17	0.00	-0.11	0.24	0.81	-0.29	-0.20	0.62	-0.09	-0.02	0.25	0.86
LU	-0.19	-0.37	-0.23	0.95	0.10	-0.03	-0.34	-0.18	-0.31	0.77	-0.02	-0.07	-0.23	0.93	0.00	0.06	0.06	-0.09	-0.27	-0.39	-0.21	0.99	1.00	-0.43	-0.08
MG	0.43	0.23	-0.37	-0.21	-0.35	0.74	-0.36	-0.25	0.54	-0.04	0.09	-0.31	0.52	-0.29	0.00	-0.26	0.43	0.81	-0.21	-0.18	0.47	-0.18	-0.11	0.26	0.80
MN	0.29	0.64	-0.08	-0.17	0.17	0.40	-0.65	0.12	0.08	-0.03	-0.11	-0.47	0.25	-0.28	0.00	-0.24	0.11	0.42	0.41	-0.28	0.22	-0.19	-0.14	-0.34	0.42
MO	0.17	0.86	0.24	-0.27	0.29	-0.25	0.36	0.55	-0.23	-0.24	0.11	-0.08	-0.26	-0.28	0.00	-0.11	-0.20	-0.13	0.91	-0.14	-0.28	-0.27	-0.26	-0.31	-0.15
NA	1.00	0.24	-0.20	-0.28	-0.20	0.15	-0.21	-0.11	0.53	-0.13	0.09	-0.19	-0.01	-0.33	0.00	-0.30	0.90	0.15	-0.07	-0.04	-0.07	-0.26	-0.21	0.31	0.24
NB	0.24	1.00	0.20	-0.40	0.25	0.16	-0.23	0.52	0.08	-0.38	-0.01	-0.25	0.09	-0.48	0.00	-0.16	-0.09	0.28	0.83	-0.17	0.05	-0.42	-0.39	-0.13	0.30
NI	-0.20	0.20	1.00	-0.07	0.08	-0.48	-0.37	0.19	-0.08	0.04	0.23	-0.41	-0.46	-0.26	0.00	0.23	-0.38	-0.43	0.42	0.50	-0.50	-0.18	-0.20	0.15	-0.47
P	-0.28	-0.40	-0.07	1.00	0.06	-0.12	-0.38	-0.08	-0.41	0.77	0.00	-0.10	-0.32	0.93	0.00	0.06	-0.05	-0.17	-0.23	-0.33	-0.30	0.98	0.96	-0.49	-0.19
PB	-0.20	0.25	0.08	0.06	1.00	0.08	-0.30	0.59	-0.18	-0.21	-0.67	-0.25	-0.19	0.01	0.00	0.60	-0.23	-0.02	0.46	0.09	-0.14	0.07	0.10	-0.09	0.06
RB	0.15	0.16	-0.48	-0.12	0.08	1.00	-0.32	0.00	0.32	-0.13	-0.54	-0.23	0.69	-0.17	0.00	-0.18	0.25	0.94	-0.19	-0.33	0.70	-0.12	-0.06	0.01	0.95
S	-0.21	-0.23	-0.37	-0.38	-0.30	-0.32	1.00	-0.14	-0.30	-0.36	0	0.99	0.20	-0.01	0.00	-0.42	-0.30	-0.33	-0.15	-0.47	0.29	-0.29	-0.34	-0.13	-0.26
SB	-0.11	0.52	0.19	-0.08	0.59	0.00	-0.14	1.00	-0.34	-0.49	-0.36	-0.22	-0.34	-0.20	0.00	0.27	-0.30	0.12	0.74	0.10	-0.31	-0.16	-0.19	-0.14	0.00
SC	0.53	0.08	-0.08	-0.41	-0.18	0.32	-0.30	-0.34	1.00	-0.21	0.17	-0.27	0.30	-0.47	0.00	0.19	0.57	0.28	-0.30	0.38	0.23	-0.38	-0.33	0.79	0.47
SE	-0.13	-0.38	0.04	0.77	-0.21	-0.13	-0.36	-0.49	-0.21	1.00	0.16	-0.06	-0.27	0.76	0.00	-0.08	0.02	-0.22	-0.29	-0.23	-0.26	0.79	0.79	-0.37	-0.23
SN	0.09	-0.01	0.23	0.00	-0.67	-0.54	0	-0.36	0.17	0.16	1.00	0.05	-0.22	0.00	0.00	-0.12	0.00	-0.37	-0.06	0.19	-0.31	0.00	-0.02	0.20	-0.39
SR	-0.19	-0.25	-0.41	-0.10	-0.25	-0.23	0.99	-0.22	-0.27	-0.06	0.05	1.00	0.23	0.23	0.00	-0.28	-0.18	-0.31	-0.23	-0.37	0.30	-0.02	-0.06	-0.22	-0.22
TA	-0.01	0.09	-0.46	-0.32	-0.19	0.69	0.20	-0.34	0.30	-0.47	-0.22	0.23	1.00	-0.23	0.00	-0.41	0.09	0.58	-0.34	-0.48	0.99	-0.29	-0.26	-0.04	0.74
TB	-0.33	-0.48	-0.26	0.93	0.01	-0.17	-0.01	-0.20	-0.47	0.76	0.00	0.23	-0.23	1.00	0.00	-0.03	-0.08	-0.26	-0.30	-0.45	-0.18	0.97	0.94	-0.55	-0.24
TE	0.00	0.00	0.00	0.00	0.00	0.00	0.00	0.00	0.00	0.00	0.00	0.00	0.00	0.00	1.00	0.00	0.00	0.00	0.00	0.00	0.00	0.00	0.00	0.00	0.00
TH	-0.30	-0.16	0.23	0.06	0.60	-0.18	-0.42	0.27	0.19	-0.08	-0.12	-0.28	-0.41	-0.03	0.00	1.00	-0.26	-0.21	0.09	0.67	-0.39	0.06	0.07	0.48	-0.16
TI	0.90	-0.09	-0.38	-0.05	-0.23	0.25	-0.30	-0.30	0.57	0.02	0.00	-0.18	0.09	-0.08	0.00	-0.26	1.00	0.20	-0.41	-0.08	0.04	0.00	0.05	0.32	0.31
TL	0.15	0.28	-0.43	-0.17	-0.02	0.94	-0.33	0.12	0.28	-0.22	-0.37	-0.31	0.58	-0.26	0.00	-0.21	0.20	1.00	-0.06	-0.25	0.58	-0.18	-0.13	0.05	0.90
U	-0.07	0.83	0.42	-0.23	0.46	-0.19	-0.15	0.74	-0.30	-0.29	-0.06	-0.23	-0.34	-0.30	0.00	0.09	-0.41	-0.06	1.00	0.05	-0.34	-0.27	-0.27	-0.25	-0.14
V	-0.04	-0.17	0.50	-0.33	0.09	-0.33	-0.47	0.10	0.38	-0.23	0.19	-0.37	-0.48	-0.45	0.00	0.67	-0.08	-0.25	0.05	1.00	-0.51	-0.37	-0.37	0.75	-0.34
W	-0.07	0.05	-0.50	-0.30	-0.14	0.70	0.29	-0.31	0.23	-0.26	-0.31	0.30	0.99	-0.18	0.00	-0.39	0.04	0.58	-0.34	-0.51	1.00	-0.26	-0.23	-0.09	0.73
Y	-0.26	-0.42	-0.18	0.98	0.07	-0.12	-0.29	-0.16	-0.38	0.79	0.00	-0.02	-0.29	0.97	0.00	0.06	0.00	-0.18	-0.27	-0.37	-0.26	1.00	0.99	-0.47	-0.18
YB	-0.21	-0.39	-0.20	0.96	0.10	-0.06	-0.34	-0.19	-0.33	0.79	-0.02	-0.06	-0.26	0.94	0.00	0.07	0.05	-0.13	-0.27	-0.37	-0.23	0.99	1.00	-0.44	-0.11
ZN	0.31	-0.13	0.15	-0.49	-0.09	0.01	-0.13	-0.14	0.79	-0.37	0.20	-0.22	-0.04	-0.55	0.00	0.48	0.32	0.05	-0.25	0.75	-0.09	-0.47	-0.44	1.00	0.11
ZR	0.24	0.30	-0.47	-0.19	0.06	0.95	-0.26	0.00	0.47	-0.23	-0.39	-0.22	0.74	-0.24	0.00	-0.16	0.31	0.90	-0.14	-0.34	0.73	-0.18	-0.11	0.11	1.00

13.5 Drillcore Results

This section comprises all drillcore logging results. The abbreviations used in the logging are explained in the following.

Rock types	
OVB	Overburden
CONq	Conglomerate connected to quartzitic sandstone
QT	Quartzitic sandstone
CHT	Chert
MUD	Mudstone
CONgr	Conglomerate connected to greywacke Greywacke
GRW	Low grade hematite and magnetite
lgHEM	Low grade hematite
lgHEM	Low grade magnetite
lgMAG + HM	Hematite and Magnetite
HEM	Hematite
MAG	Magnetite
DIA	Diabase
BAS	Basalt
RD, QP	Rhyodacite
TA, SP	Trachyandesite

Texture	
Agg	Agglomerate
Por	Porphyritic

Colours	
1	Black
2	Blue
3	Green
4	Red
5	Yellow
6	Purple
7	Grey
8	Brown
9	White

Grainsize	
cg	coarse grained
fg	fine grained
vfg	very fine grained

Table 13.7 Drillcore logging results for PG81156 and PG81163.

Drillhole	From	To	Rocktype	Colour	Grainsize	Texture	Comments
81156	38.90	41.00	CONgr	47	fmg		Inhomogeneous deformed fragments of dark dense rock and red rock.
81156	41.00	47.25	MUD	7	fg		
81156	47.25	67.10	GRW	7	fmg		deformed small clasts different in nature. Local parts with finer grained>>mudstone
81156	67.10	91.30	CONgr	47	mg		deformed small clasts different in nature (porphyry Qz grey rock?)
81156	91.30	94.10	lgHEM	7	vfg		Inhomogeneous
81156	94.10	106.45	MUD	7	fg		Very homogenous
81156	106.45	143.70	GRW	7	mg		The same as before but with clear layering. Layer of silicate. Fragmentation occurs but not so many that you would call the conglomerate. The proportion of fragments (polymikt) increases towards the end of the section. Many Qz veins >>>tends to mudstone
81156	143.70	166.00	GRW				Similar rock as above but more Hem. often weathered
81156	166.00	187.20	BAS	7	fg		intermediate metavolcanic (andesite? Volcanoclastic ?). In early porphyritic stage since it looks like the whole rock is full small Pl? looks sedimentary (greywacke ?)
81156	187.20	200.60	BAS	37	fg		intermediate metavolcanic (andesite? Volcanoclastic ?). Here it is also common with silicates in small cracks. (greywacke?)
81156	200.60	205.65	BAS				Inhomogeneous Weathered Hem-clasts
81156	205.65	209.70	BAS	47	fg		intermediate metavolcanic (andesite?). reddish-gray but the same rock that pre and post
81156	209.70	247.05	BAS	7	fg		intermediate metavolcanic (andesite?) Homogeneous gray with some diffuse Pl
81156	247.05	260.00	BAS	47	mg		gradual transition between the previous rock and the ore.
81156	260.00	263.00	BAS	7	aph		Apatite clasts (fine grained Ap?). Clasts between 3 mm and 5 cm. Mag occur at the end.
81156	263.00	266.00	lgHEM	7	aph		Apatite clasts (fine grained Ap?). Clasts between 3 mm and 5 cm. Mag occur at the end.
81156	266.00	269.00	GRW	7	aph		Apatite clasts (fine grained Ap?). Clasts between 3 mm and 5 cm. Mag occur at the end.
81156	269.00	272.00	lgHEM	7	aph		Apatite clasts (fine grained Ap?). Clasts between 3 mm and 5 cm. Mag occur at the end.
81156	272.00	275.00	GRW	7	aph		Apatite clasts (fine grained Ap?). Clasts between 3 mm and 5 cm. Mag occur at the end.
81156	275.00	290.00	GRW	47	fg		Inhomogeneous fragments and layers of silicates K-Fsp (often brick red) and Pl.
81156	290.00	294.30	lgHEM	47	fg		Inhomogeneous fragments and layers of silicates K-Fsp (often brick red) and Pl.
81156	294.30	296.10	lgHEM	17	fmg		Inhomogeneous unit: mix between Mag and porphyry. Red phenocrysts still visible.
81156	296.10	304.10	GRW	17	fmg		Inhomogeneous unit: mix between Mag and porphyry. Red phenocrysts still visible.
81156	304.10	306.80	MAG	7	vfg		Mag with Qz. 3-mm Fsp sprinkle barley occur. At the end Hem occurs in the fractures.
81156	306.80	312.15	lgMAG	7	vfg		Mag with Qz. 3-mm Fsp sprinkle barley occur. At the end Hem occurs in the fractures.
81156	312.15	314.80	MAG	7	vfg		Mag with Qz. 3-mm Fsp sprinkle barley occur. At the end Hem occurs in the fractures.
81156	314.80	328.65	RD	37	fmg		Strongly inhomogeneous metamorphosed porphyry with some Mag. Phenocrysts are occasionnaly visible.
81156	328.65	330.00	RD		mg		Grey black matrix with red phenocrysts
81156	330.00	332.60	RD	7	fg		Replenishing? Of phyllite? Fine-grained layered with some coarse apatite- rich layers. rather magnetic.
81156	332.60	338.70	RD	14		Por	abundant cm-sized red phenocrysts with dark fine-grained matrix. Towards the end are quite many fracture fillings with Mag
81156	338.70	350.95	RD				Altered rhypdacite
81156	350.95	370.95	RD	84		Por	Less converted Brown Red Matrix with red porfyroblaster. Sometimes stray grains rather uncertain
81156	370.95	413.40	RD	7			Grey converted porphyry. Sprinkle the granules are usually off-white but red elements are present - even matrix can sometimes be a slight brownish red. Sometimes it is a distinct foliation of the matrix which then appears to consist of biotite and chlor
81163	29.70	65.00	MUD	37	fg		Qz/Cal veins
81163	65.00	71.15	GRW	37	mg		More Cal/Qz veins than above. Clasts up to 8cm long locally deformed.
81163	71.15	75.15	CONgr	7	mg	Agg	Zone with much more clasts different in size and nature still deformed
81163	75.15	91.95	GRW	7	fg	Agg	Cal/Qz veins. Locally very fine grained>>tends to mudstone
81163	91.95	113.70	CONgr	7	mg	Agg	2-5 cm in size clasts different in nature (porphyry quartz dark dense silicates light gray silicates...). The matrix is composed of greywacke. Less clasts toward the lower contact.
81163	113.70	132.90	lgHEM	7	aph		Hem in a fine-grained light gray matrix.
81163	132.90	134.80	GRW	7	fg		Same as above but with many cracks filled with pinkish Cal
81163	134.80	140.80	GRW	7	fg		Homogeneous with mm-sized black grains (Chl?).
81163	140.80	147.95	GRW	7	fg		Same as above but with many cracks filled with pinkish Cal
81163	147.95	158.80	GRW	17	fg		Irregular Hem bearing rocks with Cal Amp and Chl
81163	158.80	176.45	GRW	17	fg		Hem amount increasing toward the lower contact. Sprinkle Barley light mineral (Fsp?). Several dm-wide pink Cal veins
81163	176.45	183.90	GRW	7	fg		Stratified/ banded Hem. Abundant yellowish Cal in the guangue. some irregular Qz fragments.
81163	183.90	188.85	lgHEM	7	aph		
81163	188.85	190.40	RD	74	mg		Inhomogeneous strongly altered porphyry. Hem and Ap
81163	190.40	192.60	RD	4	mg		Inhomogeneous unit. Chl in cracks ?
81163	192.60	197.50	RD	4	mg		
81163	197.50	203.90	RD				Strongly altered porphyry
81163	203.90	208.65	RD	4		Por	weathered with large brown crystals in the cracks See pictures
81163	208.65	209.50	RD	4		Por	Moderatly altered porphyry
81163	209.50	215.10	RD	4		Por	Least altered porphyry
81163	215.10	285.00	RD	4		Por	

Table 13.8 Drillcore logging results for PG81165 and PG81617.

Drillhole	From	To	Rocktype	Colour	Grainsize	Texture	Comments
81165	2.20	28.10	CONq	7	fmg		Chlorite schist with some Specularite and some Malachite. Some Qz/Cal veins associated with Py. The unit is very altered and leached (creating cavities) toward the upper contact. The unit is yellowish altered toward the lower contact.
81165	28.10	91.30	MUD	3	vfg		Same unit as before with some fine grained disseminated Mag.
81165	91.30	95.20	MUD	3	vfg		Homogeneous altered mudstone
81165	95.20	101.40	MUD	3	vfg		Qz/Cal veins. Some small clasts here and there
81165	101.40	121.50	GRW	7	fmg		Clasts inhomogeneous in size and nature with sometimes red pigmentation. Some Cal veins. Matrix composed of coarse grains.
81165	121.50	138.00	CONgr	71	fmg		Same unit as before with some Hem amygdules in addition of the clasts. Stronger Red pigmentation. There are less clasts toward the lower contact.
81165	138.00	148.00	CONgr	71	vfg		Homogeneous unit with few Cal/Qz veins. Some Specularite
81165	148.00	162.35	GRW	73	fmg		Many Qz/Cal veins
81165	162.35	199.35	GRW	73	fmg		Conglomerate. Inhomogeneous unit with Hem in the matrix Ab (Albite) clasts. Some Specularite/Qz veins. Local Mlc (Malachite). Toward the upper contact the rock is rich in Chl (chlorite) and Tlc (Talc). Ep (Epidote) in the cracks
81165	199.35	218.00	CONgr	27	vfg		Many Cal veins. Not Cal veins toward the lower contact.
81165	218.00	222.75	GRW	73	fg		Conglomerate. Ab clasts rich Qz/sp salmonish veins. The Hem composes mostly the matrix >>Breccia ? Locally deformed
81165	222.75	241.25	CONgr	27	vfg		Inhomogeneous mix between massive Hem and strong red apatite. Some disseminated Mag in the Hem. Some Qz
81165	241.25	257.05	CONgr	47	vfg		Inhomogeneous mix between massive Hem and strong red apatite. Some disseminated Mag in the Hem. Some Qz
81165	257.05	260.50	lgHEM	47	vfg		Very K-altered unit strong red in colour. The primary rock type cannot be guessed (Basalt?). Hem veins toward the lower contact. Some Cal veins.
81165	260.50	278.40	BAS	4	fg		Inhomogeneous unit with decreasing amount of massive Hem toward the lower contact. The unit is richer in strong red K-Fsp toward the lower contact. Ab in the Hem. Some Chl and Specularite associated with Cal veins.
81165	278.40	281.15	HEM	47	vfg		Inhomogeneous unit with decreasing amount of massive Hem toward the lower contact. The unit is richer in strong red K-Fsp toward the lower contact. Ab in the Hem. Some Chl and Specularite associated with Cal veins.
81165	281.15	283.90	lgHEM	47	vfg		Inhomogeneous unit with decreasing amount of massive Hem toward the lower contact. The unit is richer in strong red K-Fsp toward the lower contact. Ab in the Hem. Some Chl and Specularite associated with Cal veins.
81165	283.90	286.65	GRW	47	vfg		Massive Hem with some disseminated Mag and Ab/Cal veins
81165	286.65	292.10	lgHEM	7	vfg		Disseminated Mag (Susceptibility up to 350 in some parts). Ab clasts and some Qz/K-Fsp veins. Ep locally in the cracks Diabase from 303 00 to 303 85
81165	292.10	298.05	HEM	2	aph		Disseminated Mag (Susceptibility up to 350 in some parts). Ab clasts and some Qz/K-Fsp veins. Ep locally in the cracks Diabase from 303 00 to 303 85
81165	298.05	301.00	lgHEM	2	aph		Disseminated Mag (Susceptibility up to 350 in some parts). Ab clasts and some Qz/K-Fsp veins. Ep locally in the cracks Diabase from 303 00 to 303 85
81165	301.00	303.00	GRW	2	aph		
81165	303.00	303.85	DIA				Disseminated Mag (Susceptibility up to 350 in some parts). Ab clasts and some Qz/K-Fsp veins. Ep locally in the cracks Diabase from 303 00 to 303 85
81165	303.85	306.95	lgHEM	2	aph		Disseminated Mag (Susceptibility up to 350 in some parts). Ab clasts and some Qz/K-Fsp veins. Ep locally in the cracks Diabase from 303 00 to 303 85
81165	306.95	310.00	HEM	2	aph		Disseminated Mag (Susceptibility up to 350 in some parts). Ab clasts and some Qz/K-Fsp veins. Ep locally in the cracks Diabase from 303 00 to 303 85
81165	310.00	312.90	lgHEM	2	aph		Disseminated Mag (Susceptibility up to 350 in some parts). Ab clasts and some Qz/K-Fsp veins. Ep locally in the cracks Diabase from 303 00 to 303 85
81165	312.90	321.80	HEM	2	aph		Disseminated Mag (Susceptibility up to 350 in some parts). Ab clasts and some Qz/K-Fsp veins. Ep locally in the cracks Diabase from 303 00 to 303 85
81165	321.80	324.80	lgHEM	2	aph		Disseminated Mag (Susceptibility up to 350 in some parts). Ab clasts and some Qz/K-Fsp veins. Ep locally in the cracks Diabase from 303 00 to 303 85
81165	324.80	327.75	HEM	2	aph		Disseminated Mag (Susceptibility up to 350 in some parts). Ab clasts and some Qz/K-Fsp veins. Ep locally in the cracks Diabase from 303 00 to 303 85
81165	327.75	330.75	MUD	47	fg		Chl and Scp (Scapolite) rich. Relicts of phenocrysts are distinguishable toward the lower contact. Does the Scp come from altered phenocrysts from the porphyry ???
81617	532.50	568	QT	7	cg		Compacted sandstone with little porosity
81617	568	598	QT	7	cg		Compacted sandstone with little porosity

Table 13.9 Drillcore logging results for 81617.

Drillhole	From	To	Rocktype	Colour	Grainsize	Texture	Comments
81617	598.30	630.30	CONq	4	fmg		fine grained sandstone matrix with clasts off different size; clasts have mainly reddish colour
81617	630.30	638.60	CONq	4	fmg		fine grained sandstone matrix with clasts off different size; clasts have mainly reddish colour
81617	638.60	676.90	CONq	4	fmg		fine grained sandstone matrix with small clasts; clasts have mainly reddish and grey colour
81617	722.35	722.35	MUD	7	fg		dark grey to light grey/ greenish colour of very fine grained and compact rock
81617	722.35	734.60	GRW	7	fmg		light grey, "ashy colour" of groundmass
81617	734.60	763.45	CONq	4	fmg		
81617	763.45	800	CONq	4	fmg		
81617	800	863.75	BAS	7	fg		intermediate volcano-sedimentary rock with tuff features (dark grey colour), some lighter grey layers
81617	836.75	884.15	GRW	7	fmg		light grey, "ashy colour" of groundmass
81617	884.15	891.55	CONq	4	fmg	Agg	fine grained sandstone matrix with clasts off different size; clasts have mainly reddish colour
81617	891.55	895.85	CONq	4	fmg	Agg	""
81617	895.85	903.60	GRW	7	fmg	Agg	light grey, "ashy colour" of groundmass
81617	903.60	907.30	lg HEM	4	fg		low-grade hematite in dissimination and layers
81617	907.30	913.30	GRW	7	vfg		""
81617	913.30	916.05	MAG+HEM	4	vfg		massive Mag + Hem
81617	916.05	922.20	GRW	7	fmg	Agg	""
81617	922.20	926	MAG+HEM	4	vfg		massive Mag + Hem
81617	926	932.85	MAG	4	vfg		Mag breccia
81617	932.85	935.10	MAG	4	vfg		disseminated Mag
81617	935.10	943.25	MAG	4	vfg		Mag breccia
81617	943.25	962	RD	4	fg	Por	strongly KF altered
81617	962	966.15	MAG	4	vfg		massive
81617	966.15	957.15	MAG	4	vfg		breccia
81617	967.15	972.25	MAG	4	vfg		massive
81617	972.25	994-90	MAG	4	vfg		breccia
81617	994.90	1002.60	RD	4	fg	Por	RD + Mag breccia
81617	1002.60	1044.25	MAG	4	vfg		breccia
81617	1044.25	1048.30	MAG	4	vfg		breccia
81617	1048.30	1052.45	MAG	4	vfg		massive
Drillhole	From	To	Rocktype	Colour	Grainsize	Texture	Comments
87114	194	291.30	mMag	7	vfg		HW OF THE CORE WAS MISSING
87114	291.30	292.84	SP	7	fg		sodic altered; Mag dissemination
87114	292.84	362.15	SP	7	fg		partly potassic and partly sodic altered
87114	362.15	383.46	SP	7	fg		sodic alteration; Mag dissemination stops
87115	209	216.90	QP	7	fg	Por	Start of logging, typical QP
87115	216	227.15	QP	4	fg	Por	moderate potassic alteration
87115	227.15	237.10	QP	4	fg	Por	potassic alteration
87115	237.10	307.95	QP	4	fg	Por	Mag starts to occur as dissemination and veining
87115	307.95	392.15	mMag	7	vfg		massive Mag with some calcite veinlets. Partly sulfides, chloride and actinolite patches
87115	392.15	397.30	SP	7	fg		potassic alteration
87115	397.30	468.50	SP	4	fg		moderate potassic alteration

Table 13.10 Drillcore logging results of KUJ87123 - 88100.

87123	72.40	90.70	QP	4	fg	mnp0<ß	Start of logging; typical QP strongly potassic altered and fine Mag dissemination
87123	90.70	90.80	QP	4	fg	Por	Clay and sericite occurence
87123	90.80	102.00	QP	4	fg	Por	moderate potassic alteration, Mag starts to occur as dissemination
87123	102.00	111.52	QP	4	fg	Por	sodic alteration
87123	111.52	148.08	QP	4	fg	Por	weak potassic alteration
87123	148.08	253.67	mMag	4	vfg		massive Mag with some calcite veinlets. Partly sulfides, chloride and actinolite patches
87123	253.67	254.95	SP	7	fg		potassic alteration
87123	254.95	324.7	SP	7	fg		sodic alteration
87221	135.76	147.52	QP	4	fg	Por	typical QP with potassic alteration
87221	147.52	151.00	QP	4	fg	Por	Mag starts to occur as dissemination and veining
87221	151	158.62	QP	4	fg	Por	sodic alteration
87221	158.62	212.24	QP	4	fg	Por	potassic alteration
87221	212.24	327.65	mMag	7	vfg		massive Mag with some calcite veinlets. Partly sulfides, chloride and actinolite patches
87221	327.65	381.20	SP	7	fg		overall moderate sodic alteration, party potassic. Mag mainly as dissi
88100	398.50	399.2	QP	4	fg	Por	start of logging: potassic altered QP
88100	399.2	479.78	QP	4	fg	Por	potassic altered QP with Mag dissemination
88100	479.78	517.70	mMag	7	vfg		massive Mag with some calcite veinlets. Partly sulfides, chloride and actinolite patches
88100	517.70	523.30	SP	7	fg	Por	SP with Mag veining
88100	523.30	551.90	SP	7	fg	Por	SP with potassic alteration